ADVANCED TRANSMISSION ELECTRON MICROSCOPY STUDIES OF INDUCED INTERACTIONS OF METALLIC SPECIES WITH PEROVSKITE OXIDE HOSTS

by

MICHAEL B. KATZ

A dissertation submitted in partial fulfillment
of the requirements for the degree of
Doctor of Philosophy
(Materials Science and Engineering)
in the University of Michigan
2013

Doctoral Committee:

Professor Xiaoqing Pan, Co-Chair
Adjunct Professor George W. Graham, Co-Chair
Associate Research Scientist Kai Sun
Associate Professor Anton Van der Ven
Professor Ralph T. Yang

Dedication

This dissertation is dedicated to all who have taken on the pursuit of knowledge and all those yet to come. It is dedicated to those who already possess their hard-earned doctorate, to those who are still toiling in the mines, and to those who couldn't quite get there, for better or for worse.

Acknowledgement

I would like, first and foremost, to thank my advisors, Xiaoqing Pan and George Graham. They have guided and financed my forays, adventures, and failures in science over the past many years. None of the work presented in the following document would have been possible without their guidance. I would also like to thank the rest of my committee. Anton Van der Ven was chiefly responsible for overseeing the theoretical work in this dissertation, as well as being an enthusiastic observer of my work throughout the years. Kai Sun offered much advice and assistance throughout the years regarding science in general and microscopy in particular. I would like to thank Ralph Yang for offering essential assistance at a critical moment. Finally, though not able to serve on my doctoral committee, I would also like to extend my thanks to Galen Fisher, for his enthusiasm and advice.

I am, of course, indebted to those who contributed to the work in this dissertation. Baihai Li (University of Electronic Science and Technology of China), under the advising of Liang Chen (Ningbo Institute of Materials Technology and Engineering) and Anton Van der Ven, contributed heroic efforts to the modeling work outlined in this dissertation. His contributions comprise the theoretical portions of Chapters III and V. Specimens and materials were prepared, in part, by Hong Liu (Sichuan University), Yingwen Duan (Lanzhou University), Hongjie Wang (Xi'an Jiaotong University), Minghao Fang (China University of Geosciences), and Xianfeng Du (Xi'an Jiaotong University) during their posts as visiting scholars in our group

at U-M. Some thin films were also generously supplied by Carolina Adamo and Darrell Schlom at Cornell University. Some specimens were processed at Ford Motor Company by Hung-Wen Jen. Also deserving of thanks at Ford are Robert McCabe and Yisun Chen.

This work was made possible by the Electron Microbeam Analysis Laboratory and its staff: John Mansfield, Kai Sun, Haiping Sun, and Ying Qi.

Much of the work in this dissertation was performed off of the U-M campus. I would like to thank Lawrence Allard (Oak Ridge National Laboratory) for his collaboration and assistance as well as his incomparable enthusiasm for all things related to microscopy and Michigan. I would also like to thank others from the science and administrative staff at ORNL, including Jane Howe, David Cullen, Chad Parish, Edgar Lara-Curzio, Raymond Unocic, and Christine Goudy. As well, Wilbur Bigelow (U-M) and the Protochips company deserve my thanks for dreaming up and manufacturing the *in situ* equipment used in this dissertation, respectively. I would also like to thank the staff at the National Center for Electron Microscopy at the Lawrence Berkeley National Laboratory, in particular Quentin Ramasse, Christian Kisielowski, James Ciston, Chengyu Song, and Bin Jiang. Staff at JEOL were also of valuable assistance, including Masahiro Kawasaki, Eiji Okunishi, and Toshihiro Aoki. Finally, Douglas Blom at the University of South Carolina also provided assistance with microscopy work.

I would like to thank current and former members of the Pan Research Group as well for their various contributions to my successes, material and intangible. Yanbin Chen taught me everything I know about TEM sample preparation and myriad lessons of life, relationships, and lunch. Arnold Allenic always kept a cheerful and genial atmosphere in the lab. Wei Guo

provided support for all the heavy lifting. I would like to thank Obiefune Ezekoye for teaching me about rational action and Christopher Nelson for teaching me about irrational action. Kui Zhang grew many of the thin films examined in this dissertation. Shuyi Zhang provided me with invaluable assistance. I would like to thank the rest of the students and postdocs of the group, including Jake Jokisaari, Yi Zhang, Peng Gao, Sung Joo Kim, Rachel Harrington, Liqing Zhou, and Guangyan Zhao.

I also must thank those on staff who kept the building from collapsing in on itself, both proverbially and literally, and were invaluable in providing me administrative, moral, and nutritional support throughout the years. These include Christopher Christian, Beverly Clampit, Shelley Fellers, Christos Filyo, Judy Hyde, Debbie Johnson, Jeanette Johnson, Georgia Knope, Keith McIntyre, Nancy Polashak, Justin Scanlon, Pattie Vogel, and Kevin Worth. A very special thanks goes to Renee Hilgendorf, who was essential in making sure I graduated so I would stop bothering her.

Many faculty at U-M, both in and outside the Dept. of Materials Science and Engineering, are deserving of acknowledgment. Specific thanks go to Michael Falk and David Martin for offering me the chance to perform undergraduate research under their supervision. The following are also deserving of acknowledgment for their constructive conversations and/or especially inspiring courses: James Allen, Alex Bielajew, Rachel Goldman, Peter Green, John Halloran, Elizabeth Holm, Wayne Jones, John Kieffer, Richard Laine, Neil Marsh, Joanna Millunchick, Kathleen Nolta, John Pasquale, Richard Robertson, Max Shtein, Damon Talley, Katsuo Thornton, George Wynarsky, Steven Yalisove, and Albin Zak.

This entire dissertation was inspired by the work of Hirohisa Tanaka of Daihatsu Motor Co. and colleagues, who, though he may have been scientifically mistaken, gave the strangest and most memorable conference talk I've ever seen.

I would be remiss if I neglected to acknowledge my funding sources. I have been funded in part by the Department of Education Graduate Assistance in Areas of National Need. Work was performed under the funding of National Science Foundation grants DMR-0907191, CBET-0933239, DMR-0723032, DMR-9871177, DMR-0315633, and CBET-1159240. Work at Oak Ridge National Laboratory was sponsored by the United States Department of Energy Office of Energy Efficiency & Renewable Energy, Vehicle Technologies Program.

Finally, I would like to thank my parents for their support throughout my higher education, even though none of us really have any idea what the hell any of this is all about.

Contents

List of Figures

Chapter I

Introduction and Background

1.1 Introduction

The universe formed 13.7 billion years ago.[1] The Earth followed about 9 billions years later,[2] and life on Earth about a billion years after that.[3] The build-up of organic matter resulting from 3.5 billion years of life, and its subsequent transformation into high-energy materials in subterranean deposits has resulted in perhaps the most convenient source of energy currently available. The discovery, extraction, and combustion by human civilization of these fossil fuels helped launch the industrial revolution of the last few hundred years and has led to the development of the world as we know it.

With industrialization, and the rise of the automobile as the primary mode of personal transport in the twentieth century, though, came a dangerous downside. Along with the expected combustion emissions of CO_2 and H_2O, noxious gases were also present in automobile exhaust in hazardous amounts. This mounting problem was, in part, responsible for the passage by Congress and subsequent signing by President Nixon in 1970 of the National Environmental Policy Act of 1969, which gave rise to the Environmental Protection Agency and the Clean Air Act of 1970, which instituted regulations regarding air pollution. With the passage of these laws and the regulations stemming from them, the automobile industry was given a mandate to find a solution to these harmful emissions.

1.2 A Short History of Automotive Catalysis

Three major by-products are produced during the combustion process that must be dealt with. CO is a poison which functions as an oxygen displacant in the bloodstream, while hydrocarbons (HCs) and NO_x form into oxidants that function as general irritants and contribute to smog.[4] The first automotive catalysts, which were put into widespread use in 1974[5] were designed to transform carbon monoxide and unburned hydrocarbons into the more benign by-products CO_2 and H_2O.[6] Both of these emissions can be dealt with in an oxidizing atmosphere, which could easily be accomplished by running the air-fuel mixture at a slightly lean stoichiometry.

The question of the metal to be used for this oxidation catalyst then becomes a matter of elimination. Most common base metal catalysts, for instance Ni, Cu, Co, Mn, Cu, and Cr, and their oxides, are not sufficiently reactive enough[7] or succumb to easily to poisoning by fuel contaminant products.[8] Among precious metals, Pt, Pd, and Rh are the only ones that do not form volatile oxides. Rh, however, is scarce relative to the other two.

Further regulations, beginning in 1979, however, would require the mitigation of NO_x emissions as well.[6] Initially, this was done with two catalyst beds in series, with a rich fuel mixture inducing NO_x reduction reaction in the first bed. Air was then pumped into the second bed to provide an oxidizing atmosphere to process the CO and HCs.[7] After much research and experimentation, Rh proved to be the most suitable NO_x reduction catalyst, despite its cost and scarcity.

Eventually in the 1980s, the limitations involved in a dual-bed catalyst, coupled with advances in oxygen sensing and feedback mechanisms and fuel injection control drove the adoption of the three-way catalyst (TWC). It was so called because it promotes all three reactions with a single

catalyst formulation, with the oxidizing and reducing reactions occurring as the gas feed fluctuates cyclically between lean and rich fuel mixtures.[9] This fluctuation is driven at about 1 Hz by the fuel injection control system, thereby essentially driving all reactions effectively simultaneously.[10] Current formulations include all three metals discussed – Pt, Pd, and Rh – in various combinations.

Precious metals, however, are rare and expensive. In 2011, about $22.5 billion worth of Pt, Pd, and Rh went into automotive catalysts.[11] This is roughly double that from 2010, which was again roughly double the 2009 value. While global economic and market drivers were much of the cause of the four-fold increase over two years, increasingly strict emissions standards coupled with huge projected increases in automobile usage across the world will no doubt continue to increase the demand, and therefore the price, of these catalyst metals.[12]

This scarcity has motivated catalyst engineers to minimize the amount of noble metal used in catalytic converters. Because catalysis occurs on the metal surface, and atoms on the inside not exposed to gas are effectively wasted, the goal is to maximize the surface area to volume ratio and, in most systems, the easiest way to accomplish that is by creating a very high dispersion of very small nanoparticles. Metal nanoparticles, however, will undergo thermodynamically driven coarsening in a process that minimizes energy, and hence, surface area. In order to slow down this sintering, the particles can be placed on a support, which impedes this loss of surface area.

Catalyst supports usually comprise high surface area refractory oxides, which themselves are designed to be resistant against coarsening in the high operating temperatures of the catalytic converter. To this effect, γ-Al_2O_3 was chosen as the obvious solution. It can be synthesized with

very high surface areas, and is generally resistant to loss of surface area at high temperatures. It can, however, undergo a phase transformation to the much lower surface area α-Al_2O_3 when enough heat is applied, losing much surface area in the process. Stabilizing agents, such as La dopants,[13] CeO_2 additions,[14] ZrO_2 additions,[15] or other additives can be used to hinder this process.

CeO_2-based supports then received much attention due to its oxygen storage capacity (OSC).[16,17] The operating principle is that CeO_2 will act as a buffer, damping the sudden swings in the redox environment (air-to-fuel stoichiometry) as well as preventing temporary extremes from adversely affecting catalyst performance or precluding wholly either the oxidation or reduction catalysts from accomplishing their task. It was subsequently found that ZrO_2 could be added to CeO_2 in fractions up to bout 30% to maximally stabilize the surface area and thermal stability of the support, to the point that it is currently the most promising catalyst support.

One aspect that has been absent so far from the discussion in this section is the nature of the interaction between the metal catalyst and the oxide support. For a support to contribute effectively to prevent the coarsening of the catalyst, it must essentially pin the individual nanoparticles on their surface, preventing them from moving around and coalescing with other particles, thus becoming larger and losing surface area. The ideal interaction, in this regard, would be one in which the metal particle sticks to the support surface quite strongly physically, but does not chemically interact to the degree that it loses its natural catalytic activity.

Methods to accomplish this strong interaction can broadly be grouped into two classes: geometric stabilization and what can roughly be called dynamic stabilization. Geometric stabilization is

based principally on classical views of wetting and contact angles and surface energies.[18] The essential goal is to keep particles or metal atoms from those particles from moving around on the support, leading to the processes of either migration and coalescence or Ostwald ripening.[19,20] Migration and coalescence is the easier of the two coarsening mechanisms to understand. If particles are mobile, two particles will eventually meet. This is akin to water droplets moving on a glass pane. At high enough temperatures, these particles will sinter together. When that happens, their overall surface area will reduce, reducing the effectiveness of a given amount of catalyst. For two hypothetical particles of diameter 1 nm, this decrease in surface area after coalescence is 23%. Thus the key to preventing migration and coalescence is to make the energy barrier for particle mobility high.

Ostwald ripening is a process by which atoms from one particle essentially evaporate off of one particle and land on another, causing them each to shrink and grow, respectively, by a small amount for each diffusion event. Smaller particles are less stable than larger particles because of their high surface radius of curvature, and will therefore tend to give off more atoms per area than larger particles. This therefore will result in a greater preponderance of larger particles with lower stability. The theory and kinetics of this process can be found elsewhere.[21]

Dynamic stabilization processes, on the other hand, are phenomena that stabilize particles due to some support-dependent interaction with the catalyst particle. In the case of a strong interaction, the support is not simply considered a non-participating entity that simply lends its surface as a place for a catalyst particle to sit, but actively participates and is, in fact, modified by the presence of the particle itself in some way. One way in which extra stability can be gained is through chemical pinning or anchoring.[22] In one manifestation of the anchoring, Pt placed on a CeO_2

support will, even in a metallic state, form an interfacial Pt-O-Ce bond that will suppress migration and preserve dispersion over the same loading on an Al_2O_3 support.

Another effect, which was met with much fanfare, is the so-called strong metal-support interaction (SMSI).[23,24] When a metal catalyst particle is placed on an SMSI-active support, prototypically TiO_2, and the system is exposed to reducing conditions, the reduced TiO_2 species will migrate up from the support onto the surface of the metal itself. This results in a greater intermingling of the catalyst and the support, and serves to pin the particle in its place on the support surface. The net result, though, after extended times, may end with the particle surface being totally occluded by the mobile support species, thus leaving it unavailable for catalysis.

1.3 The Daihatsu Intelligent Catalyst

A new type of catalyst/support system has been recently developed by the Daihatsu Motor Co. In a series of high-profile articles, beginning in 2001, Daihatsu began promoting what it alternately termed the 'intelligent catalyst' (later, the 'super-intelligent catalyst') and the 'self-regenerative catalyst'. This catalyst system takes advantage of an extensive interaction between a precious metal catalyst and a perovskite oxide support, and claims to utilize the cyclical redox environment in the exhaust stream to alternately dissolve the metal into and extrude it out of the support under oxidizing (lean) and reducing (rich) conditions, respectively. Because the catalyst is essentially re-formed on the surface of the support upon each subsequent redox cycle, any sort of coarsening mechanism is superseded and is not given a chance to occur.

The material explored by Daihatsu took the form of a chemically synthesized metal-doped perovskite powder. In their earliest work, the specific formulation studied was

$LaFe_{0.57}Co_{0.38}Pd_{0.05}O_3$, though formulations with slightly varied transition metal ratios were also tested.[25-28] The data presented in those early works utilized x-ray absorption near-edge structure (XANES), extended x-ray absorption fine-structure (EXAFS), x-ray photoelectron spectroscopy (XPS), and x-ray diffraction (XRD) to show a transition of the Pd atom between a metallic and an ionic oxidation states after repeated redox treatments and an enhanced dispersion after redox treatments relative to simple in-air aging and also versus Pd on Al_2O_3 catalysts. The assertion presented by Daihatsu was that, as prepared and upon oxidation, Pd sits ionically on the perovskite b-site, and upon reduction, it leaves the b-site position, and forms a particle on the perovskite surface, changing from an ionic to a metallic species at some point in the interim.

Transitioning to the simpler perovskite $LaFe_{0.95}Pd_{0.05}O_3$, Daihatsu published additional data showing improved catalytic activity and light-off characteristics.[29,30] They also published rudimentary transmission electron microscopy (TEM) data, claiming to show a drastic reduction of Pd particle size in the 'intelligent' catalyst versus Pd on Al_2O_3, though to the discriminating reader, the micrographs for the 'intelligent' catalyst are somewhat dubious as to their content. More extensive TEM observations[31] showed improvements in Pd dispersion in $LaFe_{0.95}Pd_{0.05}0_3$ over $LaCo_{0.95}Pd_{0.05}O_3$, $LaMn_{0.95}Pd_{0.05}O_3$, and Pd/Al_2O_3, though again, the results are somewhat ambiguous regarding the state of Pd in the $LaFe_{0.95}Pd_{0.05}0_3$ specimen. Curiously, Pd/Al_2O_3 seemed to out-perform the other two perovskites in terms of stabilization against coarsening.

More extensive studies by Daihatsu showed the extent to which the $LaFe_{0.95}Pd_{0.05}0_3$ system was dynamic over temperature and time. A series of experiments where they reduced, then re-oxidized samples at various temperatures showed that the 'self-regenerative' reaction starts at temperatures as low as 200 °C for the reduction reaction and re-oxidation as low as about

400 °C.[31] Furthermore, dynamic EXAFS results seem to show the complete exchange of Pd-O bonds for Pd-Pd bonds upon reduction after mere seconds.[31-34] Their interpretation of this result implies a necessity for some form of heretofore unknown diffusion mechanism that would transport metal from a homogeneously distributed ionic state throughout the host perovskite particle, which is of order 50-100 nm, to a uniformly metallic state on the surface of that particle in a time that is orders of magnitude faster than even grain boundary or surface transport.

Daihatsu then posed the question of whether the phenomenon they were studying was unique to Pd in $LaFeO_3$, and promptly answered themselves by publishing data on Rh and Pt in $CaTiO_3$. They show again x-ray spectroscopy results and interpret the data as proving the mechanism for these additional systems.[32] In fact, they assert[35] that this effect occurs, with various combinations of Pd, Rh, and Pt, in at least seven different perovskites and show a summary of data, purporting to be from spectroscopy results, of the relative capacities of metal in each. Interestingly, they claim that $CaTiO_3$ has zero capacity for Pd, $SrZrO_3$ has zero capacity for Rh, and $SrZrO_3$ and $BaZrO_3$ both have zero capacity for Pt, however no data has yet been published by Daihatsu from these extended experiments.

Because Pt is much heavier than its $CaTiO_3$ host, TEM images of that system are much clearer than those of the $LaFe_{0.95}Pd_{0.05}0_3$ system.[32] They do, in fact, show definite heavy particles of order 2 nm diameter accompanying a much larger oxide particle. However, since TEM necessarily creates a projection image, it is not immediately obvious if those particles are on (the surface of) or in (the bulk of) the perovskite host. Because of the general distribution of particles, it appears to this author that they are most likely on the interior of the perovskite.

As of this writing, in early 2013, no new papers regarding this class of materials have come out of Daihatsu since 2010.[34-50] The reasons for this can only be speculated upon, but they seem to have ceased aggressively pursuing this research. Though other groups have followed up on the material,[36] the 'intelligent catalyst' seems to be increasingly met with waning enthusiasm and, as far as can be gathered, is not yet used effectively in any production catalytic converter. The material, and Daihatsu's interpretation of its behavior, however, pose a set of quite interesting materials questions, which this dissertation seeks to answer.

1.4 Objectives of this Dissertation

The objective of this dissertation is to investigate the 'intelligent catalyst' materials systems proposed by the Daihatsu Motor Company and their claims regarding them. The probe utilized is the TEM, which offers nearly unparalleled abilities to probe the local structure of a material at the atomic resolution and gives a view of the material and the arrangement of the atomic species therein that are direct and leave little leeway for differing interpretation. The model sample will be both powder catalysts, which offer a realistic analogue to the morphology that Daihatsu used and that may be used in real catalytic converters, and planar thin film catalysts, which are ideal form factors for morphological and structural studies in the TEM. This dissertation aims to show whether the systems discussed by Daihatsu function as they claim, to what extent they do so, by what mechanisms they operate, and through which pathways they may be utilized in the future for a practical automotive catalyst.

1.5 References

1 C.L. Bennett, M. Halpern, G. Hinshaw, N. Jarosik, A. Kogut, M. Limon, S.S. Meyer, L. Page, D.N. Spergel, G.S. Tucker, E. Wollack, E.L. Wright, C. Barnes, M.R. Greason,

R.S. Hill, E. Komatsu, M.R. Nolta, N. Odegard, H.V. Peiris, L. Verde, J.L. Weiland, "First-Year Wilkinson Microwave Anisotropy Probe (WMAP) Observations: Preliminary Maps and Basic Results", *Astrophys. J. Suppl. S.* **148** [1] 1-27 (2003).

2 G.B. Dalrymple, "The Age of the Earth in the Twentieth Century: A Problem (Mostly) Solved", *Geol. Soc. London Spec. Publ.* **190** 205-221 (2001).

3 J.W. Schopf, "Microfossils of the Early Archean Apex Chert: New Evidence of the Antiquity of Life", *Science* **260** 640-646 (1993).

4 J. Wei, "Catalysis for Motor Vehicle Emissions", *Adv. Catal.* **24** 57-129 (1975).

5 M. Shelef, R.W. McCabe, "Twenty-Five Years After Introduction of Automotive Catalysts: What Next?", *Catal. Today* **62** 35-50 (2000).

6 H.S. Gandhi, G.W. Graham, R.W. McCabe, "Automotive Exhaust Catalysis", *J. Catal.* **216** 433-442 (2003).

7 J.T. Kummer, "Catalysts for Automobile Emission Control", *Prog. Energy Combust. Sci.* **6** 177-199 (1980).

8 M. Shelef, K. Otto, N.C. Otto, "Poisoning of Automotive Catalysts", *Adv. Catal.* **27** 311-365 (1979).

9 M.V. Twigg, "Progress and Future Challenges in Controlling Automotive Exhaust Gas Emissions", *Appl. Catal. B Environ.* **70** 2-15 (2007).

10 J. Kašpar, P. Fornasiero, N. Hickey, "Automotive Catalytic Converters: Current Status and Some Perspectives", *Catal. Today* **77** 419-449 (2003).

11 J. Butler; *"Platinum 2012"*, Johnson Matthey (2012)

12 C.J. Yang, "An Impending Platinum Crisis and Its Implications for the Future of the Automobile", *Energy Policy* **37** 1805-1808 (2009).

13 B. Béguin, E. Garbowski, M. Primet, "Stabilization of Alumina by Addition of Lanthanum", *Appl. Catal.* **75** 119-132 (1991).

14 A. Piras, A. Trovarelli, G. Dolcetti, "Remarkable Stabilization of Transition Alumina Operated by Ceria Under Reducing and Redox Conditions", *Appl. Catal. B Environ.* **28** [2] L77-L81 (2000).

15 T. Horiuchi, Y. Teshima, T. Osaki, T. Sugiyama, K. Suzuki, T. Mori, "Improvement of Thermal Stability of Alumina by Addition of Zirconia", *Catal. Lett.* **62** 107-111 (1999).

16 A. Trovarelli, "Catalytic Properties of Ceria and CeO_2-Containing Materials", *Catal. Rev. Sci. Eng.* **38** [4] 439-520 (1996).

17 J. Kašpar, P. Fornasiero, M. Graziani, "Use of CeO_2-Based Oxides in the Three-Way Catalysis", *Catal. Today* **50** 285-298 (1999).

18 P. Wynblatt, N.A. Gjostein, "Supported Metal Crystallites", *Prog. Solid State Chem.* **9** 21-58 (1975).

19 P.W. Voorhees, "The Theory of Ostwald Ripening", *J. Stat. Phys.* **38** [1|2] 231-252 (1985).

20 A.K. Datye, Q. Xu, K.C. Kharas, J.M. McCarty, "Particle Size Distributions in Heterogeneous Catalysts: What Do They Tell Us About the Sintering Mechanisms?", *Catal. Today* **111** 59-67 (2006).

21 P. Wynblatt, N.A. Gjostein, "Particle Growth in Model Supported Metal Catalysts—I. Theory", *Acta Met.* **24** 1165-1174 (1976).

22 H. Shinjoh, M. Hatanaka, Y. Nagai, T. Tanabe, N. Takahashi, T. Yoshida, Y. Miyake, "Suppression of Noble Metal Sintering Based on the Support Anchoring Effect and its Application in Automotive Three-Way Catalysis", *Top. Catal.* **52** 1167-1171 (2009).

23 S.J. Tauster, S.C. Fung, R.T.K. Baker, J.A. Horsley, "Strong Interactions in Supported-Metal Catalysts", *Science* **211** [4487] 1121-1125 (1981).

24 S.J. Tauster, "Strong Metal-Support Interactions", *Acc. Chem. Res.* **20** [11] 389-394 (1987).

25 H. Tanaka, I. Tan, M. Uenishi, M. Kimura, K. Dohmae, "Regeneration of Palladium Subsequent to Solid Solution and Segregation in a Perovskite Catalyst: An Intelligent Catalyst", *Top. Catal.* **16|17** [1-4] 63-70 (2001).

26 H. Tanaka, M. Misono, "Advances in Designing Perovskite Catalysts", *Curr. Op. Sol. St. Mater. Sci.* **5** 381-387 (2001).

27 Y. Nishihata, J. Mizuki, T. Akao, H. Tanaka, M. Uenishi, M. Kimura, T. Okamoto, N. Hamada, "Self-Regeneration of a Pd-Perovskite Catalyst for Automotive Emissions Control", *Nature* **418** 164-167 (2002).

28 H. Tanaka, N. Mizuno, M. Misono, "Catalytic Activity and Structural Stability of $La_{0.9}Ce_{0.1}Co_{1-x}Fe_xO_3$ Perovskite Catalysts for Automotive Emissions Control", *Appl. Catal. A* **244** 371-382 (2003).

29 H. Tanaka, M. Taniguchi, N. Kajita, M. Uenishi, I. Tan, N. Sato, K. Narita, M. Kimura, "Design of the Intelligent Catalyst for Japan ULEV Standard", *Top. Catal.* **30|31** 389-396 (2004).

30 Y. Nishihata, J. Mizuki, H. Tanaka, M. Uenishi, M. Kimura, "Self-Regeneration of Palladium-Perovskite Catalysts in Modern Automobiles", *J. Phys. Chem. Sol.* **66** 274-282 (2005).

31 H. Tanaka, "An Intelligent Catalyst: The Self-Regenerative Palladium-Perovskite Catalyst for Automotive Emissions Control", *Catal. Surv. Asia* **9** [2] 63-74 (2005).

32 H. Tanaka, M. Uenishi, M. Taniguchi, I. Tan, K. Narita, M. Kimura, K. Kaneko, Y. Nishihata, J. Mizuki, "The Intelligent Catalyst Having the Self-Regenerative Function of Pd, Rh and Pt for Automotive Emissions Control", *Catal. Today* **117** 321-328 (2006).

33 M. Uenishi, H. Tanaka, M. Taniguchi, I. Tan, Y. Nishihata, J. Mizuki, T. Kobayashi, "Time Evolution of Palladium Structure Change with Redox Fluctuations in a $LaFePdO_3$ Perovskite Automotive Catalyst by High-Speed Analysis with *in situ* DXAFS", *Catal. Comm.* **9** 311-314 (2008).

34 D. Matsumura, Y. Nishihata, J. Mizuki, M. Taniguchi, M. Uenishi, H. Tanaka, "Dynamic Structural Change in Pd-Perovskite Automotive Catalyst Studied by Time-Resolved Dispersive X-ray Absorption Fine Structure", *J. Appl. Phys.* **107** 124319-1-5 (2010).

35 H. Tanaka, M. Taniguchi, M. Uenishi, N. Kajita, I. Tan, Y. Nishihata, J. Mizuki, K. Narita, M. Kimura, K. Kaneko, "Self-Regenerating Rh- and Pt-Based Perovskite Catalysts for Automotive-Emissions Control", *Angew. Chem. Int. Ed.* **45** 5998-6002 (2006).

36 K.B. Zhou, H.D. Chen, Q. Tian, Z.P. Hao, D.X. Shen, X.B. Xu, "Pd-Containing Perovskite-Type Oxides Used for Three-Way Catalysts", *J. Mol. Catal. A* **189** 225-232 (2002).

37 U.G. Singh, J. Li, J.W. Bennett, A.M. Rappe, R. Seshadri, S.L. Scott, "A Pd-Doped Perovskite Catalyst, $BaCe_{1-x}Pd_xO_{3-\delta}$, for CO Oxidation", *J. Catal.* **249** 349-358 (2007).

38 G.L. Chiarello, J.-D. Grunwaldt, D. Ferri, F. Krumeich, C. Oliva, L. Forni, A. Baiker, "Flame-Synthesized $LaCoO_3$-Supported Pd 1. Structure, Thermal Stability and Reducibility", *J. Catal.* **252** 127-136 (2007).

39 G.L. Chiarello, D. Ferri, J.-D. Grunwaldt, L. Forni, A. Baiker, "Flame-Synthesized $LaCoO_3$-Supported Pd 2. Catalytic Behavior in the Reduction of NO by H_2 Under Lean Conditions", *J. Catal.* **252** 137-147 (2007).

40 J. Li, U.G. Singh, J.W. Bennett, K. Page, J.C. Weaver, J.-P. Zhang, T. Proffen, A.M. Rappe, S. Scott, R. Seshadri, "$BaCe_{1-x}Pd_xO_{3-\delta}$ ($0 \leq x \leq 0.1$): Redox Controlled Ingress and Egress of Palladium in a Perovskite", *Chem. Mater.* **19** 1418-1426 (2007).

41 G.C. Mondragón Rodríguez, R. Ochrombel, B. Saruhan, "Meta-Stability and Microstructure of the $LaFe_{0.65}Co_{0.3}Pd_{0.05}O_3$ Perovskite Compound Prepared by a Modified Citrate Route", *J. Eur. Cer. Soc.* **28** 2611-2616 (2008).

42 S. Sartipi, A.A. Khodadadi, Y. Mortazavi, "Pd-Doped $LaCoO_3$ Regenerative Catalyst for Automotive Emissions Control", *Appl. Catal. B* **83** 214-220 (2008).

43 G.C. Mondragón Rodríguez, B. Saruhan, O. Petrova, W. Grünert, "Pd-Integrated Perovskite as Effective Catalyst for Selective Catalytic Reduction of NO_x by Propene", *Top. Catal.* **52** 1723-1727 (2009).

44 A. Eyssler, P. Mandaliev, A. Winkler, P. Hug, O. Safonova, R. Figi, A. Weidenkaff, D. Ferri, "The Effect of the State of Pd on Methane Combustion in Pd-Doped $LaFeO_3$", *J. Phys. Chem. C* **114** 4584-4594 (2010).

45 G.C. Mondragón Rodríguez, B. Saruhan, "Effect of Fe/Co-Ratio on the Phase Composition of Pd-Integrated Perovskites and its H_2 SCR of NO_x Performance", *Appl. Catal. B* **93** 304-313 (2010).

46 X. Wei, P. Hug, R. Figi, M. Trottmann, A. Weidenkaff, D. Ferri, "Catalytic Combustion of Methane on Nano-Structured Perovskite-Type Oxides Fabricated by Ultrasonic Spray Combustion", *Appl. Catal. B* **94** 27-37 (2010).

47 M. Santhosh Kumar, A. Eyssler, P. Hug, N. van Vegten, A. Baiker, A. Weidenkaff, D. Ferri, "Elucidation of Structure-Activity Relationships of Model Three Way Catalysts for the Combustion of Methane", *Appl. Catal. B* **94** 77-84 (2010).

48 G.C. Mondragón Rodríguez, K. Kelm, B. Saruhan, "H_2-Selective Catalytic Reduction of NO_x Activity and Microstructural Analysis of New $BaTi_{0.95}Pd_{0.05}O_3$ Catalyst", *Appl. Catal. A* **387** 173-184 (2010).

49 A. Eyssler, E. Kleymenov, A. Kupferschmid, M. Nachtegaal, M. Santhosh Kumar, P. Hug, A. Weidenkaff, D. Ferri, "Improvement of Catalytic Activity of $LaFe_{0.95}Pd_{0.05}O_3$ for Methane Oxidation Under Transient Conditions", *J. Phys. Chem. C* **115** 1231-1239 (2011).

50 I. Hamada, A. Uozumi, Y. Morikawa, A. Yanase, H. Katayama-Yoshida, "A Density Functional Theory Study of Self-Regenerating Catalysts $LaFe_{1-x}M_xO_{3-y}$ (M = Pd, Rh, Pt)", *J. Amer. Chem. Soc.* **133** 18506-18509 (2011).

Chapter II

Materials Preparation and Characterization Techniques

2.1 Introduction

The science and engineering of solid materials encompass four primary components of study: structure, properties, processing, and performance.[1] These components compose what is known as the 'materials science tetrahedron'[2] – each aspect of materials science sits on a vertex and each is connected, or interrelated, to each of the three. This dissertation, being a relatively fundamental study, is concerned mainly with the structure and processing of the materials discussed herein. To that end, this chapter will discuss the characterization techniques and processing procedures utilized throughout this dissertation. Specialized techniques and procedures will be discussed briefly within their respective relevant chapters.

2.2 Characterization Techniques

2.2.1 Transmission Electron Microscopy

Much of the work presented in this dissertation requires a characterization of the materials in question on an Ångstrom-level (1×10^{-10} m) scale. This is the scale of interatomic bonds and the crystalline lattice, the scale at which the practically indivisible constituent components of matter – atoms and elements[3] – bind together and compose the structures that manifest as solid objects on the human scale. In other words, every aspect of how matter obtains its properties derive from the type and arrangement of the atoms it comprises.

The most practical tool currently available for probing crystalline matter at the atomic scale is the transmission electron microscope (TEM). It comprises generally an electron source that accelerates electrons toward the specimen, electromagnetic lenses that focus the electron beam into a desired configuration, and a detector that collects the electrons after they have interacted in some way with the specimen. Because electrons can be accelerated to several hundred thousand volts, the effective wavelength of the electron beam, given by the de Broglie equation, $\lambda = h\left[2m_e eE\left(1+\frac{eE}{2m_e c^2}\right)\right]^{-1/2}$ for E = 200 keV, is 0.02915 Å.[4] This puts the diffraction limit of the electron beam at far below the necessary resolution to resolve atomic-level features, which are typically on the order of 1 Å. This section comprises a general introduction to the TEM techniques used for this dissertation. For a more detailed description of TEM theory and practice, texts by B. Fultz and J.M. Howe[4] and by D.B. Williams and C.B. Carter[5], respectively, should be consulted.

TEMs can be considered as simple optical systems, with a series of lenses and apertures controlling how the specimen is probed and what information is gathered at the image detector. Conventional TEM is performed in a parallel illumination mode, in which all of the optical rays originating from the source impinging on the specimen are made essentially parallel to the optic axis of the instrument by the condenser lens system, with fine focus on the specimen controlled by the objective lens system. The electron beam is then diffracted by the specimen and reconstituted into a useful image on the detector by the projector lens system focusing either on the image plane, for a simple image, or on the back focal plane, for a diffraction pattern.

Three major sets of apertures are available to manipulate the electron-optical system in a desirable fashion. The condenser aperture, positioned within the condenser lens system, allows

for only the desirable portions of the electron beams emitted from the source to be used for probing the specimen. This is essentially a trade-off between higher signal (larger aperture – more electrons) and higher resolution (smaller aperture – fewer electrons, but a beam with less aberration). There is a caveat, however, that though a smaller aperture limits lens aberrations, it also decreases resolution due to Airy disk blurring, and the two effects must be balanced. The objective aperture is placed in the back focal plane and allows for only beams meeting certain diffractions to be selected to form the resultant image. This is the mode used for bright-field and dark-field imaging. Finally, a selective area aperture, placed in the image plane, allows for the selection of rays emanating from only a specific portion of the specimen to compose a diffraction pattern.

The work presented in this dissertation, however, makes use predominantly of scanning TEM (STEM), rather than conventional TEM imaging. In STEM imaging modes, the condenser lens system creates a convergent beam condition, in which all rays from the source meet at the specimen. The beam, as the name implies, is then scanned, or rastered, across the specimen. A computer system then collects a time-resolved signal from the detector(s) and uses that to reconstitute a raster image, which can then be displayed on the screen and/or stored. The detector can be one of several types, capturing various angles of scattered and/or transmitted electrons to various effect[6], but is most frequently simultaneously operated high-angle annular dark-field (HAADF) and bright-field (BF) detectors. Images acquired using HAADF-STEM imaging take advantage of Rutherford scattering, and usefully show contrast roughly proportional to the square of the atomic number of the probed atom, and are thusly known alternately as Z-contrast images.[7] Additionally, since the inner collection angle of the HAADF detector is so large, all coherently scattered electrons – that is, electrons scattered by Bragg

diffraction – are excluded from contributing to the resultant image. This means that HAADF-STEM is resistant to such artifacts as thickness fringes or anomalous diffraction contrast, and gives a signal that, in most practical cases, is simply based monotonically on the mass and thickness of the specimen. A schematic of a STEM system is shown in Figure 2.1.

Because the TEM relies on electromagnetic lenses, it suffers from lens aberrations, which keep the instrument from achieving its theoretical resolution limit. Spherical aberration (C_S) is the main aberration affecting the performance of electron-optical instruments. C_S is a geometric aberration – that is it is created by inadequacies in the probe-forming lenses in terms of creating spherical lens geometries. Differences in the focal power of the lenses along various radii keep the optical rays from converging on the same point, thus creating a so-called disc of confusion, an limiting the ultimate achievable resolution of the instrument. In recent years, however, technological advances have made possible the practical operation and widespread dissemination of C_S correctors.[8-10] This, in turn, allows for reliable imaging at atomic resolution with clearly resolvable single atoms or crystalline atomic columns.

Several different instruments were used to contribute to this work. At the University of Michigan Electron Microbeam Analysis Laboratory (EMAL), a JEOL JEM-3011 high-resolution TEM and a JEOL JEM-2100F C_S-corrected TEM/STEM were used. Also used were JEOL JEM-2200FS C_S-corrected TEM/STEMs at Oak Ridge National Laboratory and Lehigh University, a JEOL JEM-2100F C_S-corrected TEM/STEM at the University of South Carolina, and at the JEOL demonstration facility in Tokyo, Japan, JEOL JEM-2100F and JEM-ARM200F C_S-corrected TEM/STEMs. With the exception of the JEOL JEM-3011, which is operated at 300 kV, all instruments were operated at an accelerating voltage of 200 kV. The JEOL JEM-2100F housed

at EMAL has achieved a resolution of 1 Å in HAADF-STEM imaging. A beam energy spread of 0.75 eV (full-width at half-maximum) can be achieved, although a spread of roughly 1 eV is regularly achievable under practical circumstances.

2.2.2 Spectroscopy in the Transmission Electron Microscope

In addition to simply imaging, TEM/STEM can be used in conjunction with various spectroscopic techniques in order to characterize the chemical nature of the specimen. These techniques are x-ray energy-dispersive spectroscopy (XEDS) and electron energy-loss spectroscopy (EELS). Each offers a way to obtain information about the elemental identity of the atom impinged upon by the beam, and each has both advantages and disadvantages.

XEDS is perhaps the simpler of the two techniques to understand. The process of generating an x-ray from at atom begins when a high-energy electron impinges on that atom. If that impinging electron is able to impart enough energy on a core electron within the atom, it will eject as a secondary electron. That atom now has a hole in a core level, and so a higher-orbital electron must fall into the now empty inner orbital. In that process, the atom ejects an x-ray, which is characteristic to that particular transition. Though XEDS is somewhat inefficient for lighter elements, and signals from elements lighter than carbon cannot generally be collected, the entire periodic table is none-the-less represented in XEDS spectra. The major disadvantage of XEDS is its extremely low collection efficiency. The specimen emits characteristic x-rays essentially in all directions, but the detector can only collect a small fraction of them, generally covering about 0.05 to 0.1 steradian, with the largest, specialized detectors rated at ~1 steradian. This limitation is the result of the fact that the detector window must be positioned in a compromise between

bringing it close in to the specimen and at a high enough angle so as not to be shadowed by the specimen holder. At higher angles, it must be pulled back to accommodate the upper pole piece.

EELS is the other major spectroscopy technique utilized in this work. EELS signals result from an impinging electron interacting inelastically with an atom in the specimen, losing energy to it before continuing down the TEM column. When generating a characteristic signal, or EELS edge, the beam electron excites a specimen electron either out of the atom entirely or into an unoccupied, higher energy orbital. Since these energy transitions are unique to each element, the resultant energy loss signature in the beam electron is also characteristic. The beam electrons continue down the column and are spread by a magnetic prism according to energy (lower energy electrons will have more curved paths through the prism) before being focused onto a CCD, which acts as the EELS detector. For thin specimens, EELS can provide for a very high signal-to-noise ratio, because almost all of the inelastically scattered electrons that travel down the column can be collected in the entrance aperture of the EELS detector. For thick samples, however, the signal is dominated by the tail of the plasmon excitation peak, which damps out any other appreciable information. Carbon contamination deposition on the specimen from inside the specimen chamber can also cause problems, as the beam induces the carbon to build up on the specimen wherever the beam is impinging, adding effective thickness and additional plasmon signal to the EEL spectrum.

EELS is an incredibly powerful technique for studying local chemistry as well. Because the electron orbital energy levels are altered depending upon the bonding state of the atom, the resultant energy-loss edge is also altered. If the impinging electron beam is sufficiently monochromatic, the fine structure of the edge can be captured, and, for some elements, the

formal oxidation state and/or the bonding environment (*e.g.* oxygen coordination, oxidation state) can be deduced.[11,12] Conversely, not all elements on the periodic table produce productive or convenient EELS edges. Pd, for instance, produces a very broad edge that is often damped out in all but the most ideal conditions. Other elements produce edges that are high in energy, deflecting most electrons away from the entrance aperture into the side of the electron column.

Both EELS and XEDS can be used in conjunction with both TEM and STEM techniques. When combined with the atomic resolution and fine probe control of STEM, however, they become extremely powerful techniques. STEM, as a matter of course, is able to place a sub-Ångstrom probe at any point on the specimen at will, leading to very localized, atomically-resolved EELS and XEDS measurements.[13-16] For this work, both EELS and XEDS were performed on the TEM instruments listed in the previous section using XEDS detectors by JEOL and EDAX and Gatan Image Filter (GIF) EELS systems by Gatan.

2.2.3 X-ray Photoelectron Spectroscopy

The final spectroscopy used in this dissertation is x-ray photo-electron spectroscopy (XPS).[17] XPS, also known historically as electron spectroscopy for chemical analysis (ESCA), is a surface characterization technique in which a specimen is bombarded with ideally monochromatic x-rays in order to induce the ejection of photo-electrons, which are then collected and counted by a detector versus their binding energy, which is calculated by subtracting the kinetic energy of the collected photo-electron from the energy of the impinging x-ray. Each element again has a characteristic set of binding energies unique from other elements. XPS, like EELS, is also sensitive to the local bonding environment of the atoms being probed, though XPS is not usually spatially resolved, as is EELS, and samples from an area usually measured in square millimeters.

The instrument used in this work was a Kratos AXIS Ultra DLD XPS system with a monochromatic Al x-ray source, located at EMAL.

2.3 Sample Preparation and Treatment

2.3.1 Materials Synthesis and Thin Film Growth

Perovskite oxide powders were prepared by either sol-gel chemical synthesis or by the solid state method. For the sol-gel route, stoichiometric amounts of organic precursors for the constituent elements (La, Fe, Ca, Ti, Ba, Ce, Pd, Pt, Rh) were combined in solution with acid, precipitated out and dehydrated into a gel, and calcined, to create a ceramic powder comprising relatively small primary particles. For the solid state synthesis route, stoichiometric amounts of the same metals listed previously, or their oxides or carbonates, were co-milled to intermingle the various powders and calcined at high temperature to homogenize the mixture. Details regarding each synthesis route are presented in their relevant chapter.

When necessary, portions of each powder were then pressed and sintered into dense ablation targets for pulsed laser deposition (PLD), which is a versatile experimental thin film growth technique.[18] PLD comprises basically a laser emitting short pulses focused onto an ablation target within a vacuum chamber. The laser pulses induce a plasma plume to explode off the surface of the target and land on the surface of a heated substrate, where it gradually builds up a thin film. The PLD growth for this work utilized a 248 nm KrF excimer laser. Growth conditions generally comprised a laser energy of 200 mJ, laser repeat rates of 5-20 Hz (usually 10 Hz), substrate temperatures of 600-750 °C, and oxygen back-pressures of about 50 mTorr, with growth times ranging from 30 min to a few hours. Growth rates for the materials in this dissertation were generally approximately 100-300 nm/hr. The particulars are given, again, in

each relevant chapter. Some thin films, graciously provided by Darrell Schlom's group at Cornell University (previously at Pennsylvania State University), were grown by molecular beam epitaxy at his facilities. When required, thin film metal overlayers of Pd or Pt were deposited by vacuum thermal evaporation or r.f. sputtering at the University of Michigan or at Ford Motor Company, respectively.

2.3.2 Sample Processing

When required, both thin film and powder samples were reduced, oxidized, or redox cycled using quartz tube furnaces at either the University of Michigan or Ford Motor Company. Reductions were performed in either 1%, 2%, or 10% H_2 (bal. N_2), and oxidations were performed in either 1% or 20% O_2 (bal. N_2), with aging temperatures of generally 600-800 °C and times of typically 1 hour. All samples were processed in quartz boats.

2.3.3 Transmission Electron Microscopy Sample Preparation

Powder specimens were dropped onto carbon support films on copper TEM grids (Structure Probe, Inc. and Ted Pella, Inc.) for TEM examination. They were, as necessary, ground by mortar and pestle and/or dispersed in solvent (ethanol, methanol, or hexane) and sonicated, though preference dictated that the powder be dropped on the support grid dry to minimize contamination.

Cross-sectional thin film specimens were prepared for TEM by standard preparation procedures. Thin films were glued to sacrificial silicon layers with M-Bond 610 epoxy (Vishay Precision Group) before being sectioned by a low-speed diamond cutting and placed on a wedge-polishing apparatus (Precision TEM, Inc.). Cross sections were thinned and polished by hand using

diamond lapping film (3M) of varying particle sizes before being glued onto a support ring (Structure Probe, Inc.) with M-Bond 610 epoxy. Details of the preparation process are shown in Figure 2.2. The cross sections were then Ar ion milled to electron transparency using a Precision Ion Polishing System (Gatan, model 691).

2.4 References

1 W.D. Callister, *Materials Science and Engineering: An Introduction*, 6th ed., John Wiley & Sons, Inc. (2003).

2 S.M. Allen, E.L. Thomas, *The Structure of Materials*, John Wiley & Sons, Inc. (1999).

3 D.I. Mendeleev, "On the Relationship of the Properties of the Elements to Their Atomic Weights", *Zeitschrift für Chemie* **12** 405-406 (1869).

4 B. Fultz, J.M. Howe, *Transmission Electron Microscopy and Diffractometry of Materials*, 2nd ed., Springer (2002).

5 D.B. Williams, C.B. Carter, *Transmission Electron Microscopy: A Textbook for Materials Science*, Plenum Press (1996).

6 R. Hovden, D.A. Muller, "Efficient Elastic Imaging of Single Atoms on Ultrathin Supports in a Scanning Transmission Electron Microscope", *Ultramicroscopy* **123** 59-65 (2012).

7 S.J. Pennycook, "Seeing the Atoms More Clearly: STEM Imaging from the Crewe Era to Today", *Ultramicroscopy* **123** 28-37 (2012).

8 O.L. Krivanek, N. Dellby, A.R. Lupini, "Towards Sub-Å Electron Beams", *Ultramicroscopy* **78** 1-11 (1999).

9 O.L. Krivanek, G.J. Corbin, N. Dellby, B.F. Elston, R.J. Keyse, M.F. Murfitt, C.S. Own, Z.S. Szilagyi, J.W. Woodruff, "An Electron Microscope for the Aberration-Corrected Era", *Ultramicroscopy* **108** 179-195 (2008).

10 K.W. Urban, "Studying Atomic Structures by Aberration-Corrected Transmission Electron Microscopy", *Science* **321** 506-610 (2008).

11 Z.L. Zhang, W. Sigle, W. Kurtz, M. Rühle, "Electronic and Atomic Structure of a Dissociated Dislocation in $SrTiO_3$", *Phys. Rev. B* **66** 214112-1-7 (2002).

12 H.Y. Tan, J. Verbeeck, A. Abakumov, G. van Tendeloo, "Oxidation State and Chemical Shift Investigation in Transition Metal Oxides by EELS", *Ultramicroscopy* **116** 24-33 (2012).

13 D.A. Muller, L. Fitting Kourkoutis, M. Murfitt, J.H. Song, H.Y. Hwang, J. Silcox, N. Dellby, O.L. Krivanek, "Atomic-Scale Chemical Imaging of Composition and Bonding by Aberration-Corrected Microscopy", *Science* **319** 1073-1076 (2008).

14 M. Varela, A.R. Lupini, K. van Benthem, A.Y. Borisevich, M.F. Chisholm, N. Shibata, E. Abe, S.J. Pennycook, "Materials Characterization in the Aberration-Corrected Scanning Transmission Electron Microscope", *Annu. Rev. Mater. Res.* **35** 539-569 (2005).

15 M. Varela, S.D. Findlay, A.R. Lupini, H.M. Christen, A.Y. Borisevich, N. Dellby, O.L. Krivanek, P.D. Nellist, M.P. Oxley, L.J. Allen, S.J. Pennycook, "Spectroscopic Imaging of Single Atoms Within a Bulk Solid", *Phys. Rev. Lett.* **92** [9] 095502-1-4 (2004).

16 Y.C. Yu, H.L. Xin, R. Hovden, D.L. Wang, E.D. Rus, J.A. Mundy, D.A. Muller, H.D. Abruña, "Three-Dimensional Tracking and Visualization of Hundreds of Pt-Co Fuel Cell Nanocatalysts During Electrochemical Aging", *Nano Lett.* **12** [9] 4417-4423 (2012).

17 L.C. Feldman, J.W. Mayer, *Fundamentals of Surface and Thin Film Analysis*, Prentice Hall (1987).

18 H.M. Smith, A.F. Turner, "Vacuum Deposited Thin Films Using a Ruby Laser", *Appl. Optics* **4** [1] 147-148 (1965).

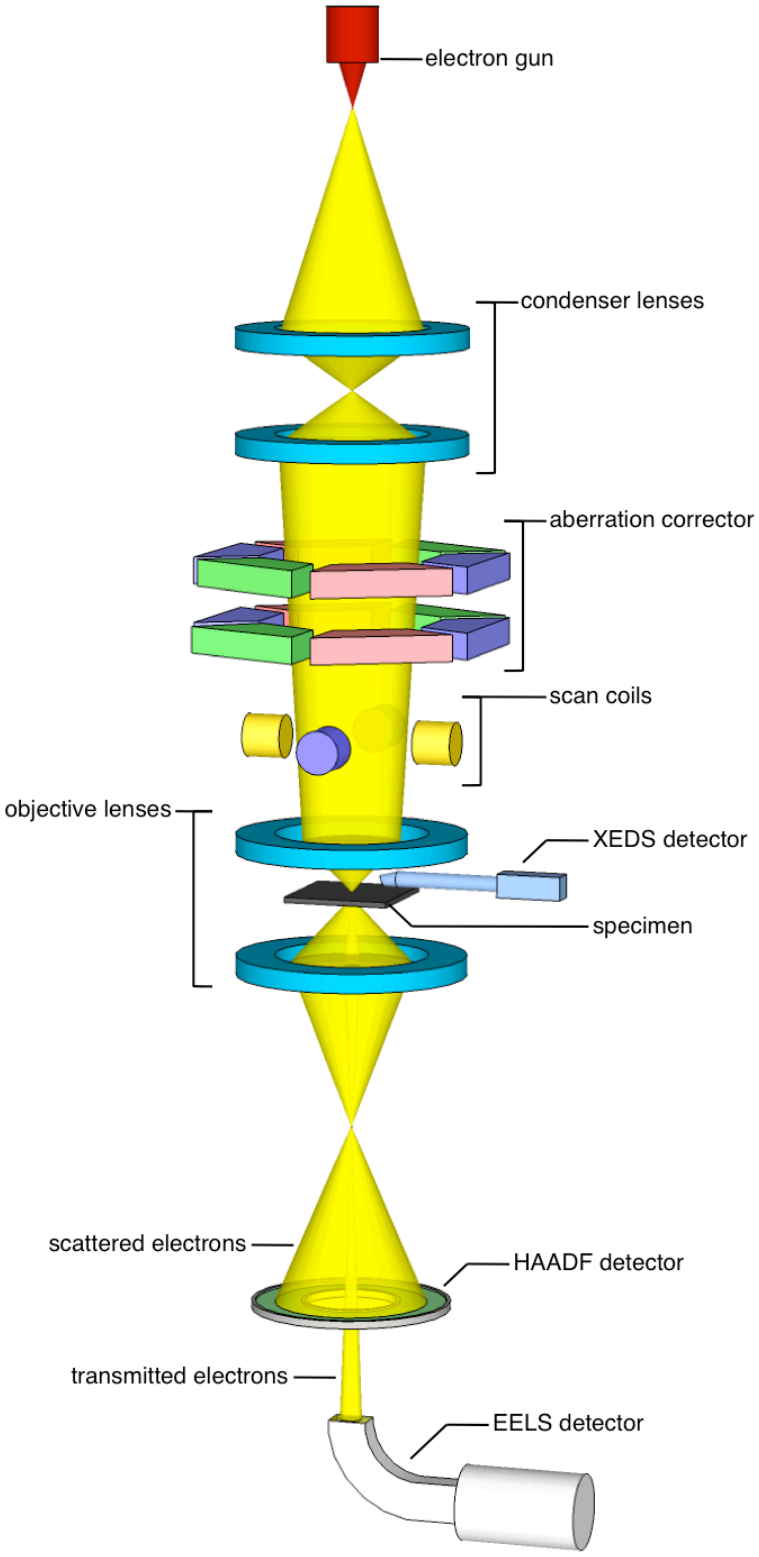

Figure 2.1. Schematic of STEM system showing the relevant components.

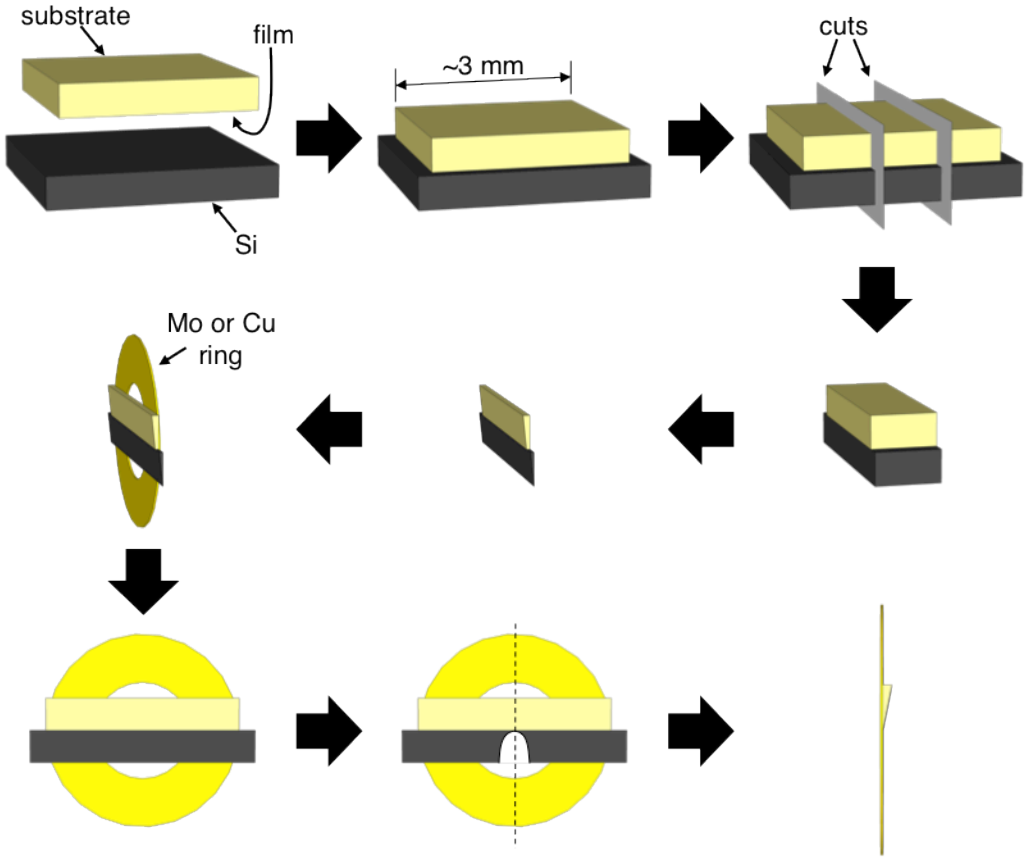

Figure 2.2. A schematic showing the various steps involved in TEM cross-sectional specimen preparation. The film side of the substrate is glued to a sacrificial Si piece, then diced into smaller pieces, approximately 1 mm wide. It is then polished on both sides into a wedge shape and glued to a Mo or Cu ring for ion milling. When the thin edge of the ion-milled hole in the sample reaches the film, the specimen is ready for TEM examination. The final panel shows a cross-section of the dashed line in the lower center panel.

Chapter III

The $Pd/LaFeO_3$ Self-Stabilizing Catalyst

3.1 Introduction and Background

As suggested in Chapter I, automotive exhaust-gas catalysts require a substantial fraction of the world's supply of Pt, Pd, and Rh.[1] The fraction would be lower, however, if the nanometer-size metal particles present in a fresh catalyst could be stabilized against growth during use. A Pd-perovskite catalyst formulation has previously been found to maintain an unusually high level of activity upon aging,[2] and an ingenious process of self-regeneration, involving cyclical dissolution and segregation of Pd into and out of the perovskite lattice during normal use, was proposed by Tanaka *et al.* to account for its stability.[3] Though appealing,[4-6] this explanation, which is based largely on x-ray absorption (near-edge structure and fine structure, XANES and EXAFS respectively) measurements, has not been verified via direct examination of catalyst dispersion. Here are presented results from this atomic-resolution transmission electron microscopy (TEM) study that casts doubt on the viability of the self-regeneration concept.

This study[7], which follows up on the Tanaka *et al.* proposal regarding self-regeneration, focuses primarily on a model planar catalyst geometry that is ideally suited to cross-sectional TEM techniques. Initially considered was Pd-doped $LaFeO_3$, $LaFe_{0.95}Pd_{0.05}O_{3-\delta}$, following the lead of Tanaka *et al.*, who prepared such a composition in high-surface-area powder form to represent the fresh state of their ultimate 'intelligent catalyst'.[8] In this work, thin (of order 100 nm thick)

single-crystal films were grown epitaxially on (100) $SrTiO_3$ substrates using pulsed-laser deposition (PLD), and samples were subjected to various thermal treatments under flowing gas mixtures in a quartz tube furnace. Changes in surface composition induced by thermal treatment were determined by x-ray photoelectron spectroscopy (XPS), and TEM cross-sectional specimens were subsequently prepared.

3.2 Experimental Methods

The citrate method was used to synthesize the PLD targets for the $LaFe_{0.95}Pd_{0.05}O_{3-\delta}$ thin films. Stoichiometric amounts of La_2O_3, $Pd(NO_3)_2 \cdot 3H_2O$, and $Fe(NO_3)_3 \cdot 9H_2O$ were dissolved in de-ionized water with citric acid, and nitric acid was used to control the solution pH. The solution was dehydrated at 100 °C and held at 60 °C until it formed a gel, which was then calcined at 800 °C in flowing oxygen. The surface area (BET) of the resulting powder, some of which was retained for experiments on powder catalysts, was approximately 20 m^2/g. The PLD target for the $LaFeO_3$ thin films was prepared using the traditional solid state reaction method, by combining La_2O_3 and Fe_2O_3 in stoichiometric amounts and grinding them together with a mortar and pestle. The powder was then calcined at high temperature. The resulting powders for both targets were then pressed and sintered at 1200-1300 °C to form dense PLD targets. Film growth was performed in an ultra-high vacuum (UHV) growth chamber using a KrF excimer laser operated at 248 nm. The $SrTiO_3$ (100) substrates were supplied by MTI Corporation. MBE films were grown in a customized UHV system using pure metal La and Fe sources. Some PLD $LaFeO_3$ films were grown atop MBE $CaTiO_3$ thin films utilized as a diffusion barrier against Pd irreversibly diffusing into the $SrTiO_3$ substrate. Pd was deposited on the undoped PLD and molecular beam epitaxy (MBE) thin films by thermal evaporation in UHV.

Thermal processing took place in a quartz tube within a tube furnace. For oxidation, compressed dry air was flowed through the tube at 450 sccm. For reduction, 10% H_2 (balance N_2) was flowed through the tube at 100 sccm after mixing with up to 900 sccm ultra-pure N_2 to vary the H_2 content from 1 to 10%.

Cross-sectional TEM specimens of the various thin films were fabricated using traditional methods, *i.e.*, they were diced to appropriate size, followed by mechanical thinning and polishing on diamond lapping media and final Ar-ion milling (Gatan PIPS, model 691) to electron transparency. It is worth noting that the film surfaces, along with any surface particles, are protected during preparation by a layer of epoxy and a sacrificial silicon wafer. This is effective in preventing any specimen fabrication step from altering the morphology of the surface before it is observed by TEM. Specimens were examined in a JEOL JEM-3011 high resolution TEM operated at 300 keV and spherical aberration (C_S) corrected JEOL JEM-2100F and JEM-2200FS TEMs operated at 200 keV. The TEMs were equipped with XEDS detectors and Gatan image filters for EELS acquisition. X-ray photoelectron spectra (XPS) were acquired using a Kratos AXIS Ultra DLD XPS system with a monochromatic Al x-ray source.

3.3 Results and Discussion

Examination of the high-surface-area powder form of the Pd-doped perovskite catalyst has not convincingly demonstrated the presence of Pd particles in any of the published Daihatsu investigations.[9] In the present study of the $LaFe_{0.95}Pd_{0.05}O_{3-\delta}$ powder sample, Pd particles of a few nanometers in diameter were occasionally found in lightly-reduced (*i.e.*, heated at 700 °C in 5% H_2 in N_2 for 5 h) samples, as shown in Figure 3.1, but these are believed to have probably originated from Pd that was not incorporated into the perovskite during synthesis. (Small

quantities of unincorporated Pd would easily account for the metallic Pd observed by XPS upon reduction at relatively low temperature in Daihatsu's work[9].) The position of these Pd particles was, at best, ambiguous. After further reduction at 800 °C in 10% H_2 in N_2 for 1 h, somewhat larger Pd particles were observed, as shown in Figure 3.2, but based on observations from several agglomerates, it can be concluded that the small number of such particles corresponds to an amount of Pd that is far less (no more than 5%) than expected if all of the Pd had segregated onto the surface of its perovskite host. In fact, the density of particles is similar to that observed on the surface of the film samples (10^2 μm^{-2}), and their larger size may simply reflect normal coarsening of the initially un-incorporated Pd. If it is presumed that the incorporated Pd nearer to the surface of the host particles reaches the surface first, the depth of doped perovskite material needed to produce Pd particles of the sizes observed is less than 1 nm. Of course, these results are not as unambiguous as those from the film samples, due to the thickness of the primary oxide particles, the fact that the positions of the Pd particles relative to the surfaces are, at best, ambiguous, and the low level of contrast between Pd and perovskite. It is worth noting that the powders synthesized for this study comprise single-crystal primary particles which are primarily 100-200 nm in diameter, the same approximate scale as the single-crystal thin films. For this reason, model thin films are an appropriate analogue to the powders for investigating the self-regeneration mechanisms.

Examination of the as-grown film by TEM revealed an atomically flat, well-ordered crystalline surface, and XPS found the expected surface composition. Two distinct chemical states of Pd, both ionic but neither corresponding to the usual +2 state in PdO, were also observed by XPS, whereas Tanaka *et al.* reported only the combination[8], possibly due to a lower instrumental energy resolution. Following a reduction treatment (1% H_2 in N_2 at 600 °C for 1 h), the state at

relatively higher binding energy lost some of its intensity, but, unlike the results of Tanaka *et al.*,[7] no new state corresponding to metallic Pd appeared, and the overall intensity of the Pd photoemission peaks did not increase relative to that of the other perovskite peaks. An additional reduction treatment at both higher H_2 concentration (5%) and temperature (700 °C) was needed to produce the first indication of any metallic Pd, and only by increasing the H_2 concentration to 10% and the temperature to 800 °C was much of the Pd converted to the metallic state, as shown in Figure 3.3a.

At this stage, TEM revealed very few Pd particles (surface areal density no more than about 10^2 μm^{-2}), each having average diameter 3 nm, all of which were epitaxial. An example of such a particle is shown in Figure 3.3b. The observed interfacial structure is consistent with density functional theory (DFT), which predicts that bonding of Pd to LaO layers should be preferred.[10] According to x-ray energy dispersive spectroscopy (XEDS) measurements, there was essentially no change in average Pd concentration within the perovskite, indicating that little of the Pd was expelled onto the surface of the film. In fact, the metallic Pd found on the surface in the form of particles after the final reduction treatment corresponds to the amount initially present within just a nanometer of the surface, consistent with the XPS observations. Similar observations were made on high-surface-area powders, though the results are not as unambiguous.

One possibility is that Pd, rather than extruding to the surface upon reduction, primarily formed into subsurface clusters within the perovskite support. Because of the significantly higher mass of La relative to Pd, small Pd-rich regions, on the order of one nanometer in diameter, would be difficult to identify by TEM. This would especially be true in the case of epitaxial inclusions, which would not disrupt the structure of the surrounding perovskite matrix. Such is the case with

both metallic fcc Pd and La_2PdO_4 (*I4/mmm*).[11] Though no direct evidence for the presence of La_2PdO_4 could be gathered, its presence may explain the unusual double peaks seen in the Pd XPS data.

Since not many Pd particles could be produced on the surface of these films by the reduction treatment, an alternative approach was adopted to examine the metal particle dissolution process. Thus, single-crystal films of pure $LaFeO_3$ were grown on (100) $SrTiO_3$ substrates, again by PLD. The stoichiometry of these films was not exact, however, there being a deficiency in Fe (Fe:La = 0.85), according to wavelength-dispersive x-ray spectroscopy measurements. Approximately 1 monolayer of Pd was then deposited onto the film surface by thermal evaporation in ultra-high vacuum (UHV), and samples were again subjected to various thermal treatments under flowing gas mixtures in a quartz tube furnace. As before, changes in surface composition induced by thermal treatment were subsequently determined by XPS, and TEM cross-sectional specimens were examined after appropriate stages of the treatment.

A low magnification image of the cross section of a sample that was first reduced (1% H_2 in N_2 at 600 °C for 1 h), then oxidized (air at 800 °C for 1 h) is shown in Figure 3.4a. The initial reduction treatment in this case was intended to stimulate growth of moderate-size Pd particles on the surface prior to oxidation. Although the perovskite surface is not atomically flat, it is clear that the Pd (as PdO) particles have sunk partially into the $LaFeO_3$, and a definite reaction zone around the particles can be distinguished by a lower level of contrast relative to the adjacent $LaFeO_3$. This phenomenon is illustrated more clearly for the particle at the extreme left side of the image in the enlargement, shown in Figure 3.4b. The accompanying compositional line scan in Figure 2c, obtained by electron energy loss spectroscopy (EELS), reveals a slight increase in the

Fe/La ratio, relative to the adjacent $LaFeO_3$, in the portion of the zone just outside the PdO particle (*i.e.* 3-6.5 nm along the *x*-axis of the line scan). This variation in composition, confirmed by XEDS in several other examples of the zone, provides a clue, though so far not understood, about the detailed nature of the reaction.

In addition to this indication of a local reaction between the PdO particles and the perovskite film, XEDS mapping revealed the presence of some Pd within the film, as shown in Figures 3.4d-f. As expected from the work of Tanaka *et al.*, regions with Pd (as indicated) are also regions of relatively low Fe concentration, since Pd is known to take the place of Fe in the perovskite lattice. It seems likely that regions of low Fe concentration were present in the film, as grown, due to its off-stoichiometry. Further, crystal defects indicated by structural disorder are also clearly evident in these regions, possibly providing channels for Pd diffusion. Based on a comparison of the XEDS signals from the doped film, discussed above, and this region, the local Pd concentration here is estimated to be about 20% of the Fe concentration.

In order to gauge the importance of crystal defects (including Fe vacancies) in allowing Pd to enter the film well below its surface, stoichiometric $LaFeO_3$ films made by molecular beam epitaxy (MBE), which are of much higher crystalline quality than the PLD films, were also considered. Figure 3.5a shows a cross-sectional image obtained from such a sample, which was simply oxidized (air at 800 °C for 1 h) after Pd was deposited onto its surface. Again, there is clear indication of a local reaction between the PdO particles and the film, as in the case of the PLD film, but the concentration of Pd within the film was much lower (*i.e.*, below the detection limit of XEDS). The crystalline quality of $LaFeO_3$ can thus be eliminated a determining factor in the local reaction that occurs around individual PdO particles contacting the perovskite film, but

certain types of defects may be necessary for much Pd to diffuse from the surface into the bulk of the perovskite film under oxidizing conditions.

To ascertain the effects of extended catalyst operation, involving alternate exposure to both oxidizing and reducing conditions, on Pd dispersion and coarsening, Pd-coated $LaFeO_3$ MBE thin films, initially oxidized as above, were subjected to mild redox cycling (heating to 600 °C in N_2 followed by alternating 10-minute periods of 1% H_2 or 0.5% O_2 in N_2 for 10 hours total, followed by cooling in 0.5% O_2 in N_2). The Pd particles on the surface were generally 5-10 nm in diameter, and all were found to be partially embedded in the support surface, as can be seen in Figure 3.5b. Many of the particles exhibited some degree of epitaxial registration with the perovskite; two typical examples are shown in Figure 3.5c,d. In total, sixty-three particles were examined in on this specimen. Of those particles, the epitaxy of twenty-one could be determined exactly, with five being $[100](001)_{Pt}\left\|[100](001)_{LaFeO_3}\right.$, twelve being $[001](110)_{Pt}\left\|[100](001)_{LaFeO_3}\right.$, and four being $[112](111)_{Pt}\left\|[100](001)_{LaFeO_3}\right.$. Three others were (111)-textured, with those planes parallel to the perovskite surface, though the in-plane registration was of a low index direction and could not be ascertained by imaging. Most of the particles, however, either showed no discernable lattice at all or planes (but not columns) at out-of-plane angles, with a few showing near-vertical (111) planes (implying $[111]_{Pt}\left\|(001)_{LaFeO_3}\right.$. While the support no longer had an atomically flat surface, the $LaFeO_3$ showed no obvious signs of widespread deterioration. The morphology induced by the initial oxidation treatment is thus stable under extended redox cycling. This situation may be contrasted with that in other more typical supports, such as CeO_2, where Pd particles remain entirely on the surface.

The morphology and particle size distribution of this $Pd/LaFeO_3$ catalyst were compared with those of Pd/CeO_2, a common system currently in use. CeO_2 single crystal films were grown by PLD on an yttria-stabilized zirconia (111) substrate, and then Pd was vacuum-deposited onto the fresh surface. Samples of both films were processed simultaneously, as described in the main text (heating to 600 °C in N_2 followed by alternating 10-minute periods of 1% H_2 or 0.5% O_2 in N_2 for 10 hours total, followed by cooling in 0.5% O_2 in N_2). Particle sizes were measured from TEM images obtained from typical regions on cross-sectional specimens of each film, selections of which are shown in Figure 3.6. The Pd particles on CeO_2 were slightly larger than those on $LaFeO_3$, on average. Statistical distributions of Pd on CeO_2 and $LaFeO_3$ are shown in Figure 3.7.

Despite the lack of extensive dissolution and extrusion of Pd into and from the $LaFeO_3$ thin film, there is likely some advantage to the processes occurring in this system. It has been previously hypothesized that an otherwise mobile particle on a support surface will have its collective migration impeded. Wynblatt and Gjostein[13] offer an analysis in which a metal particle is energetically stable in a concavity or surface pore relative to a flat or convex surface, and that the energetic advantage is higher for larger degrees of concave curvature. Their argument is valid for both migration and for Ostwald ripening.

When migrating out of a surface concavity, the particle will have to, out of the necessity of the geometry of the situation, increase its curvature on the 'up-hill' side and decrease its curvature on its 'down-hill' side. This is due to the thermodynamic necessity of the maintenance of its contact angle around its entire perimeter. However, capillary forces will attempt to minimize this curvature and, due to the previously stated contact angle constraint, impel the particle back

toward the center of the concavity. This situation is illustrated in Figure 3.8a, b, and is in contrast to the situation on a flat surface, in which there is no tendency of the particle to move to any particular location.

In terms of Ostwald ripening, the concavity in which a particle sits will, given the same contact angle and volume, decrease the radius of curvature of the particle surface relative to that of a particle on a flat surface, illustrated in Figure 3.8c. Atoms will tend to diffuse/eject off of a surface with a higher radius of curvature and will be more stable situated on one with less curvature, which is, in fact, the very principle behind Ostwald ripening. Therefore, a particle in a depression will tend to be stable, and a particle that creates a concave surface pore in which to sit on a substrate can be termed self-stabilizing.

Though encouraging that the Pd particles studied can potentially self-stabilize themselves by effectively burrowing into the surface of the perovskite support, it would be helpful to form some model as to what process is actually occurring to enable such a reaction. DFT modeling[10] reveals some insights into the process. Discussed earlier was the fact that energetic calculations show that the LaO-terminated surface is stable under reducing conditions and the FeO_2-terminated surface is stable under oxidizing conditions (Figure 3.9), with the conditions used in the experiments discussed operating around that crossover point. Baihai Li examined the behavior of a monolayer of Pd on each of those surfaces after some amount of relaxation time by DFT. As shown in Figure 3.10a, on a LaO-terminated surface, the Pd tends to coalesce into a surface cluster, with seemingly very little interaction with the LaO surface. Indeed, the Pd cluster is suspended entirely above the support surface. Conversely, on the FeO_2 surface, the Pd cluster exhibits quite a strong interaction with the underlying FeO_2 layer, to the point where it is

partially buried in the layer and well-incorporated with the adjacent Fe and O ions, as shown in Figure 3.10b.[10] It is not unreasonable to conjecture that, given conditions that favor FeO_2 surface exposure, the particle will continue to pull itself down into the support, partially displacing the surrounding material and forming a conformal pit for itself. Indeed, from the reaction zone observed in Figure 3.4b and c, it seems to have done just that, explaining the underrepresentation of La in the immediate vicinity of the particle.

3.4 Conclusions

To summarize the observations, it appears that both the formation of Pd particles on the surface of Pd-doped $LaFeO_3$ under reducing conditions as well as the dissolution of Pd particles into $LaFeO_3$ under oxidizing conditions are much more limited processes than would have been expected on the basis of results from Tanaka et al. (i.e., complete exchange of Pd within 1 h at 800 °C), even in the case of the somewhat defective PLD films. Whereas the diffusion of Pd (as ions) very far beneath the perovskite surface likely requires large numbers of defects, possibly both Fe vacancies as well as other extended types, such as point defect clusters, threading dislocations, and orthorhombic twinning boundaries, the strong reaction between Pd (or PdO) particles and $LaFeO_3$ that occurs locally under oxidizing conditions is independent of $LaFeO_3$ crystalline quality. In fact, the length scales observed in these two instances, 100 nm and 1 nm, are consistent with grain boundary and bulk cation diffusion (distance ~ $(Dt)^{0.5}$, where D is the cation diffusion constant and t is the time), respectively, in $LaFeO_3$.[12]

While it was confirmed that processes proposed by Tanaka *et al.* occur to a very limited extent, the predominant mode, according to these observations, is the localized reaction that occurs between Pd particles situated on the surface and the perovskite support under oxidizing

conditions. The surface morphology induced by this predominant mode (*i.e.*, that shown in Fig. 3b), which was also confirmed to persists under the most aggressive reducing condition used (10% H_2 in N_2 at 800 °C for 1 h), has itself previously been connected with increased particle stability: particles sitting in cavities (in this case, generated by the particle themselves) are more resistant to growth due to processes involving both inter-particle transport and particle migration than particles sitting on a flat surface, assuming the same contact angle in both cases.[13]

Finally, a connection can be made between the main results here and those of Tanaka *et al.* By way of justification for such a comparison, the perovskite particles in the powder form of this catalyst are typically characterized by a dimension that is similar to the minimum dimension of these thin films, 100 nm, and they appear to be simply crystalline in nature, *i.e.*, contain few extended defects. Thus, the film and powder forms are structurally quite similar. But how, then, can one account for the XANES and EXAFS results of Tanaka *et al.* (and others)? It is shown in the next chapter that reversible precipitation/re-dissolution of precious-metal-rich clusters occurs throughout the interior of the perovskite film under reducing/oxidizing conditions in other systems that are also considered 'intelligent catalysts'.[14] The perovskite materials in these systems are also crystalline, and the distance over which the precious-metal ions move is only a few nanometers, consistent with expectations based on diffusion data, just as in the Pd-$LaFeO_3$ system. While such clusters in the Pd-$LaFeO_3$ system could not be imaged, they may also form. If so, the reversible formation and disappearance of such clusters could well account for the XANES and EXAFS results in a way that is largely irrelevant for catalysis.

3.5 References

1 J. Butler; Platinum 2010 Interim Review (2010)

2 H. Tanaka, H. Fujikawa, I. Takahashi, "Perovskite-Pd Three-Way Catalysts for Automotive Applications", *SAE Technical Papers* **930251** 63-76 (1993).

3 Y. Nishihata, J. Mizuki, T. Akao, H. Tanaka, M. Uenishi, M. Kimura, T. Okamoto, N. Hamada, "Self-Regeneration of a Pd-Perovskite Catalyst for Automotive Emissions Control", *Nature* **418** 164-167 (2002).

4 J. Li, U.G. Singh, J.W. Bennett, K. Page, J.C. Weaver, J.-P. Zhang, T. Proffen, A.M. Rappe, S. Scott, R. Seshadri, "$BaCe_{1-x}Pd_xO_{3-\delta}$ ($0 \leq x \leq 0.1$): Redox Controlled Ingress and Egress of Palladium in a Perovskite", *Chem. Mater.* **19** 1418-1426 (2007).

5 G.L. Chiarello, D. Ferri, J.-D. Grunwaldt, L. Forni, A. Baiker, "Flame-Synthesized $LaCoO_3$-Supported Pd 2. Catalytic Behavior in the Reduction of NO by H_2 Under Lean Conditions", *J. Catal.* **252** 137-147 (2007).

6 A. Eyssler, P. Mandaliev, A. Winkler, P. Hug, O. Safonova, R. Figi, A. Weidenkaff, D. Ferri, "The Effect of the State of Pd on Methane Combustion in Pd-Doped $LaFeO_3$", *J. Phys. Chem. C* **114** 4584-4594 (2010).

7 M.B. Katz, G.W. Graham, Y.W. Duan, H. Liu, C. Adamo, D.G. Schlom, X.Q. Pan, "Self-Regeneration of Pd-$LaFeO_3$ Catalysts: New Insight from Atomic-Resolution Electron Microscopy", *J. Amer. Chem. Soc.* **133** [45] 18090-18093 (2011).

8 H. Tanaka, I. Tan, M. Uenishi, M. Taniguchi, M. Kimura, Y. Nishihata, J. Mizuki, "$LaFePdO_3$ Perovskite Automotive Catalyst Having a Self-Regenerative Function", *J. Alloys Compd.* **408-412** 1071-1077 (2006).

9 H. Tanaka, M. Uenishi, M. Taniguchi, I. Tan, K. Narita, M. Kimura, K. Kaneko, Y. Nishihata, J. Mizuki, "The Intelligent Catalyst Having the Self-Regenerative Function of Pd, Rh and Pt for Automotive Emissions Control", *Catal. Today* **117** 321-328 (2006).

10 B.H. Li, M.B. Katz, Q.J. Zhang, L. Chen, G.W. Graham, X.Q. Pan, "Surface-Termination-Dependent Pd Bonding and Aggregation of Nanoparticles on $LaFeO_3$ (001)", *J. Chem. Phys.* **138** (2013) in press

11 J.P. Attfield, G. Férey, "Structural Correlations Within the Lanthanum Palladium Oxide Family", *J. Sol. St. Chem.* **80** 286-298 (1989).

12 I. Wærnhus, N. Sakai, H. Yokokawa, T. Grande, M.-A. Einarsrud, K. Wiik, "Cation Diffusion in $La_{1-x}Sr_xFeO_{3-\delta}$, x=0 and 0.1 Measured by SIMS", *Sol. State Ionics* **178** 907-914 (2007).

13 P. Wynblatt, N.A. Gjostein, "Supported Metal Crystallites", *Prog. Solid State Chem.* **9** 21-58 (1975).

14 M.B. Katz, S.Y. Zhang, Y.W. Duan, H.J. Wang, M.H. Fang, K. Zhang, B.H. Li, G.W. Graham, X.Q. Pan, "Reversible Precipitation/Dissolution of Precious-Metal Clusters in Perovskite-Based Catalyst Materials: Bulk Versus Surface Re-Dispersion", *J. Catal.* **293** 145-148 (2012).

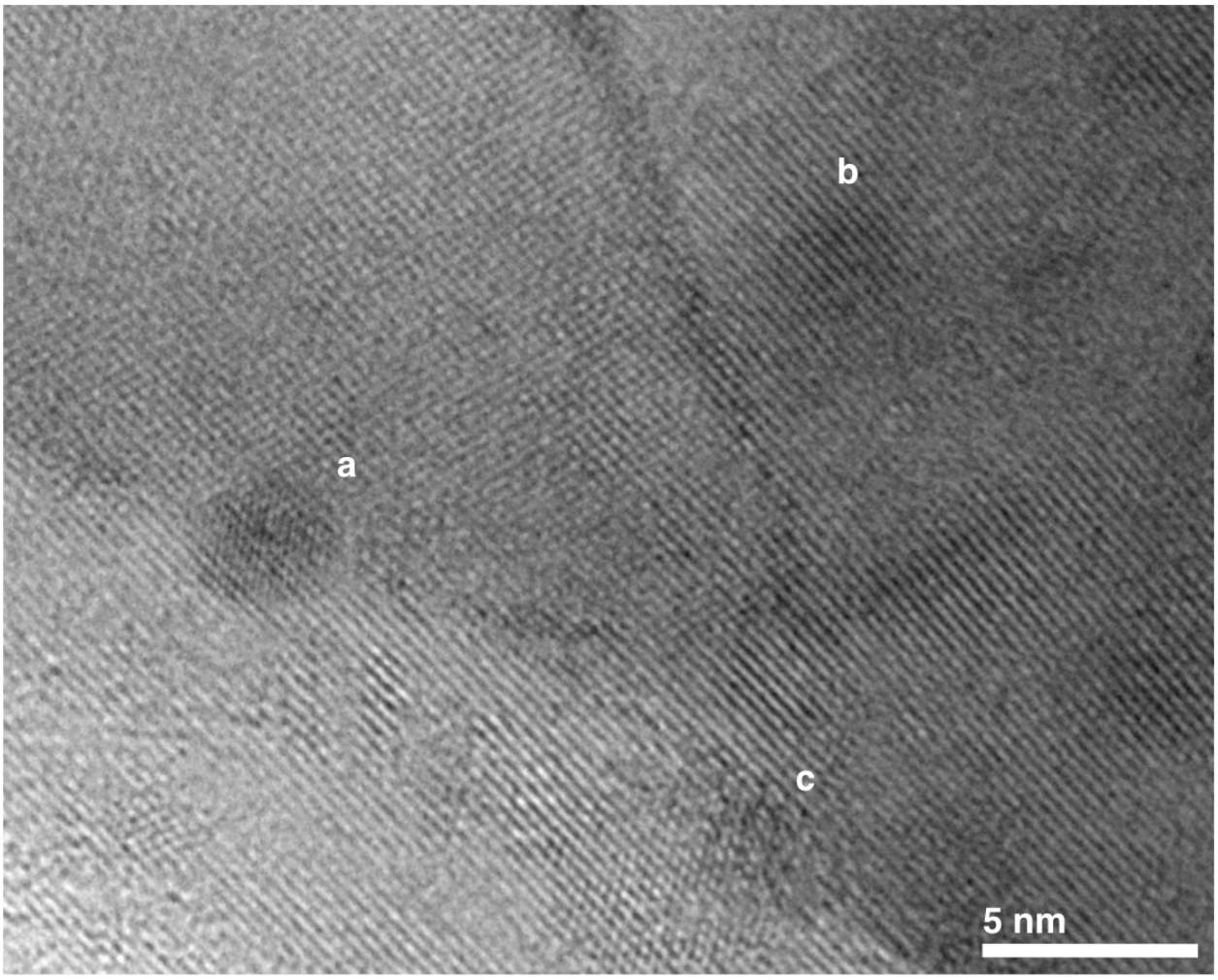

Figure 3.1. High-magnification image of the lightly reduced (700 °C, 5% H_2/N_2, 5 h) powder showing (a) metallic Pd particles as well as (b, c) features that may be Pd particles, but are more ambiguous in nature due to a lack of contrast. All three of these features are ambiguously positioned on the surface of or within the perovskite host.

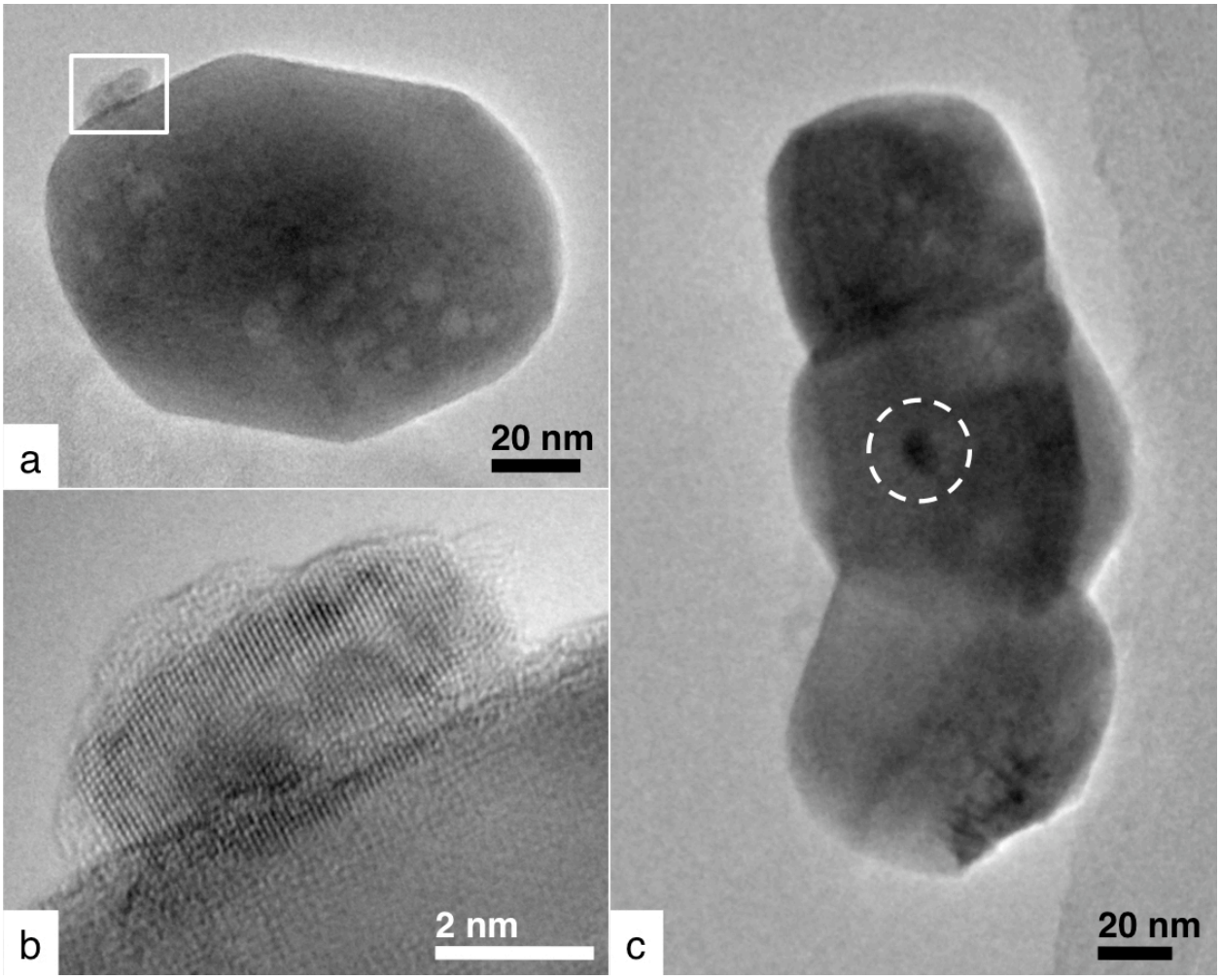

Figure 3.2. High-magnification TEM images of (a) a single perovskite support particle, (b) the Pd particle indicated by the box in (a), and (c) an agglomerate of three perovskite support particles and a Pd particle. The Pd particle in (b) contains the equivalent of 4.6% of the total Pd in its host particle, corresponding to the Pd contained within 7 Å of its surface. Likewise, the Pd particle in (c), indicated by the dashed circle, contains the equivalent of 3.5% of the total Pd in its host agglomerate.

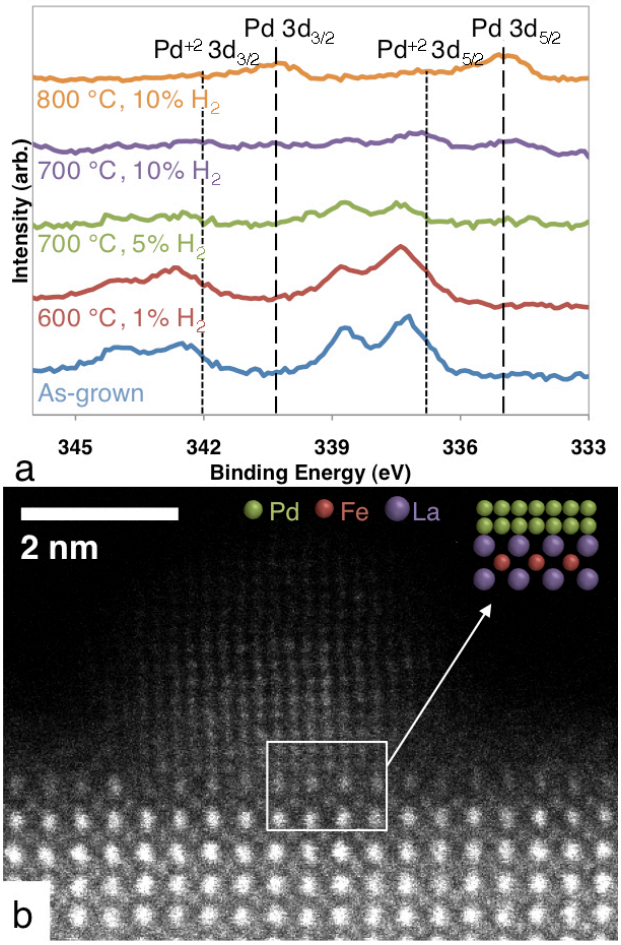

Figure 3.3. (a) XPS spectra of the $LaFe_{0.95}Pd_{0.05}O_{3-\delta}$ PLD thin film after various thermal treatments. (b) High angle annular dark field scanning transmission electron microscopy (HAADF-STEM) image of a typical Pd particle found on the $LaFe_{0.95}Pd_{0.05}O_{3-\delta}$ film surface after the most aggressive reduction step.

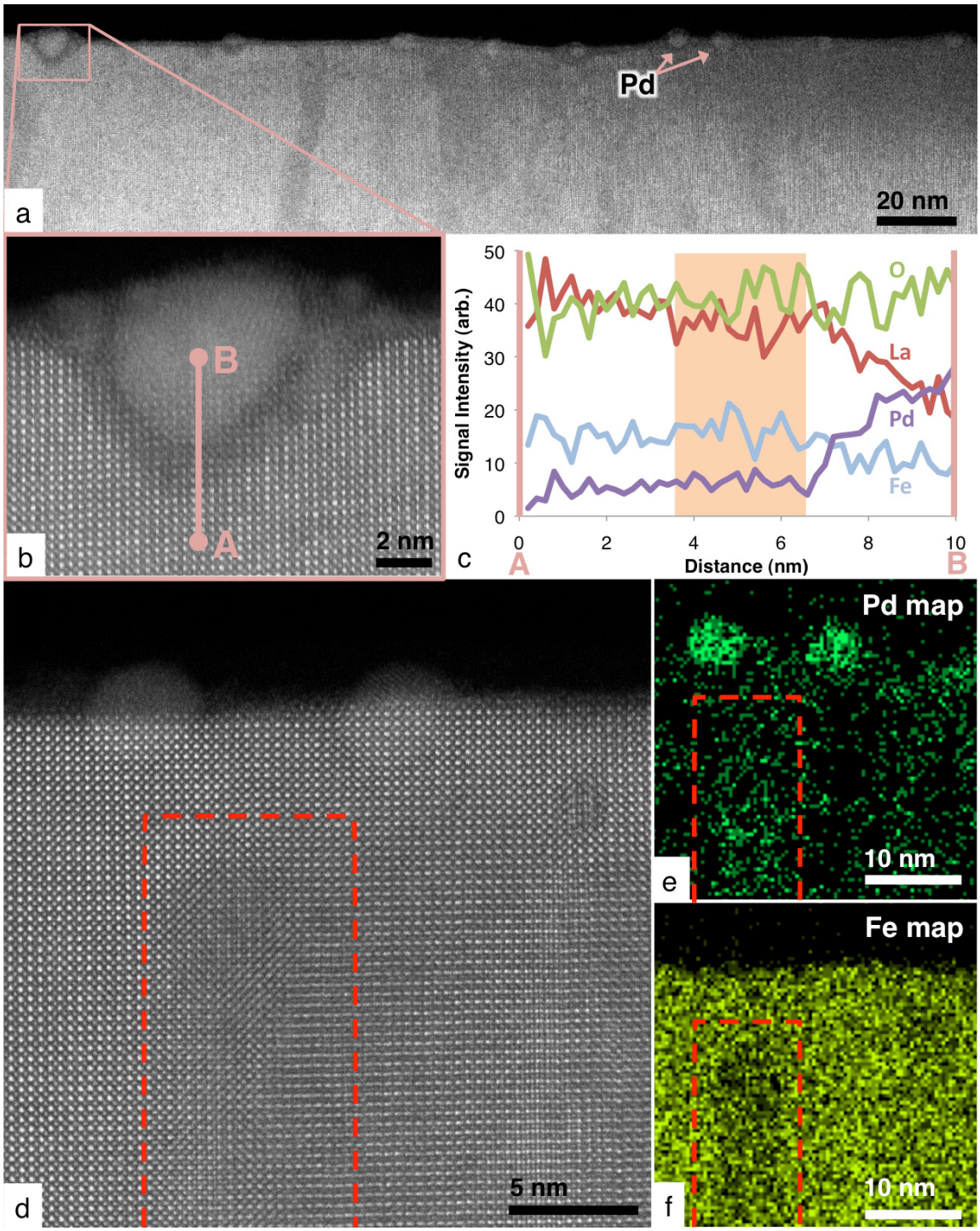

Figure 3.4. (a) HAADF-STEM image of a typical region of the oxidized Pd/$LaFeO_3$ PLD thin film, with (b) an image at higher magnification of one of the partially embedded PdO particles and (c) an EELS line scan taken across the reaction zone at the interface between the oxide and the particle in (b), as indicated by the line A-B. The shaded region in (c) corresponds to the reaction zone in (b). (d) HAADF-STEM image of a region of the oxidized Pd/$LaFeO_3$ PLD thin film with a visibly distorted lattice, together with corresponding (e) Pd and (f) Fe XEDS maps. The indicated areas contain Pd (at levels estimated to be approximately 20% of Fe) within the oxide.

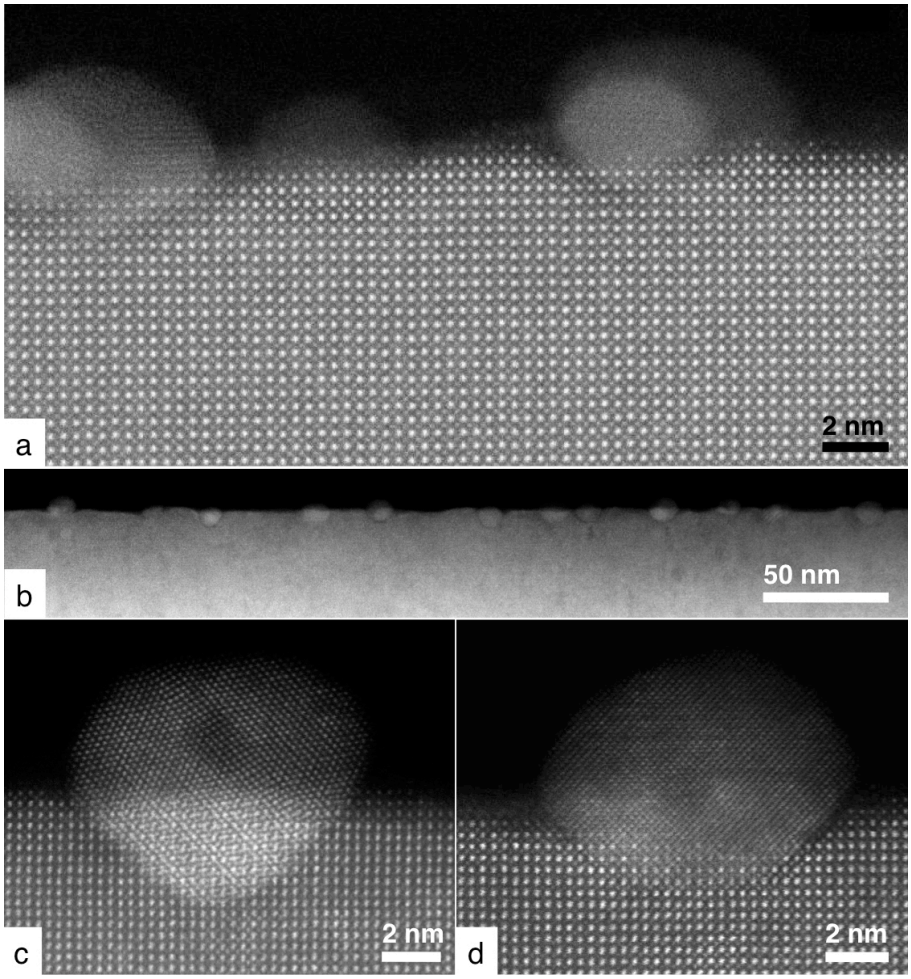

Figure 3.5. (a) HAADF-STEM image of a typical surface region of the oxidized Pd/$LaFeO_3$ MBE thin film. Note that Pd particles have again reacted with the oxide, sinking partially into the surface. (b) HAADF-STEM image of a typical area on a Pd/$LaFeO_3$ MBE film after 10 hours of redox cycling at 600 °C and (c, d) two typical Pd particles shown in detail, with the particle in (d) being epitaxial.

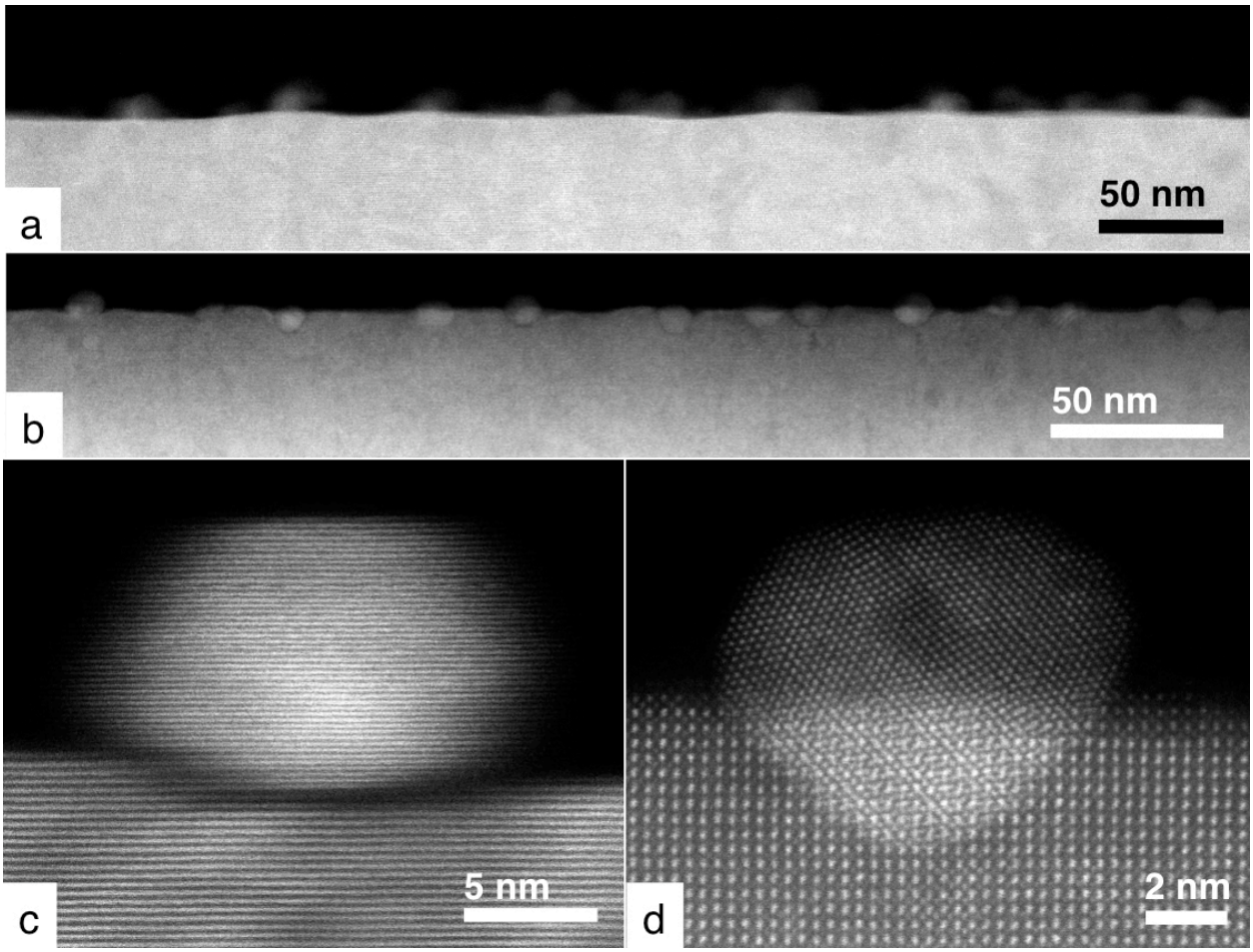

Figure 3.6. HAADF-STEM images of Pd on (a) CeO_2 and (b) $LaFeO_3$ thin films, respectively, after extended redox cycling. High-magnification images of typical Pd particles on (c) CeO_2 and (d) $LaFeO_3$ by TEM and HAADF-STEM, respectively, clearly show the difference in morphologies.

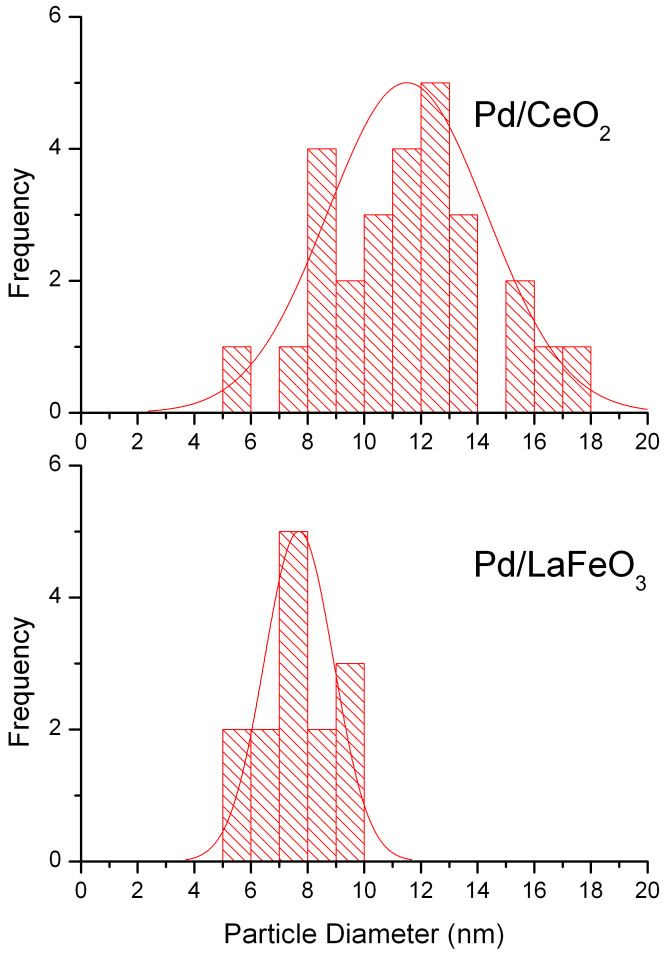

Figure 3.7. Particle size distributions of Pd on CeO_2 and $LaFeO_3$, measured by TEM.

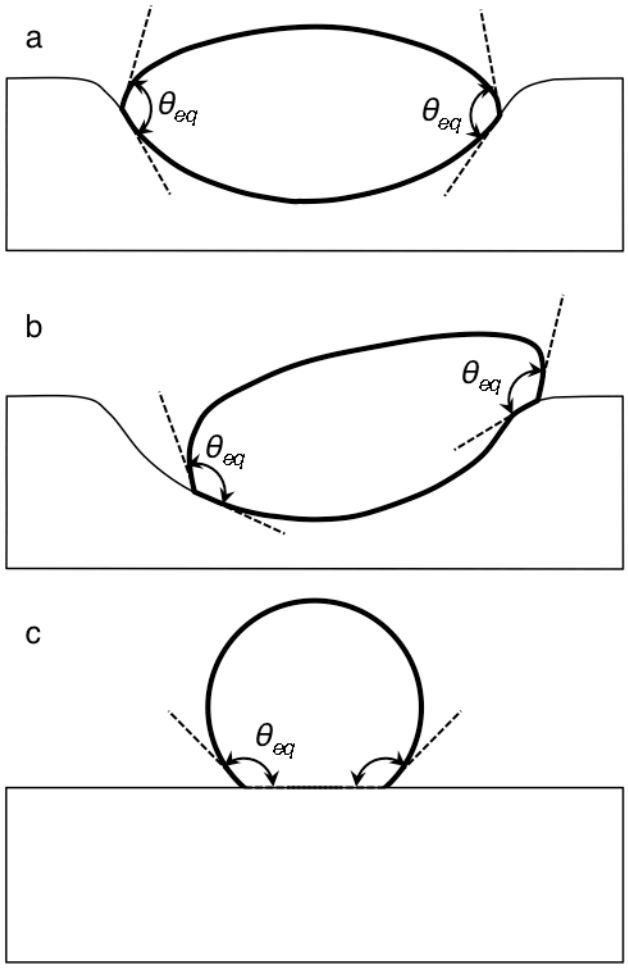

Figure 3.8. Schematics of supported particles with similar volumes (a) situated within a concave surface pore, (b) partially migrated out of the same surface pore, and (c) situated on a planar surface.

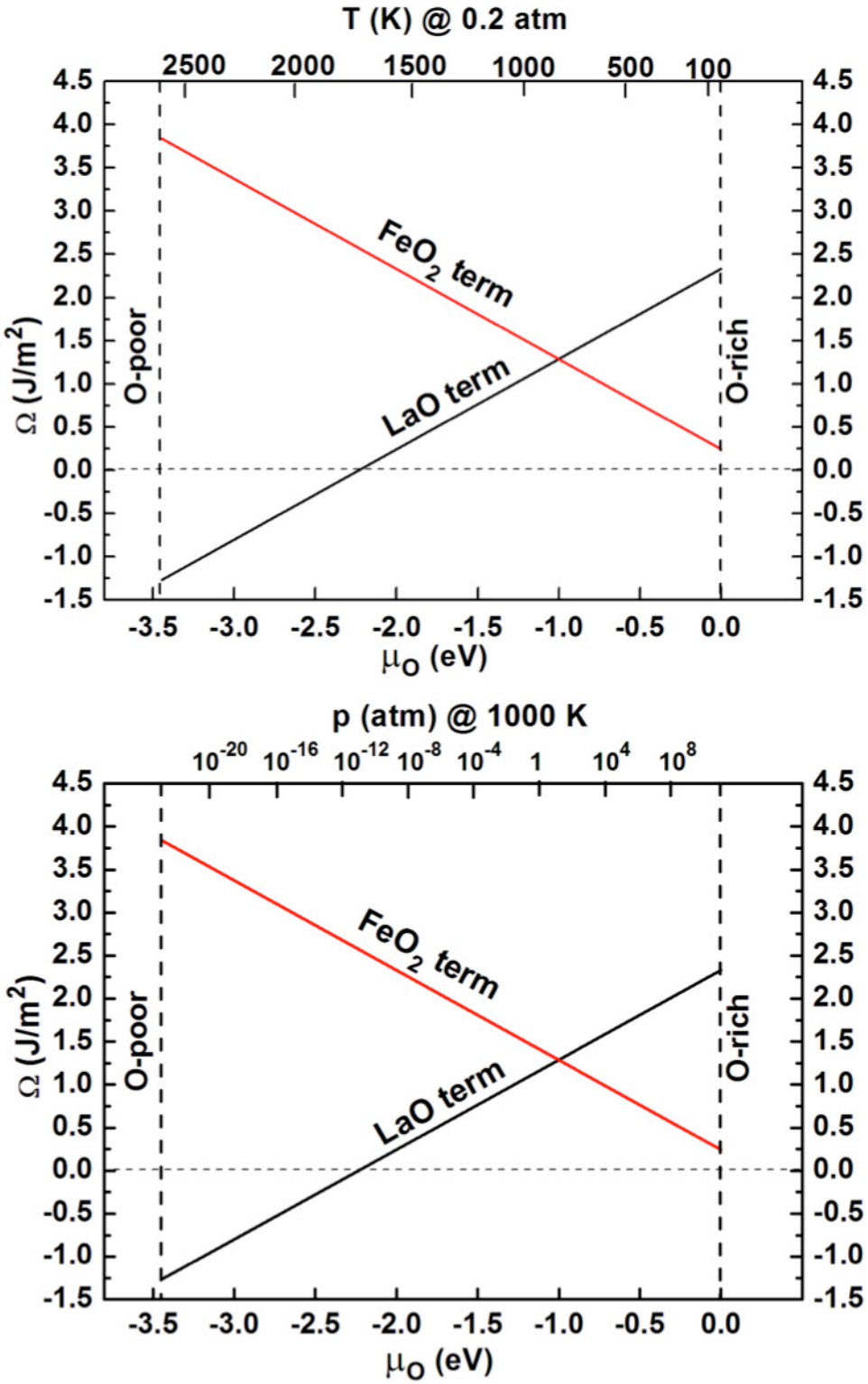

Figure 3.9. Calculated terminating surface stability plots as a function of either varying temperature at constant partial pressure oxygen (top) or varying partial pressure oxygen at constant temperature (bottom), which are essentially equivalent calculations. (Courtesy B.H. Li and adapted from Ref. 10.)

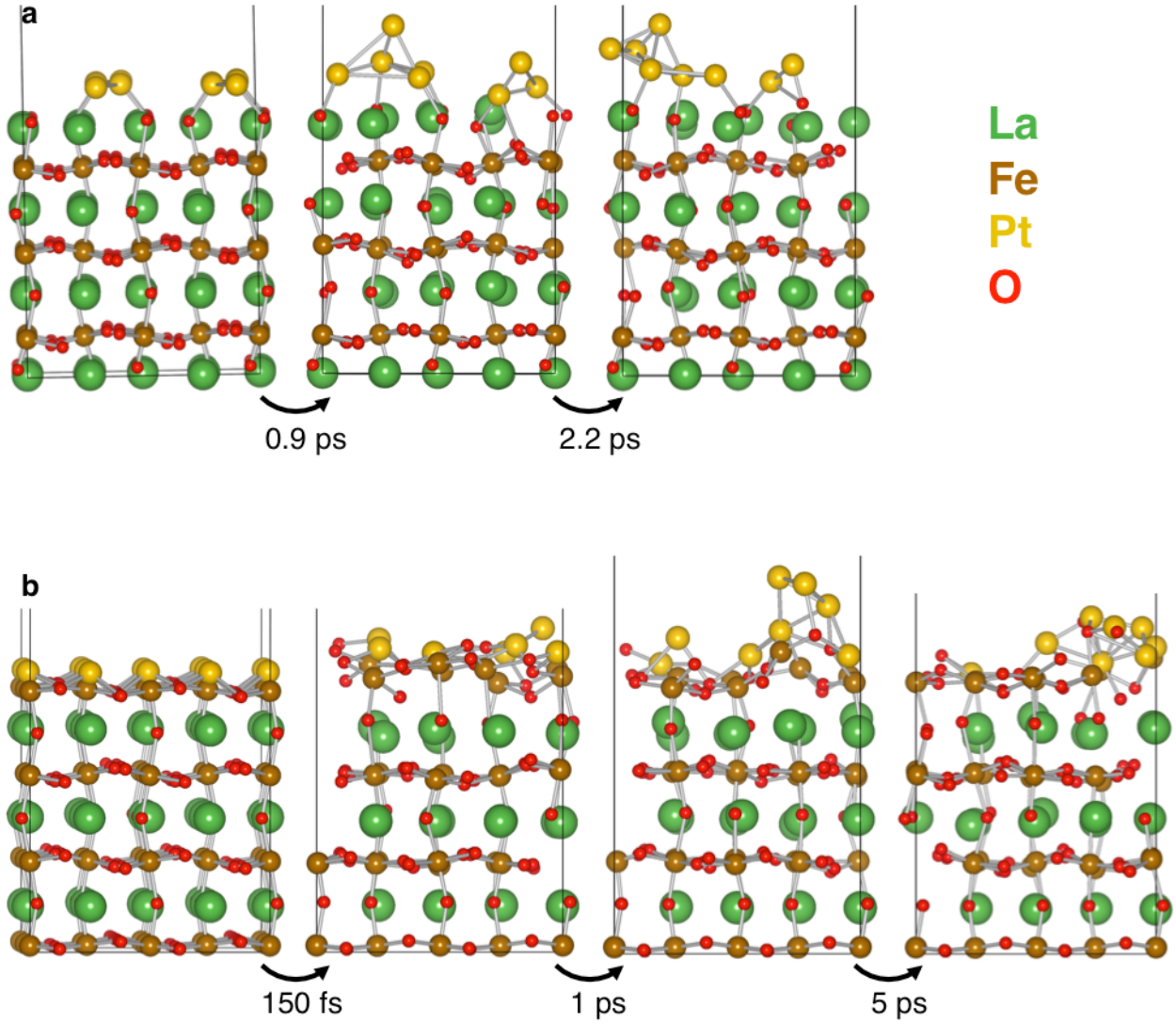

Figure 3.10. DFT relaxations of monolayers of Pd (a) on LaO-terminated and (b) on FeO_2-terminated $LaFeO_3$ (100) surfaces. (Courtesy B.H. Li and adapted from Ref. 10.)

Chapter IV

The $CaTiO_3$-Based Self-Regenerative Catalyst

Part I – A Phenomenological Study

4.1 Introduction and Background

Cyclical re-dispersion of the precious metals in novel perovskite-based three-way catalysts (TWCs) for automotive emissions control has been proposed as a means of dramatically improving catalyst durability, thereby allowing for more efficient precious metal utilization.[1,2] Again, the idea is that nanoparticles of precious metal can dissolve into and re-form out of a particular perovskite under high temperature oxidizing and reducing conditions, respectively. Since such fluctuations in exhaust gas composition are normally imposed at a frequency of about 1 Hz by the TWC engine-control system, the repeated re-formation of nanoparticles in situ would naturally result in self-regeneration of the catalyst,[3] according to the idea's proponents.

Historically, perovskite-based precious-metal catalysts have been of interest since the 1970s,[4] and a number of recent studies that cite the work on self-regeneration above may be found in the literature.[5,6] Typically, the focus is on either perovskite-supported metal catalysis, where strong interactions between metal and support are apparent,[5] or metal-doped perovskite catalysis, where intrinsic activity may be unusual.[6] Little attention, however, has been given to establishing the extent to which cyclical re-dispersion, intended to maintain high dispersion of supported metal particles, actually occurs in these catalysts.

In this chapter, the atomic-scale processes underlying the self-regenerating catalyst concept were thus investigated using spherical aberration (C_S) corrected scanning transmission electron microscopy (STEM) to examine both powder catalysts and cross-sectional specimens of model planar catalysts. In initial studies,[7] summarized in the previous chapter, the Pd-$LaFeO_3$ system was the subject of focus, and the surprising observation was made that both elementary processes, Pd particle formation on the surface of the Pd-doped perovskite, $LaFe_{0.95}Pd_{0.05}O_{3-\delta}$, as well as Pd particle dissolution into $LaFeO_3$, are much more limited than expected, based on the original reports. For example, only a minute fraction of the Pd, *i.e.*, that located within just a few nanometers of a free surface of the doped perovskite, appeared on the surface upon reduction (10% H_2/N_2 at 800 °C for 1h). It is important to realize, however, that the original work sampled the bulk,[1-3] while these observations of Pd nanoparticle formation, as in this example (discussed in Chapter III), were limited to the surface, due to the low contrast of Pd against $LaFe_{0.95}Pd_{0.05}O_{3-\delta}$.

The present study[8] in this chapter considers some of the other proposed systems,[2] exemplified by Pt-$CaTiO_3$, that are more amenable to high-angle annular dark-field (HAADF) imaging in STEM mode because of the higher contrast provided by the relatively heavier precious-metal atoms against their lighter perovskite-support atoms. The main finding is that nanometer-size Pt-rich clusters readily form upon reduction and tend to re-dissolve upon oxidation, but that most of them remain well within the perovskite, where they are essentially inaccessible for gas-phase catalytic reactions.

4.2 Experimental Methods

The citrate method was used to synthesize $CaTi_{0.95}Pt_{0.05}O_{3-\delta}$ powder. Stoichiometric amounts of $Ca(NO_3)_2 \bullet 4H_2O$, $Ti[O(CH_2)_3CH_3]_4$, and $PtC_{10}H_{14}O_4$ (Alfa Aesar) were dissolved in de-ionized water with citric acid, and nitric acid was used to control the solution pH. The solution was dehydrated at 100 °C and held at 60 °C until it formed a gel, which was then calcined at 800 °C in flowing oxygen. A portion of the resulting powder was then pressed and sintered at 1200-1300 °C to form a dense target for pulsed laser deposition (PLD) of thin films. Film growth was performed in 50 mTorr of O_2 within an ultra-high vacuum growth chamber using a KrF excimer laser operated at 248 nm on substrates held at either 600 °C or 750 °C. The $LaAlO_3$ (110) and $SrTiO_3$ (100) substrates used to promote epitaxial film growth were supplied by MTI Corporation.

Subsequent thermal processing of the $CaTi_{0.95}Pt_{0.05}O_{3-\delta}$ powder and films took place in a quartz tube within a tube furnace. For oxidation, dry air was flowed through the tube at 450 sccm. For reduction, 10% H_2 (balance N_2) was flowed through the tube at 100 sccm. These conditions mimic those in the previous work.[1,2]

Cross-sectional STEM specimens of the processed thin films were fabricated by mechanical thinning and polishing on diamond lapping media and Ar-ion milling (Gatan PIPS, model 691) to electron transparency. It is worth noting that the film surfaces, along with any surface particles, are protected during fabrication by a layer of epoxy and a sacrificial silicon wafer. This is effective in preventing any specimen fabrication step from altering the morphology of the surface before observation. Specimens were examined in C_s-corrected JEOL JEM-2100F and JEM-2200FS STEMs operated at 200 kV. Electron energy-loss spectroscopy (EELS) standard

spectra were acquired on a Cs-corrected JEOL JEM-ARM200F STEM with a cold-field emission gun operated at 200 kV. EELS quantification was performed with the Digital Micrograph software package. X-ray photoelectron spectroscopy (XPS) data was acquired using a Kratos AXIS Ultra DLD system with a monochromatic Al X-ray source.

4.3 Results and Discussion

First examined were the powder samples of freshly-prepared Pt-doped perovskite, $CaTi_{0.95}Pt_{0.05}O_{3-\delta}$. (XPS revealed that Pt was present in the Pt^{2+} oxidation state as well as the Pt^{4+} state, based on data in the literature,[9] leading us to allow for the likelihood of oxygen vacancies in this formula.) This powder was examined using C_s-corrected STEM. HAADF images provide atomic mass contrast, which allows us to directly identify small bright features as comprising relatively heavier Pt-rich clusters, confirmable by atomic resolution X-ray energy dispersive spectroscopy (XEDS), contrasting against the lighter $CaTiO_3$ perovskite matrix. As shown in Figure 1a, a few small Pt-rich clusters, several nanometers in diameter, are apparently present in the freshly-prepared material, which consists of roughly 100 nm-sized perovskite particles, which are predominantly single crystals. After reduction in 10% H_2/N_2 at 800 °C for 1 h, many more Pt-rich clusters appear, as shown in Figure 1b.

In an attempt to observe the spatial distribution of Pt-rich clusters formed in the $CaTi_{0.95}Pt_{0.05}O_{3-\delta}$ powder after reduction, a 3-D analysis of select host particles from the same powder sample shown in Figure 4.1 (though not the same particle) was conducted. Both a focal series and a tilt series were obtained for the same particle. Because of the "Z-contrast" nature of high-angle annular dark-field scanning transmission electron microscopy (HAADF-STEM), the

heavy Pt-rich clusters will appear bright against the middle-grey contrast of the host perovskite powder, itself in relief against the black background of vacuum and the lacy carbon support.

In the case of the focal series, the particle was imaged using various focal lengths by adjusting the objective lens power. The convergent nature of the incident electron probe means that only a fraction of the material, in the form of a slice of finite, but small depth (*i.e.* depth of field) is in focus in any given image frame. Though the exact depth of field is unknown, it is, importantly, smaller than the physical depth of the host particle. Chosen for this study was a nearly spherical ellipsoidal perovskite host particle (diameter of ~150 nm) and a proximal smaller companion particle. HAADF-STEM images were acquired every 20 nm over a total depth of 560 nm and sequentially compiled into a focal series. (It should be noted that the two main sources of possible error, sample drift and miscalibration of focal depth as given by the microscope software will be both systematic and internally consistent, and will therefore, if present, lead only to quantitative rather than qualitative error.) If Pt-rich clusters were indeed segregated to the surface, it would follow that only clusters on the periphery of the support particle would be in focus at any given focal depth within the particle. The contrary, however, is true. There is a plurality of Pt-rich clusters in focus throughout the focal series in the center of the projected image of the host particle. Individual images from the back, middle, and front of the particle are shown in Figure 4.2.

A tilt series of the same particle was also acquired. In this case, images of the same particle were acquired at every 2° of tilt over a total range of 40°. Efforts were made to maintain a consistent focal depth within the particle over the tilt series. The individual images were manually aligned

and compiled into a tilt series. When the tilt series is viewed sequentially in full motion, it is obvious that many Pt-rich clusters do not exhibit the same parallax shift as adjacent clusters in the projected image. This can only mean that their radial distance from the center of rotation is less than those adjacent clusters and, hence, are within the perovskite host particle rather than on the surface. Individual HAADF-STEM images from -20°, 0°, and 20° tilts are shown in Figure 4.3. Based on this analysis, it is reasonable to assign most (~90%) of the Pt particles as being on the interior of the perovskite host.

In order to learn more about the location of the Pt-rich clusters and their detailed structure, next examined were the thin films, grown specifically for cross-sectional STEM. The films were grown to thicknesses of order 100 nm, dimensionally similar to the perovskite powder samples produced in both this and the original work,[2] and the Pt was confirmed by STEM to be atomically distributed, as shown in Figure 4.4. The as-deposited thin films were highly crystalline and epitaxial to the (110) $LaAlO_3$ substrate. Films grown at 600 °C exhibit a lamellar structure, with lamellae running along the [100] direction, as shown in Figures 4.5a,b. While these lamellae are separated from each other by a network of micropores, they are aligned approximately along the same crystal directions, differing in in-plane orientation by only a slight rotation. It is important to emphasize that no pores were observed when cross-sectional specimens were viewed along the orthogonal in-plane direction. Films grown at 750 °C, in contrast, were smooth and dense as well as single-crystalline. Under close examination, all films appear to be homogeneous down to the atomic level, with no obvious segregation of Pt from the perovskite in the form of particles either on the surface or within. From this observation, coupled with the mechanics of PLD synthesis and corroboration from XPS confirming the ionic state of

the Pt (Figure 4.6), it seems reasonable to assume that Pt sits on the expected b-site of the perovskite lattice.

A reduction treatment (800 °C, 10% H_2/N_2, 1 h) induces an amalgam of transformations within the thin films, as discussed briefly below. Chief among these is the formation of Pt-rich clusters (confirmed by XEDS, as shown in Figure 4.7) within the perovskite matrix, appearing as bright contrast in Figures 4.5c,e. As shown in Figure 4.8a, these clusters are generally 1-3 nm in diameter, with many being clearly metallic, *i.e.*, exhibiting the expected face-centered cubic (FCC) structure of Pt (Figure 4.9), but the smallest exhibiting ambiguous structure. The structurally ambiguous Pt-rich clusters may be either crystalline clusters that are not epitaxial with the perovskite, or they may be amorphous. Slightly larger clusters (3-5 nm) appear at extended defects, such as threading dislocations or $CaTiO_3$ rotation domain boundaries, with the largest on the free surfaces of the thin films, including the lateral lamellar surfaces, presumably due to faster diffusion of atomic Pt along these paths. It should be mentioned that similar observations were made on the films grown at 750 °C, with the exception that fewer Pt-rich clusters were found on free surfaces, presumably due to their lower area.

In addition, nanometer-size regions of the thin film, clearly associated with relatively large Pt-rich clusters inside the perovskite matrix, have transformed into crystal structures comprising primarily or exclusively Ti cations, most often identifiable as anatase and bronze TiO_2 due to both their crystal structure in the STEM micrographs (Figure 4.10) and their chemical composition by EELS, showing a high Ti signal to the exclusion of Ca. These regions, which collectively make up no more than a few percent of the volume of the film, generally form epitaxially with the surrounding perovskite matrix, with their primary crystal axes aligning with

those of the pseudocubic setting of the perovskite. Occasionally, the Ti-rich regions were disordered and contained some Ti^{3+} (Figure 4.11). Formation of these second-phase regions indicates that the $CaTiO_3$ matrix is at least somewhat mobile at 800 °C, suggestive of cooperative mass transport during precipitation of the largest Pt-rich clusters within a formerly dense oxide matrix.

Reduced films were then subjected to a subsequent oxidation treatment (800 °C, 20% O_2/N_2, 1 h) to determine the extent to which precipitated Pt will dissolve back into the perovskite host, i.e. the reversibility of the reaction. As shown in Figures 4.5d,f, the reduced, then oxidized films are similar to the reduced films, with numerous small Pt-rich clusters within the films and larger metallic (FCC) Pt clusters on the free surfaces. Significantly, the surface clusters are considerably larger than their counterparts in the reduced films, which can be attributed to well-known Pt coarsening mechanisms that occur primarily under oxidizing conditions.[10]

More significantly, most of the very small (~1 nm) Pt-rich clusters observed in the reduced films are absent in Figures 4.5d,f. Since it is unlikely that these interior clusters contributed to the coarsening of surface clusters to any appreciable extent, due to the apparent very slow diffusion of Pt through the perovskite host,[11] they most likely dissolved back into the perovskite. Re-oxidation of the film also served to heal the disordered regions of the film, presumably by driving O back into the material and causing the locally reduced regions to reform into perovskite. In general, the appearance and disappearance of all these phases is consistent with known phase stability and equilibria in the Pt-Ca-Ti-O phase diagram.

In order to gauge the extent to which the same phenomena occur with other precious metals, Rh-doped $CaTiO_3$ was also investigated, starting with analogous powders (Figure 4.12), obtained from Cabot Corporation, then synthesizing thin films (at a substrate temperature of 750 °C) by PLD and exposing them to the same thermal treatments as the Pt-based thin films before sectioning them and subjecting them to STEM examination. The as-deposited films were similar to the films of Pt-based material grown at the higher temperature, *i.e.*, dense and locally smooth, with no obvious segregation of Rh from the perovskite (Figure 4.13a).

After being subjected to a reduction treatment (800 °C, 10% H_2/N_2, 1 h), Rh-rich clusters were found within the film, taking the form of relatively large (3-5 nm) metallic (FCC) Rh clusters generally located at extended defects, epitaxial FCC Rh clusters throughout the material (1-5 nm), and small (1-2 nm) Rh-rich clusters of bright contrast with no discernible lattice distinguishing them from the surrounding perovskite (Figures 4.13b,c). Typical examples are shown in Figure 4.8b. The distribution of Rh-rich clusters is thus very close to the distribution of Pt-rich clusters observed in the Pt-$CaTiO_3$ system. Absent, however, are the small regions of TiO_2 or any disordered regions seen in that system, the formation of which are thought to be promoted by the presence of the large Pt-rich clusters. Apparently, the less noble Rh is not as good a catalyst as Pt for these solid state reactions under these particular conditions.

In further contrast to the behavior of the Pt-$CaTiO_3$ system, re-oxidation (800 °C, 20% O_2/N_2, 1 h) appears to induce the dissolution of the majority of the Rh-rich clusters back into the perovskite (Figure 4.13d). Only the largest Rh clusters, associated with extended defects, remain. This difference may be due to the greater tendency of Rh to adopt an oxidized state compared to Pt.

Aside from these differences in detail, however, it is clear that the overwhelming majority of precious-metal-rich clusters formed upon reduction remain within the bulk of the perovskite host in both cases. Their formation upon reduction, and subsequent dissolution upon oxidation, undoubtedly accounts for the original XANES and EXAFS measurements, but the clusters within the bulk of the perovskite host are essentially irrelevant for gas-phase catalysis. Similar results were also obtained similar results for Pt-$BaCeO_3$, another system previously proposed as a self-regenerating TWC,[12] except that Pt dissolution was found to be more facile in $BaCeO_3$ than in $CaTiO_3$. Though not explored in this work, it is likely that all the other metal-perovskite systems originally characterized by X-ray absorption techniques,[2] including Pd-$LaFeO_3$,[7] may behave in like manner.

4.4 Conclusions

It has been demonstrated, using high-angle annular dark-field scanning transmission electron microscopy (HAADF-STEM), that the cyclical process previously identified by X-ray absorption techniques in a number of precious-metal-doped perovskites that have been proposed as novel self-regenerating three-way catalysts (TWCs), mostly arises from bulk rather than surface re-dispersion. From these findings, it is also clear that only a few nanometers (measured from a free surface) of such perovskites are potentially useful as a host or support for precious metals in any practical embodiment of the original self-regenerating TWC concept. In this case, conditions more accurately mimicking those in practice should also be considered, with the aim of establishing detailed temporal and oxygen chemical potential dependencies of the overall process.

4.5 References

1 Y. Nishihata, J. Mizuki, T. Akao, H. Tanaka, M. Uenishi, M. Kimura, T. Okamoto, N. Hamada, "Self-Regeneration of a Pd-Perovskite Catalyst for Automotive Emissions Control", *Nature* **418** 164-167 (2002).

2 H. Tanaka, M. Taniguchi, M. Uenishi, N. Kajita, I. Tan, Y. Nishihata, J. Mizuki, K. Narita, M. Kimura, K. Kaneko, "Self-Regenerating Rh- and Pt-Based Perovskite Catalysts for Automotive-Emissions Control", *Angew. Chem. Int. Ed.* **45** 5998-6002 (2006).

3 D. Matsumura, Y. Nishihata, J. Mizuki, M. Taniguchi, M. Uenishi, H. Tanaka, "Dynamic Structural Change in Pd-Perovskite Automotive Catalyst Studied by Time-Resolved Dispersive X-ray Absorption Fine Structure", *J. Appl. Phys.* **107** 124319-1-5 (2010).

4 R.J.H. Voorhoeve, D.W. Johnson, J.P. Remeika, P.K. Gallagher, "Perovskite Oxides: Materials Science in Catalysis", *Science* **195** 827-833 (1977).

5 J.P. Dacquin, M. Cabié, C.R. Henry, C. Lancelot, C. Dujardin, S.R. Raouf, P. Granger, "Structural Changes of Nano-Pt Particles During Thermal Aging: Support-Induced Effect and Related Impact on the Catalytic Performances", *J. Catal.* **270** 299-309 (2010).

6 X. Ouyang, S.L. Scott "Mechanism for CO Oxidation Catalyzed by Pd-Substituted $BaCeO_3$, and the Local Structure of the Active Sites", *J. Catal.* **273** 83-91 (2010).

7 M.B. Katz, G.W. Graham, Y.W. Duan, H. Liu, C. Adamo, D.G. Schlom, X.Q. Pan, "Self-Regeneration of Pd-$LaFeO_3$ Catalysts: New Insight from Atomic-Resolution Electron Microscopy", *J. Amer. Chem. Soc.* **133** [45] 18090-18093 (2011).

8 M.B. Katz, S.Y. Zhang, Y.W. Duan, H.J. Wang, M.H. Fang, K. Zhang, B.H. Li, G.W. Graham, X.Q. Pan, "Reversible Precipitation/Dissolution of Precious-Metal Clusters in

Perovskite-Based Catalyst Materials: Bulk Versus Surface Re-Dispersion", *J. Catal.* **293** 145-148 (2012).

9 L. Olsson, E. Fridell, "The Influence of Pt Oxide Formation and Pt Dispersion on the Reactions $NO_2 \leftrightarrow NO + \frac{1}{2} O_2$ over Pt/Al_2O_3 and $Pt/BaO/Al_2O_3$", *J. Catal.* **210** 340-353 (2002).

10 G.W. Graham, H.-W. Jen, W. Chun, H.P. Sun, X.Q. Pan, R.W. McCabe, "Coarsening of Pt Particles in a Model NO_x Trap", *Catal. Lett.* **93** 129-134 (2004).

11 S. Koerfer, R.A. De Souza, H.-I. Yoo, M. Martin, "Diffusion of Sr and Zr in $BaTiO_3$ Single Crystals", *Solid State Sci.* **10** 725-734 (2008).

12 Y. Matsuhisa, M. Taniguchi, M. Uenishi, I. Tan, H. Tanaka, S. Matsueda, K. Narita, A. Hirai, M. Kimura, "Improvement of the Oxygen-Storage Capacity of an Intelligent Catalyst", *SAE Technical Paper* **2008-01-1644** 1-7 (2008).

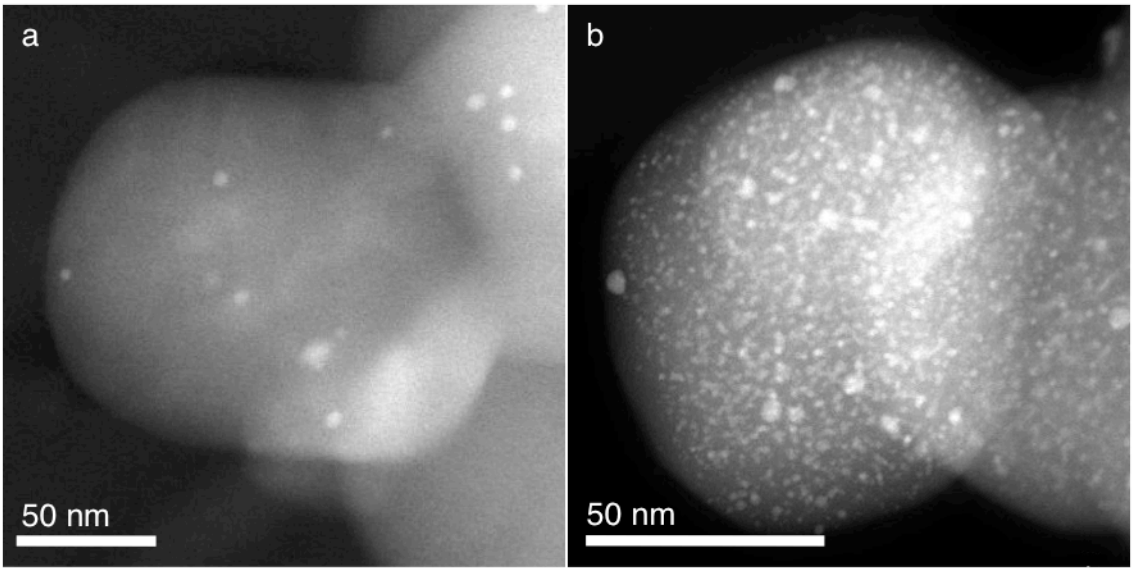

Figure 4.1. HAADF images of Pt-doped perovskite, $CaTi_{0.95}Pt_{0.05}O_{3-\delta}$, particles (a) as freshly prepared and (b) after reduction in 10% H_2/N_2 at 800 °C for 1 h.

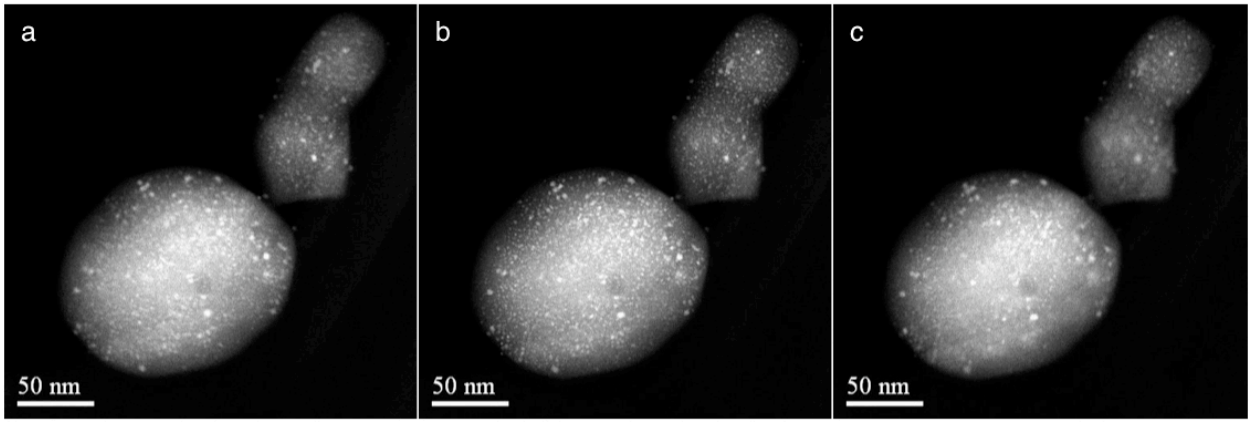

Figure 4.2. A selection of HAADF-STEM images from a $CaTi_{0.95}Pt_{0.05}O_{3-\delta}$ particle after reduction. The focal plane in the images is set at (a) the back of the particle, (b) the middle of the particle, and (c) the front of the particle, with defocus values of -280 nm, -160 nm, and -40 nm, respectively.

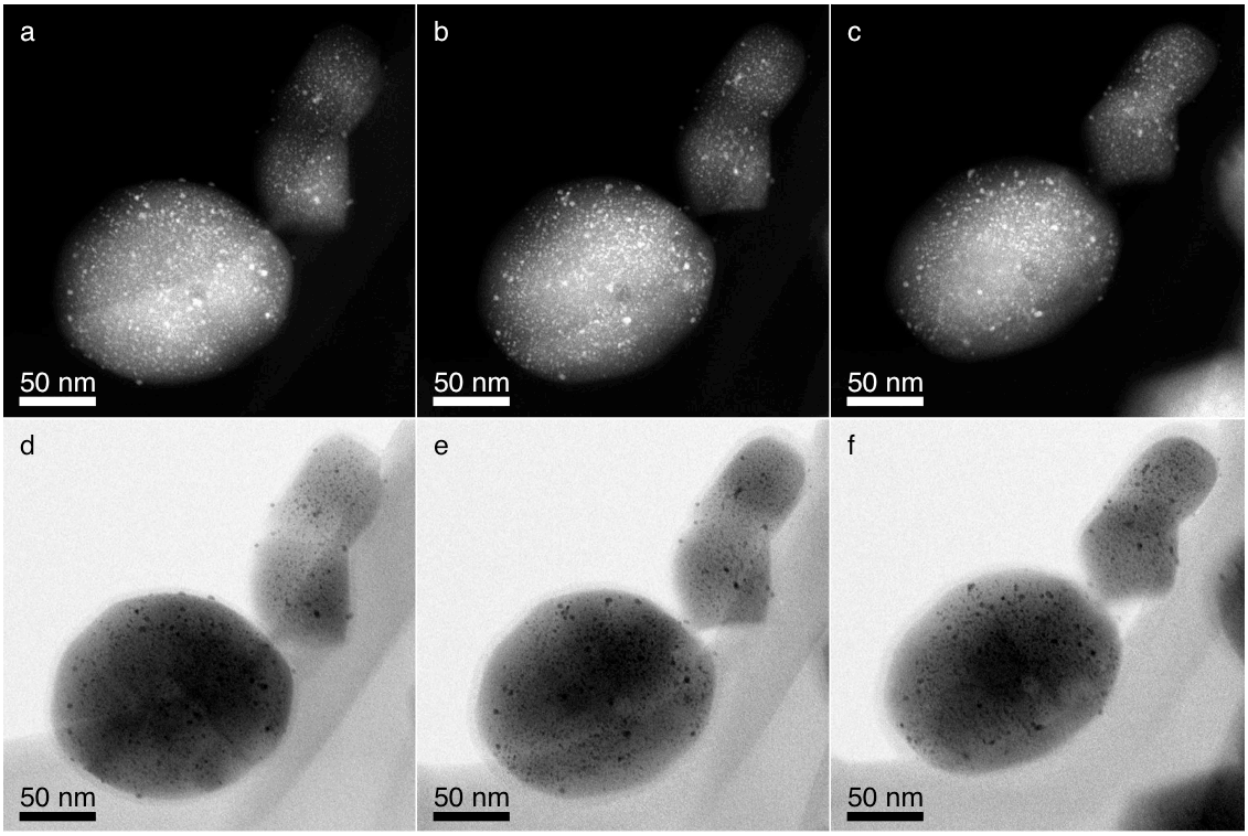

Figure 4.3. A selection of HAADF-STEM and companion bright-field STEM images from the same reduced $CaTi_{0.95}Pt_{0.05}O_{3-\delta}$ particle as in Figure 2 at various tilt angles – (a, d) -20°, (b, e) 0°, and (c, f) 20°.

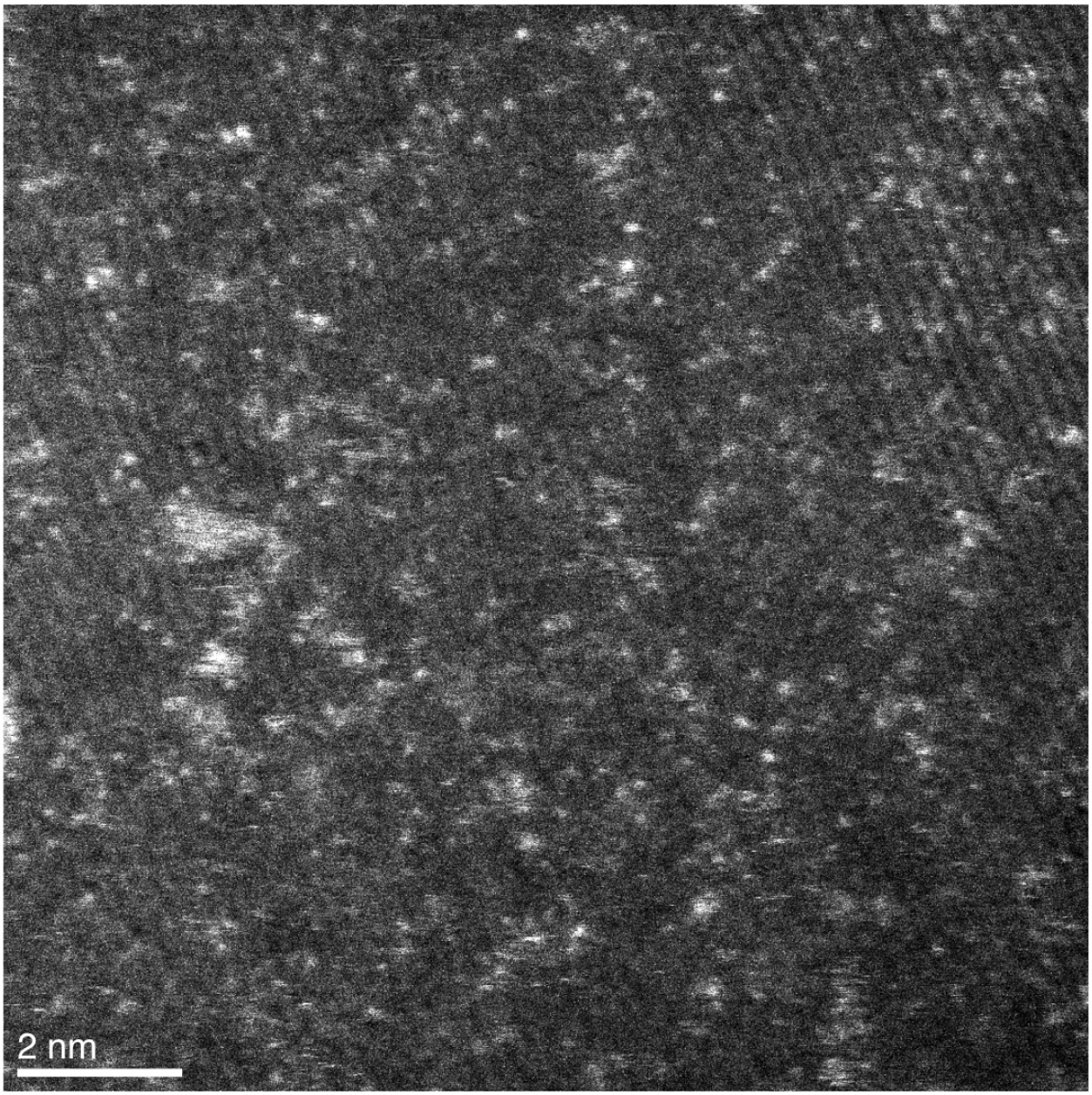

Figure 4.4. Individual Pt atoms dispersed uniformly throughout the $CaTi_{0.95}Pt_{0.05}O_{3-\delta}$ thin film.

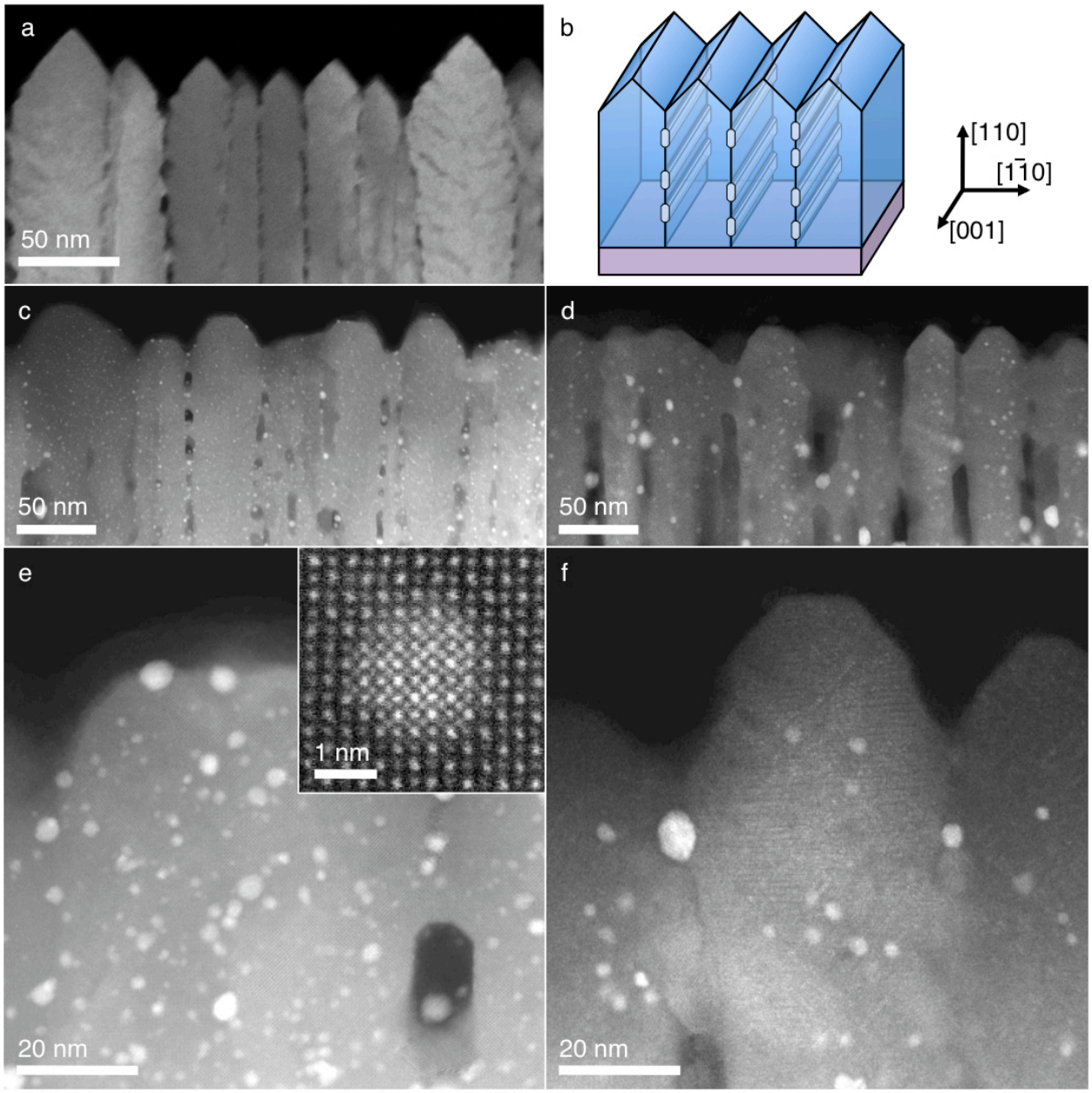

Figure 4.5. (a) HAADF image of the as-grown Pt-doped $CaTiO_3$ film and (b) schematic diagram of the crystal structure and morphology of the lamellar film structure, HAADF images of the film (c,e) after reduction, with an (inset) example of an epitaxial FCC Pt cluster, and (d,f) after subsequent re-oxidation.

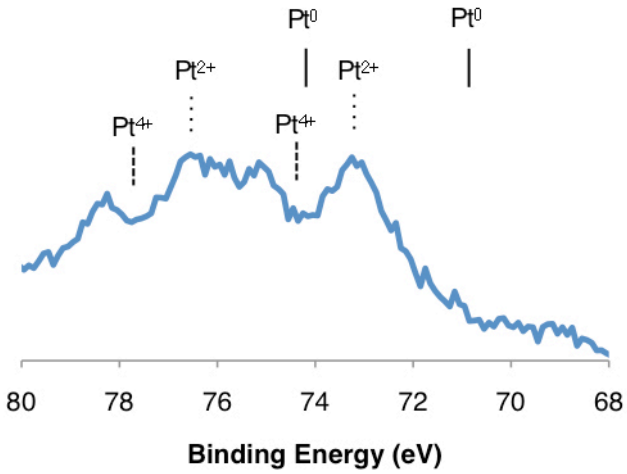

Figure 4.6. XPS spectra of an $CaTiO_3$ (CTO) thin showing strong signals only for Pt in a 2+ oxidation state.

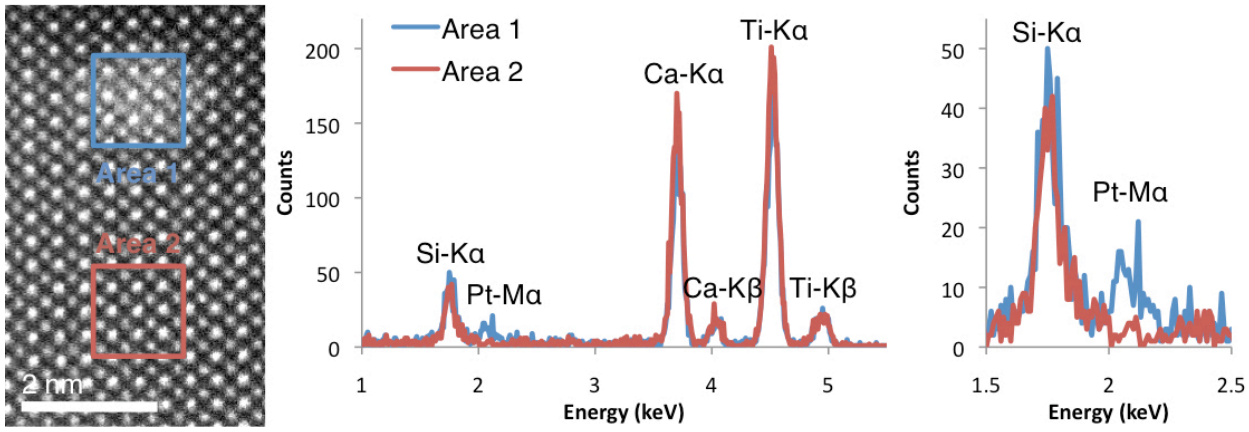

Figure 4.7. A HAADF-STEM image of a diffuse Pt-rich cluster in the $CaTiO_3$ matrix, taken from the reduced Pt-doped $CaTiO_3$ thin film, and XEDS spectra collected from the areas indicated in the image. The spectrum on the right shows the Pt-Mα peak in greater detail. The Si signal is an artifact of the TEM specimen preparation procedure, in which a sacrificial Si crystal is used to protect the thin film from direct ion bombardment during Ar ion milling and may be sputtered to a small degree onto the specimen surface.

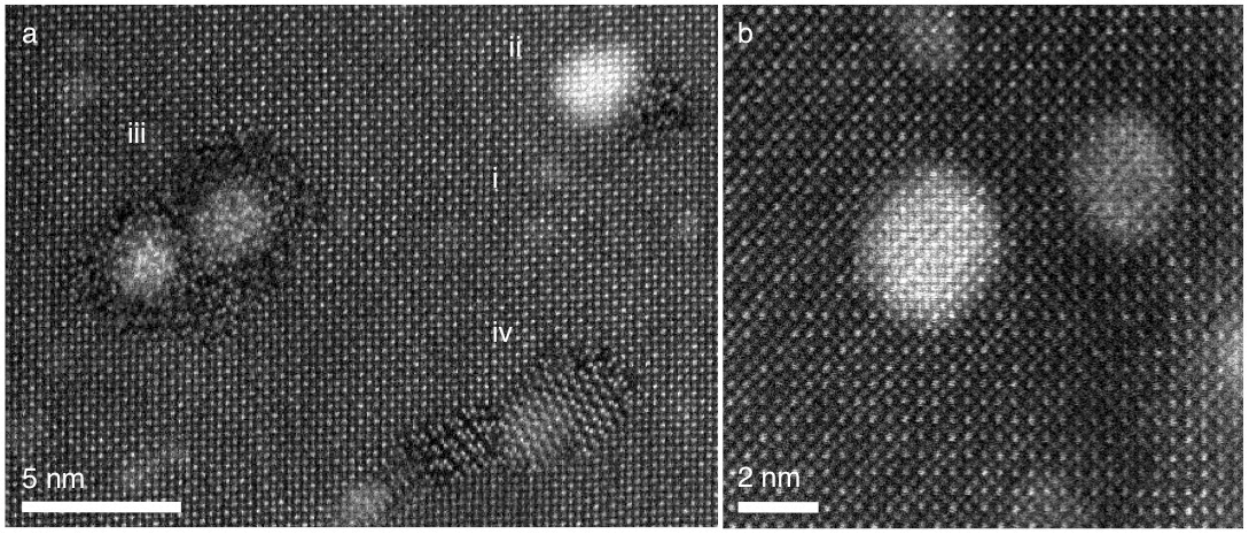

Figure 4.8. (a) A HAADF-STEM image of a region of the reduced Pt-doped $CaTiO_3$ film showing typical examples of (i) small Pt-rich clusters, (ii) an epitaxial FCC Pt cluster, (iii) Pt-rich clusters within a disordered oxide region, and (iv) a region of anatase TiO_2. (b) A HAADF-STEM image of the reduced Rh-doped $CaTiO_3$ film showing typical Rh-rich clusters.

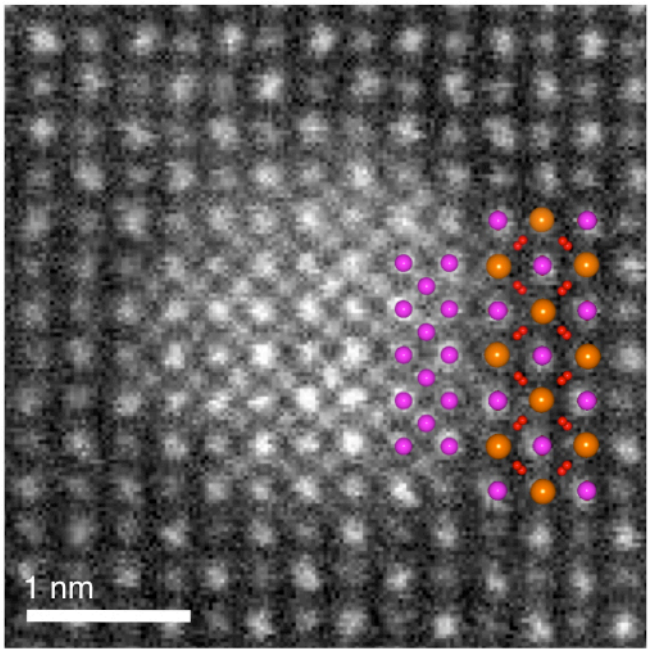

Figure 4.9. An epitaxial FCC Pt cluster within the reduced Pt-doped $CaTiO_3$ thin film with [100] and $[110]_{orthorhombic}$ projections of models of the FCC and perovskite structures, respectively, superimposed. The oxygen ions, which are not visible in the image, appear as dumbbell pairs along this projection because of canting of the oxygen octahedra in the orthorhombic $CaTiO_3$ structure. (Ca = orange, Ti/Pt = purple, O = red)

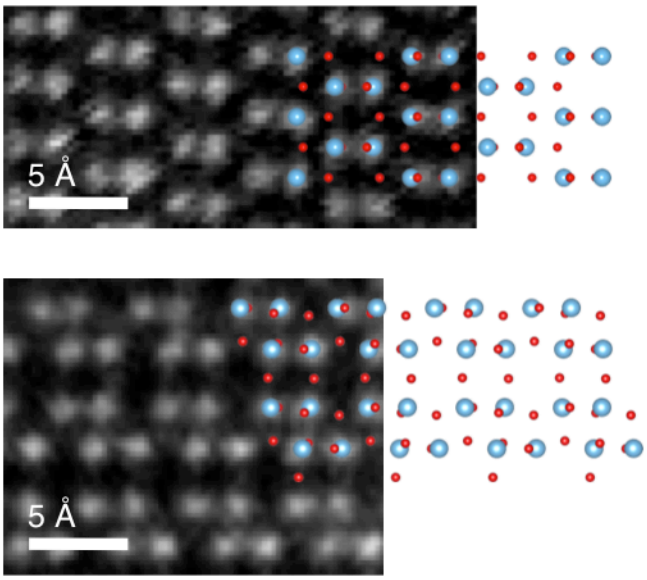

Figure 4.10. An anatase TiO_2 inclusion (top) and a bronze TiO_2 inclusion (bottom) within the reduced Pt-doped $CaTiO_3$ thin film with a [100] projection of a model of the anatase structure superimposed. Oxygen ions are not visible in the image. (Ti = blue, O = red)

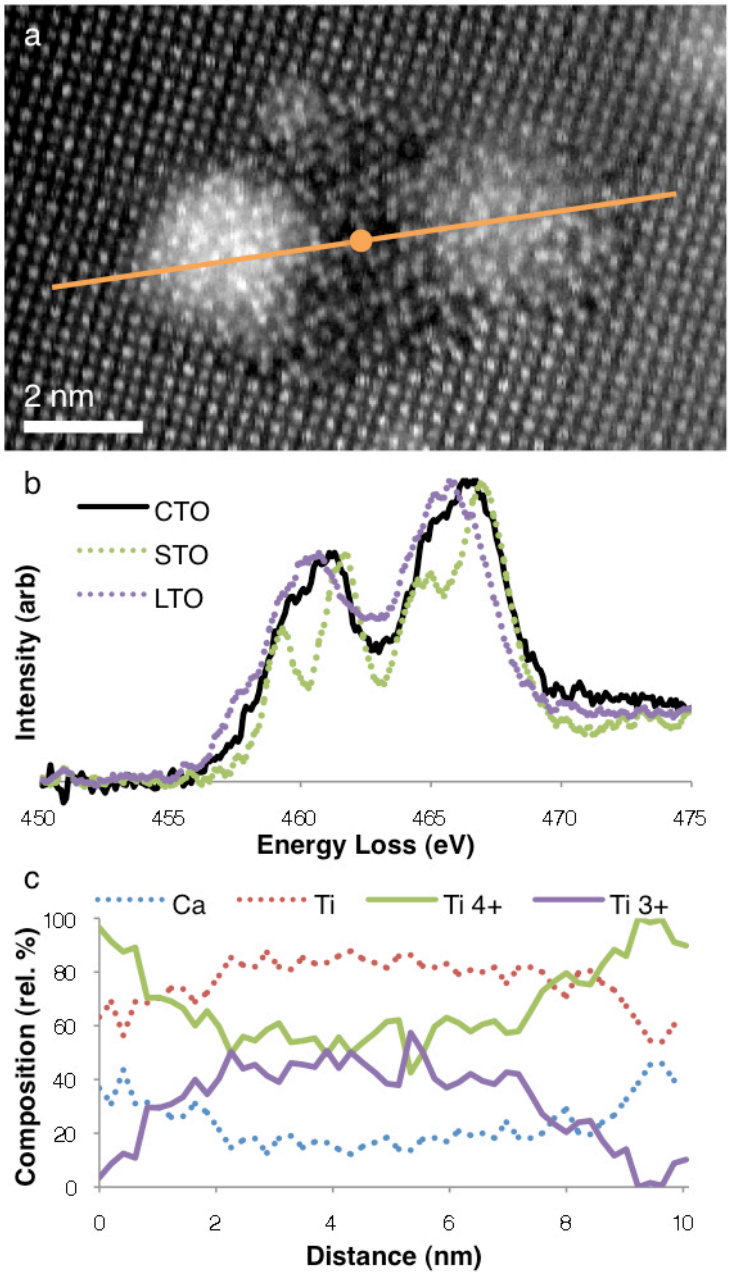

Figure 4.11. (a) A HAADF-STEM image of a region of the reduced Pt-doped $CaTiO_3$ film showing a disordered region of the film containing Pt-rich clusters with (b) a Ti edge spectrum from EELS at the point indicated in (a), accompanied by the $SrTiO_3$ Ti^{4+} and $LaTiO_3$ Ti^{3+} standard spectra, and (c) a line scan from the line in (a) showing a decrease in the oxidation state of Ti coincident with a decrease in the content of Ca relative to Ti.

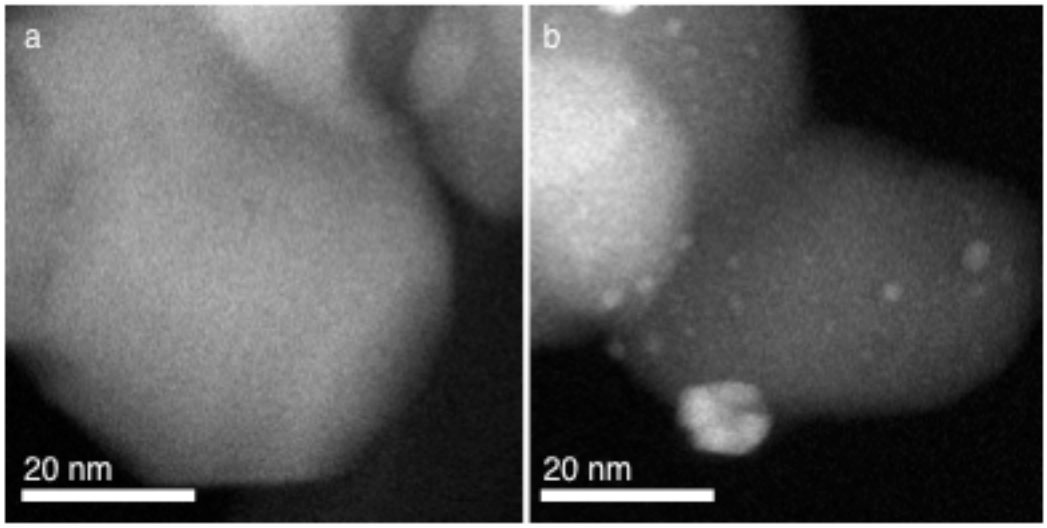

Figure 4.12. Rh-doped $CaTiO_3$ powder (a) as prepared and (b) after reduction.

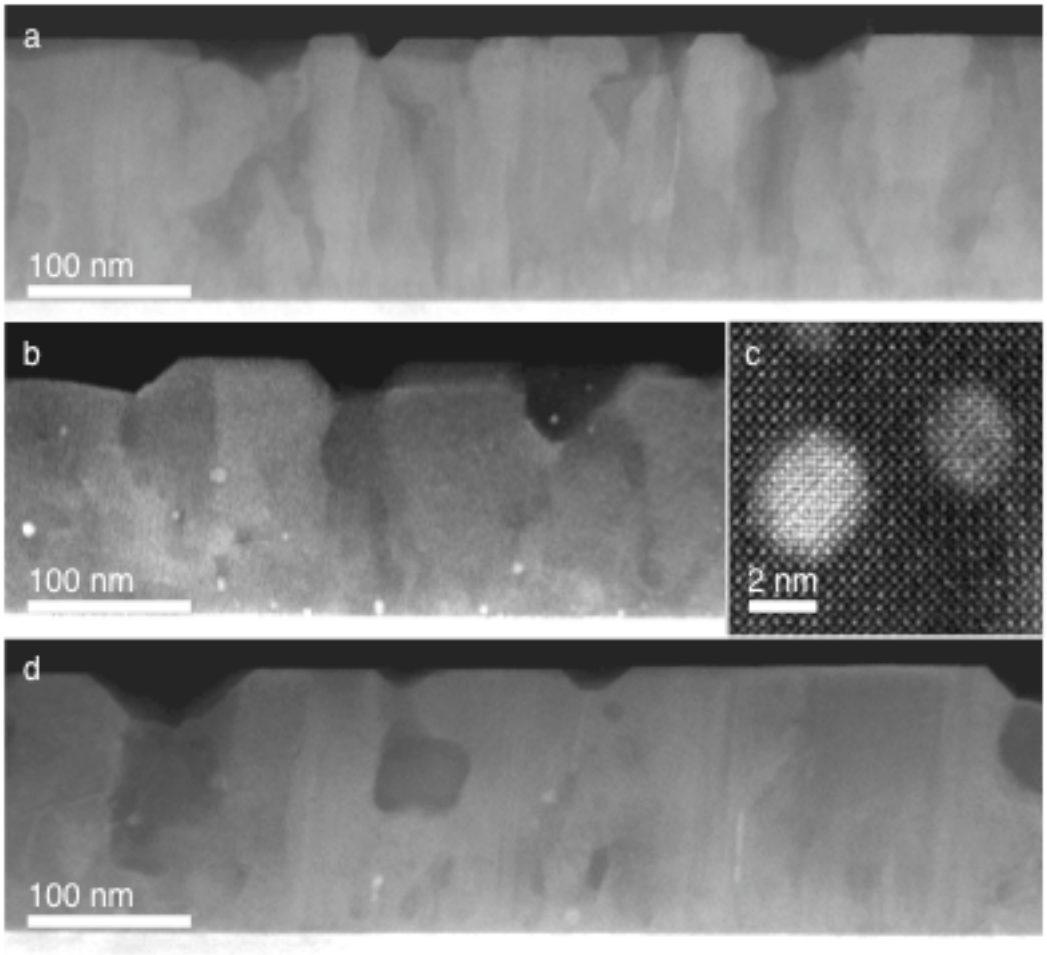

Figure 4.13. Typical regions of the Rh-doped $CaTiO_3$ thin films (a) as prepared, (b, c) after reduction, and (d) after subsequent re-oxidation.

Chapter V

The $CaTiO_3$-Based Self-Regenerative Catalyst

Part II – A Thermodynamic Study

5.1 Introduction and Background

The previous chapter characterized extensively the Pt:$CaTiO_3$ self-regenerative catalyst, based on Daihatsu's formulation of their 'intelligent catalyst',[1-2] in which a host perovskite oxide helps to regenerate the metal catalyst by taking advantage of the cyclical redox environment present in the exhaust stream. There, as reported previously,[3] an unexpected set of phase transformations occurring during redox processing was found, including the formation of TiO_2 phases within the perovskite and the formation of various Pt and/or PtO_x phases. The limited ability of Pt to dissolve into the perovskite under the conditions in this work is counter to assertions in the originating literature of the Pt:$CaTiO_3$ 'intelligent catalyst' system, that could not be explained with a simple model of metallic Pt extrusion and dissolution from a perovskite oxide. This complexity has prompted the present study to fully understand the behavior of the system, in which density functional theory (DFT) and thermodynamic simulations are exploited in an attempt to model the phase equilibria of the Ca-Ti-Pt-O system and elucidate the thermodynamic processes by which these various phases appear and to develop predictive abilities in order to construct a more effective catalyst system.

This chapter presents work resulting from a collaboration between the author and Baihai Li. The varied results from microscopy experiments prompted a theoretical exploration of the phase diagram of the Ca-Ti-Pt-O system, which Dr. Li carried out. He performed this work in his capacity as a visiting scholar in the Pan research group at the University of Michigan under the supervision of Xiaoqing Pan, George Graham, and Anton Van der Ven while sequentially a student and post-doctoral researcher, advised in both cases by Liang (Dennis) Chen, at the Ningbo Institute of Materials Technology and Engineering.

5.2 Methods

5.2.1 Density Functional Theory Modeling

Spin polarized first-principles calculations were performed using the Vienna *Ab initio* Simulation Package (VASP).[4] The electron exchange and correlation were treated within the generalized gradient approximation (GGA) using the Perdew-Wang exchange-correlation functional (PW91).[5] The projector augmented wave (PAW) method[6] was used for the treatment of the core electrons. The soft oxygen potential (O_s, $2s^2 2p^4$, cutoff energy of 250 eV) was used to treat oxygen element in order to use a smaller cutoff energy to obtain the high enough accuracy. The cutoff energy was set to 400 eV for all first-principles calculations and appropriate K-point meshes were chosen for each unit cell to ensure that the force on each atom converged to within 0.02 eV/Å to optimize the atom positions and lattice constants.

The reversible migration of Pt into and out of $CaTiO_3$ is primarily determined by the redox conditions. During redox processing, the system may absorb or release O_2 gas. Thus, the reaction entropy is dominated by the entropy of O_2, and the effect of temperature is effectively governed by the oxygen chemical potential (μ_O) when introducing the temperature into the first-principles

calculations. However, it is well known that conventional first-principles methods overestimate the binding energy of the O_2 molecule, resulting in large errors in the calculations of redox energies.[7-9] In order to compensate for this error, 0.33 eV is added to the total energy of O_2, as suggested by Lee *et al.*[10] μ_O is the key input to control the redox condition. The relationship between μ_O and the temperature (T) and oxygen partial pressure (p) is described by the following equation[11]:

$$\mu_{O_2}(T,p) = \frac{1}{2}\left[\mu_{O_2}(T) + kT\ln(p)\right]$$
$$= \frac{1}{2}kT\left\{-\ln\left[\left(\frac{2\pi(m_1+m_2)kT}{h^2}\right)^{3/2}\frac{kT}{p_0}\right] + \ln\left(\frac{p}{p_0}\right) - \ln\frac{8\pi^2 IkT}{2h^2} + \frac{h\nu}{2kT} + \ln\left(1-e^{-h\nu/kT}\right) - \frac{|D_e|}{kT} - \ln\omega_{e1}\right\} \quad (1)$$

where k is Boltzmann constant, m is the mass of oxygen atom, h is Plank constant, p_0 is the standard atmosphere pressure, I is the moment of inertia, and D_e is the corrected O_2 total energy of -8.75 eV (the VASP calculated total energy is -9.08 eV) in these calculations, which is very close to the value obtained by Lee *et al.*[10] In eqn. (1), the contribution from atomic vibration and electronic excitations is negligible. Eqn. (1) can therefore be rewritten as:

$$\mu_O(T,p) = \frac{1}{2}kT\left\{-\ln\left[\left(\frac{4\pi mkT}{h^2}\right)^{3/2}\frac{kT}{p_0}\right] + \ln\left(\frac{p}{p_0}\right) - \ln\frac{8\pi^2 IkT}{2h^2} - \frac{|D_e|}{kT}\right\} \quad (2)$$

Qualitatively, eqn. (2) indicates that a more positive oxygen chemical (μ_O) potential corresponds to lower temperature (T) and/or higher oxygen partial pressure (p), while a more negative value corresponds to higher T and/or lower p . Also, the oxygen chemical potential can be quantitatively converted to the temperature (T) at a given oxygen partial pressure (p) or to the oxygen partial pressure (p) at a given temperature (T) by this equation.

The relative stability of all the phases was determined first by the formation energy, which is calculated by:

$$\Omega(x_{Ca},x_{Ti},x_{Pt}) = \frac{\left(E_0 - N_{Ca}E_{Ca} - N_{Ti}E_{Ti} - N_{Pt}E_{Pt}\right) - N_O\mu_O}{N_{Ca}+N_{Ti}+N_{Pt}},\ x_i = \frac{N_i}{N_{Ca}+N_{Ti}+N_{Pt}}\left(i = Ca,Ti,Pt\right) \quad (3)$$

where E_0 is the total energy of each phase, E_{Ca}, E_{Ti} and E_{Pt} are the energies per atom in their bulk phases, N_{Ca}, N_{Ti}, N_{Pt}, and N_O are the number of atoms in each phase. The first principles phase diagram at a particular condition can be constructed by taking the convex hull of the formation energy for each phase at a specific μ_O and projecting the stable nodes onto the Ca-Ti-Pt ternary component space.

A combination of well established first-principles calculations and statistical mechanical methods[12-15] was adopted to study the phase stability of the Pt-Ca-Ti-O system. The first-principles energies of a small number of ordered configurations were used as parameters to construct an effective Hamiltonian for the cluster expansion in order to determine the properties of the system. A particular arrangement can be assigned by a spin-like occupation variable σ_i to the chemical species on the lattice site within the host material (i.e., σ_i = +1 and -1 for Pt and Ti, respectively). Thus, the collection of occupation variables $\vec{\sigma} = \left\{\sigma_1,\sigma_2,\sigma_i \ldots \sigma_m\right\}$ can be used to uniquely determine the configuration of Pt-Ca-Ti-O system. Within the cluster expansion formalism, the configurational energy of the system can be expanded in terms of polynomials of σ_i:

$$E\left(\vec{\sigma}\right) = V_0 + \sum_i V_i\sigma_i + \sum_{i,j} V_{ij}\sigma_i\sigma_j + \sum_{i,j,k} V_{ijk}\sigma_i\sigma_j\sigma_k + \ldots \quad (4)$$

where the interaction coefficients V_i, V_{ij}, V_{ijk}, *etc.* are referred to as effective cluster interactions (ECIs) for all pairs, triplets, quadruplets, *etc*. The expansion can be formally extended over all

possible clusters of sites within Pt-Ca-Ti-O system. In practice, however, the above cluster expansion must be truncated above some maximum sized cluster and keep the physical properties well. The values of the effective coefficients were determined by fitting eqn. (4) to the first-principles energies of the subset of the selected configurations using a root mean square method. By using a genetic algorithm,[16] an optimal effective coefficient can be obtained which optimizes the cross-validation (CV) score, a criterion for the quality of the cluster expansion in predicting energies not included in the fit.[12,17,18] With the set of optimal ECIs and the effective Hamiltonian, the optimal set of clusters are obtained. Subjecting the resultant ECI to the grand canonical Monte Carlo simulations to calculate the free energies at finite temperatures and the phase equilibrium of the system, the relationship between the oxygen chemical potential and Pt concentration in the perovskite matrix can be revealed.

5.2.2 Thin Film Sample Preparation and Microscopy

Pulsed laser deposition (PLD) targets were constructed from $CaTi_{0.95}Pt_{0.05}O_3$ and $Ca_{1.1}Ti_{0.9}Pt_{0.1}O_3$ (high titanium and low titanium, or high-Ti and low-Ti, respectively) powders, which were synthesized using the citrate method. Stoichiometric amounts of $Ca(NO_3)_2 \bullet 4H_2O$, $Ti[O(CH_2)_3CH_3]_4$, and $PtC_{10}H_{14}O_4$ (Alfa Aesar) were dissolved in de-ionized water with citric acid, with nitric acid used to control the solution pH. The solution was dehydrated at 100 °C and held at 60 °C until gelation, after which it was calcined at 800 °C in flowing oxygen. The resultant powder was then pressed and sintered at 1200-1300 °C to form a dense PLD target. Film growth was performed in an ultra-high vacuum growth chamber using a KrF excimer laser operated at 248 nm, with Pt:$CaTiO_3$ films grown at both 600 °C and 750 °C. $LaAlO_3$ (110) and $SrTiO_3$ (100) single crystal substrates were supplied by MTI Corporation.

Thermal processing was performed in a quartz tube in a tube furnace. Dry air was flowed through the tube at 450 sccm and 10% H_2 (balance N_2) at 100 sccm for oxidation and reduction treatments, respectively. These conditions mimic those in the original work.[2]

Cross-sectional STEM specimens were then fabricated by mechanical thinning and polishing on diamond lapping media, followed by Ar-ion milling (Gatan PIPS, model 691) to electron transparency. Specimens were examined in a C_s-corrected JEOL JEM-2100F STEM operated at 200 kV and equipped with EELS and XEDS detectors. WDS analyses were performed on a Cameca SX-100 Electron Microprobe Analyzer.

5.3 Results and Discussion

5.3.1 Analytical Microscopy

The Pt:$CaTiO_3$ epitaxial thin films, as grown, were a homogeneous and comprised a single perovskite phase. STEM examination revealed no second phases and no Pt segregation. The high-temperature films (T_g = 750 °C) were smooth, whereas the low-temperature films (T_g = 600 °C) were lamellar, as has previously been reported,[3] with the lamellae aligning along the beam direction, hence manifesting as an apparent columnar structure in the HAADF-STEM cross-sectional images. Morphology aside, the films appear identical at the atomic scale and behave in a congruent fashion upon redox aging.

The thin films were exposed to reducing conditions (800 °C, 10% H_2/N_2, 1 h) in order to induce the extrusion of metallic Pt from the perovskite matrix. As already discussed and shown again in Figure 5.1, the metal does not to exit the perovskite to a free surface (to any significant degree above that expected by random chance), as prior literature asserts, but coalesces into Pt-clusters

of varying size and character within the oxide matrix itself. The majority of Pt clusters are 1-2 nm in diameter and appear in images simply as a diffuse, but definite increase in the HAADF-STEM contrast, though their chemical identity as Pt has been confirmed by XEDS. Typical examples are shown in Figure 5.2. The phase identity of these smallest clusters, however, remains unknown because of the lack of a distinct crystal structure in the images. This alone does not discount the possibility of crystallinity, as it could simply be lacking a favorable zone axis alignment with the electron probe, but leaves open the possibility (through analysis of images alone) of the clusters being any of the following: a metallic Pt particle, any oxide of Pt, a high local concentration of Pt_{Ti}-substituted perovskite (*i.e.* $CaPtO_3$), or a cluster of interstitial Pt. The assumption, however, owing to the reducing nature and high temperature of the reduction treatment, is that these clusters are indeed metallic. Also present are 1-3 nm fcc Pt particles that are epitaxial to the surrounding perovskite matrix with orientation relationships of either $[100](010)_{Pt}||[100](010)_{CTO}$ (cube-on-cube epitaxy) or $[100](011)_{Pt}||[100](010)_{CTO}$ (45° rotation about a primary axis), with the $CaTiO_3$ crystal treated for this purpose as pseudocubic. Finally, there is a population of 2-5 nm non-epitaxial fcc Pt particles that form both on the free surfaces (and inter-lamellar surfaces of the low-temperature film) and on internal defect surfaces.

The oxide itself in the high-Ti films also underwent significant local phase transformations in the vicinity of the Pt clusters which had nucleated upon reduction. Small 2-15 nm regions of second phases formed epitaxially to the surrounding perovskite matrix. These phases were identified as the anatase phase and bronze phases of TiO_2 [TiO_2 (A) and TiO_2 (B), respectively], shown in Figure 5.3, by their crystal structure as imaged in HAADF-STEM and their stoichiometry – the absence of Ca relative to the surrounding matrix – as probed by EELS.

Also present was a Ca-doped variant of the bronze phase, identified for the first time in this work and shown in Figure 5.4a (from a film grown from a $CaTi_4O_9$ PLD target). Based on the atomic column motifs present in the images, as well as its proximity and epitaxiality with the TiO_2 (B) structures within the film, it is clearly related to TiO_2 (B). It possesses, however, two peculiarities beyond that of TiO_2 (B) as generally described in the literature.[19,20] The first is that the slabs of edge-sharing TiO_6 octahedra are repeatedly twinned from slab to slab, to the extent that it can be thought of as a superlattice. The second is that there is, between slabs, an entire row of atomic columns that are not accounted for by the TiO_2 (B) crystal structure, twinned or otherwise.

Subsequent experiments exploring this crystal structure, though not fully presented in this dissertation, were able to reproduce large crystals of this modified TiO_2 (B) structure, always twinned and always with an intercalated row of atoms. The intercalated row of atoms, however, in HAADF-STEM imaging, appear to alternate in contrast between columns that are approximately as bright as the adjacent Ti-O columns of TiO_2 (B), and columns that are dimmer. Because HAADF-STEM contrast is roughly proportional to the atomic number of the atom being probed, these columns either possess fewer Ti atoms than adjacent rows, or are not Ti.

Atomic-resolution EELS mapping, shown in Figure 5.4b indicated these columns to likely be Ca, rather than Ti. That chemical analysis, coupled with images from two of the three primary crystal direction and informed by the structure of TiO_2 (B), composed enough information to create a crystal model of the structure in question. The formula unit is $CaTi_5O_{11}$, and the structure is essentially two TiO_2 (B) slab structures twinned, pulled apart, and stabilized by the

addition of one Ti, one Ca, and one O per formula unit. Alternatively, it's the addition of two each of Ca, Ti, and O per TiO_2 (B) unit cell. The intercalated Ti and O form TiO_2 octahedra and the Ca is essentially dodecahedrally coordinated. An image of the crystal model is shown in Figure 5.4c, along with HAADF-STEM image simulations. The formation energy of the structure was then calculated using DFT and turned out to be remarkably low. The simulated images of the constructed crystal were compared to the experimental images to further confirm the identity of this previously unknown phase.

A further unexpected phenomenon was the appearance of small 2-10 nm regions in which the crystalline ordering has degraded, shown in Figure 5.5. These disordered regions nearly universally surround or are adjacent to Pt clusters. Upon close examination, very small areas of the disordered regions, comprising only several atomic columns, appear to take on crystalline motifs resembling those of the TiO_2 (A) and TiO_2 (B) structures, principally projected bond distances and angles. ELNES reveals a decrease in Ca content with a commensurate increase in the fraction of Ti^{3+} relative to Ti^{4+}. It is worth noting again that these titanate phases formed only in the high-Ti films synthesized from the $CaTi_{0.95}Pt_{0.05}O_3$ target and not in the low-Ti films from the $Ca_{1.1}Ti_{0.9}Pt_{0.1}O_3$ target. That latter contained only the Pt-associated formations.

It is notable that, while several phases of TiO_2 and Ti-enriched regions were found and identified, analogous regions of high Ca concentration were not identified. The most likely phase for Ca to take up would be the rock salt phase, none of which was identified from HAADF-STEM imaging. Furthermore, EELS energy-filtered imaging, shown in Figure 5.6, revealed no high-Ca regions in the film above the perovskite background, only low-Ca regions corresponding to the TiO_2 phase and disordered regions. The stoichiometry of the thin film, as well as the

originating PLD target was therefore determined experimentally by XWDS. Though the target had a nominal stoichiometry of $Ca_{0.958}Ti_{0.979}Pt_{0.042}O_3$ (cation concentrations normalized to a fully oxygenated state), close to the desired $CaTi_{0.95}Pt_{0.05}O_3$, the resultant thin film had a stoichiometry of $Ca_{0.858}Ti_{1.057}Pt_{0.014}O_3$. It is apparent that Ti was less volatile or had a higher affinity for the substrate during growth than Ca and Pt.

The thin films were then exposed to a subsequent oxidation treatment (800 °C, 20% O_2/N_2, 1 h) in order to induce dissolution of the Pt clusters into the perovskite phase. Most of the very small (1-2 nm) Pt clusters have dissolved into the perovskite and no longer appear under HAADF-STEM imaging, as shown in Figure 5.7. There still remain, however, some larger (2-3 nm) internal Pt clusters and most of the metallic Pt particles that had formed along internal surfaces during reduction. The metallic Pt particles that had formed on the free surfaces of the lamellar film have coarsened into larger particles, which is expected given the well-known tendency of metallic Pt to coarsen under oxidizing conditions. Gone also are the disordered regions, having presumably re-crystallized into either into a TiO_2 phase or reformed into the perovskite phase. The details of these transformations, after both reduction and re-oxidation, are presented in Ref. 3.

5.3.2 Construction of Calculated Phase Diagrams

Because the main conceit of the self-regenerative concept is the reversible dissolution of Pt into the $CaTiO_3$ perovskite structure, substituting for Ti on the perovskite b-site, the first step in constructing equilibrium pseudo-ternary phase diagrams of the PtO_x-CaO_y-TiO_z system is necessarily to perform a cluster expansion calculation of the $CaTi_{1-x}Pt_xO_3$ family of compositions. The comparison between the predicted and first-principles formation energies shows that the

cluster expansion is sufficiently converged and accurately reproduces the first-principles ground states, as shown in Figure 5.8. This calculation attests that the $CaTiO_3$ and $CaPtO_3$ end members are effectively miscible in each other, forming a solid solution. The Pt chemical potential, as shown in Figure 5.8, smoothly increases as a function of Pt concentration, with no kinks between the two end member compositions within the range of 100-800 °C.

In the validation process, 28 clusters consisting of the empty and point, 11 pairs, 9 triplets and 6 quadruplets were selected out of 92 candidates to fit the ECIs. The weighted (CV) score for the cluster expansion is 3.3 meV/f.u. (f.u. = formula unit) with a root mean square (rms) error of 1.4 meV/f.u. However, the formation energies of the ground states are only several meV/f.u. lower than that of the excitation states, which likely results in the $CaTi_{1-x}Pt_xO_3$ ordered phase becoming a disordered solid solution at elevated temperatures. This presumption was then corroborated by grand canonical Monte Carlo simulations.

The Gibbs formation energy of $CaTi_{1-x}Pt_xO_3$ system was calculated by integrating Pt chemical potential at a fixed temperature according to:

$$\Omega_{CTPO} = \frac{xE_{CaPtO_3} + (1-x)E_{CaTiO_3} + \int_0^x \mu_{Pt}dx - E_{Ca} - xE_{Pt} - (1-x)E_{Ti} - 3\mu_O}{2}, 0 \le x \le 1 \qquad (5)$$

where E_{CaTiO_3} and E_{CaTiO_3} are the total energies of one formula unit of $CaTiO_3$ and $CaPtO_3$, respectively, with μ_{Pt}, μ_O, and x are the Pt chemical potential in Monte Carlo simulations, oxygen chemical potential related to the external temperature, and oxygen partial pressure, the concentration of Pt in one formula unit of $CaTi_{1-x}Pt_xO_3$, respectively, and E_{Ca}, E_{Ti} and E_{Pt} are the energies for each atom in their bulk phases. The value of denominator is determined by

$N_{Ca}+N_{Ti}+N_{Pt}=2$ in one formula unit of $CaTi_{1-x}Pt_xO_3$. The calculated Gibbs formation energies were then combined with first-principles formation energies of other phases to construct the ternary phase diagrams. The $CaTi_{1-x}Pt_xO_3$ phase can thus be considered to be a continuously variable solid solution for all conditions considered.

Primary attention was focused on the evolution of phases at temperatures between 100 °C and 800 °C, mirroring those temperatures accessed during the experiments, and in oxygen partial pressures (P_{O_2}) of 0.2 and 1×10^{-8} atm, representing oxidizing and reducing conditions, respectively. Pseudo-ternary phase diagrams can now be constructed based on the calculated equilibrium stabilities of all compounds reported to exist within the Ca-Ti-Pt-O system. Stoichiometric, cation-defective, and anion-defective crystal structures, including orthorhombic, cubic, and tetragonal $CaTiO_3$; the Ruddlesden-Popper-type $Ca_3Ti_2O_7$ and $Ca_4Ti_3O_{10}$; $CaTi_2O_4$, the newly characterized structure of $CaTi_5O_{11}$, anatase TiO_2 [TiO_2 (A)], rutile TiO_2 [TiO_2 (R)], brookite TiO_2 [TiO_2 (B')] and bronze TiO_2 [TiO_2 (B)], TiO, Ti_2O_3, Ti_3O_5, CaO, *etc.*, are taken into account to construct the first-principles phase diagram of Ca-Ti-O system.

The first-principles phase diagrams of Ca-Ti-O under redox environments are shown in Figure 5.9, where the hcp Ti and fcc Ca are chosen as the references. Oxygen partial pressure was fixed at 0.2 p_0, which is close to the oxygen partial pressure in air, to investigate the phase diagrams change as a function of temperature. TiO_2 (A), orthorhombic $CaTiO_3$, $CaTi_5O_{11}$, and CaO are stable under the oxidizing conditions (100 °C, 0.2 p_0). The relative stability of TiO_2 phases is in the order of TiO_2 (R) < TiO_2 (B') < TiO_2 (B) < TiO_2 (A), and the total energies of the three less stable structures are 89.7, 52.1 and 13.5 meV/f.u. higher than that of TiO_2 (A), respectively. The result that TiO_2 (A) is more stable than TiO_2 (R) at low temperature is

consistent with the observation by Savaloni *et al.*[21] When the temperature increases to 800 °C, these four phases remain and no additional phases appear – the formation energies of the existing phases simply becomes less negative. Reduced structures with ordered oxygen vacancies were calculated as well, but are not energetically favorable and do not appear in the calculated phase diagrams. It can be expected that disordered oxygen vacancies may appear at the $CaTiO_3$ surface in experiments, but, as this is not a bulk phase, it is not considered. Ordered cation defect phases are also energetically unfavorable, thus these structures do not appear in the phase diagrams under the environments considered. TiO_2 (A) gives way to Ti_2O_3, and $CaTi_5O_{11}$ disappears from the phase diagram under aggressively reducing conditions (*e.g.* 800 °C, 10^{-20} p_0). Further reduction leads to the formation of $CaTi_2O_4$ at the expense of orthorhombic $CaTiO_3$.

Because entropy and the various excitations – vibrational, configurational, and electronic – are not considered in first-principles calculations, some discrepancies between first-principles calculations and experimental phase diagrams obtained at non-zero temperatures are to be expected. This manifests in the Ruddlesden-Popper-type $Ca_3Ti_2O_7$ and $Ca_4Ti_3O_{10}$ phases, which have been found experimentally,[22] not appearing in the first-principles-derived phase diagrams. It is not expect, however, that this discrepancy is critical for the expanded investigations of phase stability and evolution of the Pt-Ca-Ti-O system, as these structures were also absent in the experimental systems.

The first-principles calculated isothermal phase diagrams of the four-component Pt-Ca-Ti-O system manifests as a three-dimensional convex hull. In order to conveniently display and interpret the results, the convex hull was projected onto a two-dimensional pseudo-ternary phase

diagram, holding constant the oxygen content vis-à-vis the oxygen chemical potential. In agreement with the phase diagram of Ca-Ti-O system, TiO_2 (A), $CaTiO_3$ (orthorhombic), $CaTi_5O_{11}$, CaO also appear in the Pt-Ca-Ti-O diagram. Additionally, Ca_4PtO_6 (*R-3cH*, 167) has been observed in the range of 667 ~ 1127 °C by Jacob *et al.* in the Ca-Pt-O system.[23] Indeed, this structure is a stable phase in the calculated phase diagram under the considered redox conditions.

Additional structures involving Pt single atoms and dimers doped at cation and interstitial sites of stoichiometric and reduced $CaTiO_3$, TiO_2 species, Ti_2O_3, as well as Pt-Ti and Pt-Ca binary crystals, Pt oxides, *etc.*, are included to construct the Pt-Ca-Ti-O phase diagrams. A full accounting of all phases calculated and considered for this study can be found in Table 1. Phase stabilities were calculated and subsequently used to construct phase diagrams at intervals of 100 °C for P_{O_2} = 0.2 atm and between 100 °C and 800 °C for $P_{O_2} = 1\times10^{-8}$ atm, and are shown in Figures 5.10 and 5.11.

Under reducing conditions, the phase diagram at 100 °C features TiO_2 (A), PtO_2, and CaO as the ternary end members, with $CaPtO_3$, $CaTiO_3$, Ca_4PtO_6, and $CaTi_5O_{11}$ (a TiO_2 (B)-related structure) also appearing, $CaPtO_3$ and $CaTiO_3$ coexisting as a solid solution, notated as $CaTi_{1-x}Pt_xO_3$. The shape of the phase fields do not much change as temperature is increased, though the stable PtO_x end member becomes Pt_3O_4 by 400 °C and Pt by 500 °C. Above 500 °C, the platinated form of $CaTi_{1-x}Pt_xO_3$ begins to destabilize relative to Pt and CaO, with Pt gradually becoming less soluble with increasing temperature, until by 700 °C, it no longer forms. As well by 700 °C, Ca_4PtO_6 is no longer stable. At all temperatures at which the $CaTi_{1-x}Pt_xO_3$

phase is stable, it exists in two-phase equilibria with CaO or Ca_4PtO_6 and with the PtO_x end member.

A similar phase field configuration persists for the phase diagram evolution under oxidizing conditions – the low-temperature diagrams are identical to the reducing phase diagrams. In this case, though, the Pt_3O_4 and Pt phases do not appear until above 700 °C and 900 °C, respectively, with the fully platinated perovskite phase remaining stable until above 1000 °C and partially platinated perovskite existing even above 1200 °C, the highest temperature calculated. The Ca_4PtO_6 phase is stable until 1100 °C.

These phase diagrams, however, present a problem, as they cannot accurately reflect the experimental data presented above. The nominal composition of the thin films puts the material slightly within the $PtO_2/Pt_3O_4/Pt\text{-}CaTiO_3\text{-}CaTi_5O_{11}$ phase field, which remains unaltered throughout the temperatures and oxygen partial pressured sampled in the calculated phase diagrams. The experimental data would dictate that there should exist some temperature at which Pt is soluble in the perovskite phase under oxidizing conditions and insoluble under reducing conditions.

Since all phases reported to exist within the Ca-Ti-Pt-O quaternary system can potentially appear in the phase diagrams, kinetics is considered as playing a role in preventing certain phases from forming. Oxides of Pt, for instance, are well known to be difficult to form,[24] despite their relatively lower free energies. Additionally, no accounting in the phase diagrams presented here is made for surface energies. The low-strain epitaxial nature of the $Pt/CaTiO_3$ interface likely serves to stabilize Pt's metallic phase. Since it furthermore cannot be confirmed experimentally

that Pt exists as a simple oxide in any of the thin film specimens, those phases are thus eliminated from contention and redraw the phase diagrams.

Though the end-member phases present in these new phase diagrams are the same, save for the substitution of metallic Pt for its simple oxides, the phase field layout is substantially different. For reducing conditions, shown in Figure 5.12, the $CaTi_{1-x}Pt_xO_3$ phase now forms two-phase coexistence regions with TiO_2 (A) and $CaTi_5O_{11}$ rather than with the Pt at lower temperatures, though starts to form two-phase regions with Pt, starting with the more heavily platinated end of the $CaTi_{1-x}Pt_xO_3$ above 300 °C, finishing the shift by 500 °C. The Pt-heavy end of the $CaTi_{1-x}Pt_xO_3$ phase gives way to more energetically favorable Pt and CaO above 500 °C, with none but the non-platinated $CaTiO_3$ perovskite remaining by 700 °C. The phase diagrams, shown in Figure 5.13, are again largely the same for oxidizing conditions, though generally shifted to higher temperatures.

This set of phase diagrams is in good agreement with experimental observations, much more so than the phase diagrams containing oxides of platinum. The most important feature in regard to the self-regenerative catalyst concept is the existence of a set of nominal compositions that, at engine operating temperatures, are in two-phase regions with Pt completely dissolved in host oxides under oxidizing conditions and are in three-phase regions where those oxides are in equilibrium with free Pt metal under reducing conditions. This modulation in the shape of the phase fields with changing oxygen partial pressure is the mechanism behind the self-regenerating effect. It is in fact the extent of movement of the edge of the two-phase $CaTi_{1-x}Pt_xO_3$-TiO_2 region toward and away from the Pt corner of the phase diagram that determines the extent to which Pt can be loaded into and reclaimed from the perovskite.

In both the reduced and oxidized conditions, the high-Ti catalyst formulation should form only perovskite, metallic Pt, and $CaTi_5O_{11}$, according to the calculated phase diagrams. This is somewhat contrary to the experimental results, in which TiO_2 (A) also appears, as well as the appearance of the TiO_2 (B) base structure of $CaTi_5O_{11}$. Both of these can be partially explained by $CaTi_5O_{11}$ being kinetically more difficult to form, owing to its large unit cell, resulting in the formation of the simpler TiO_2 (B) variant. Additionally, both bronze-related phases have less suitable epitaxy with $CaTiO_3$ than TiO_2 (A). Therefore, though thermodynamically stable in the bulk, the formation of bronze-related phases will defer to that of TiO_2 (A) given the small sizes of the minority phase domains, which are mechanically pinned on all sides and would likely shift energetic favorability toward TiO_2 (A).

It is worth noting that the assumed oxygen partial pressure of 1×10^{-8} atm during reduction may be higher than that of the real reducing condition in these experiments (*i.e.* flowing 10% H_2/N_2). The evolution of phase diagrams with decreasing oxygen partial pressure at fixed 800 °C (Figure 5.14) was therefore investigated. Calculations show that there is no phase disappearing or new phase appearing at the range of 1×10^{-8} - 1×10^{-20} atm until the bimetallic structure Pt_8Ti_1 shows up at 1×10^{-20} p_0. Under even more aggressively reducing condition, the Pt-Ca bimetallic alloy (Ca_1Pt_5 and Ca_2Pt_4), followed by Pt_5Ti_3 appear in the phase diagrams gradually. TiO_2 (A) can be reduced to Ti_2O_3 while $CaTi_5O_{11}$ disappears at 1×10^{-28} atm. $CaTiO_3$ could be reduced to be $CaTi_2O_4$ at extremely low oxygen partial pressure, but, as this was not seen in the experiments, that can be taken as a lower bound to the oxygen content

5.3.3 Informed Synthesis of a Self-Regenerative Catalyst

Using the knowledge gained from this study, specifically from the calculated phase diagrams, a theoretically maximally effective self-regenerative catalyst may be intelligently designed to contain the maximum Pt loading that could be expected to be stabilized by the $CaTiO_3$ support. That is, the phase diagrams may be used as a guide to maximally utilize the support for a prescribed amount of Pt at the expected use temperature without oversaturating the support during oxidation-induced dissolution.

For the purposes of this discussion, the operating temperature will be presumed to be 800 °C. If a catalyst could be made with a stoichiometry of exactly $CaTi_{1-x}Pt_xO_3$, *i.e.* on the line precisely between $CaTiO_3$ and $CaPtO_3$, any amount of Pt could, in principle, be used. This would result in an oscillation between a totally perovskite microstructure and a three-phase mixture of $CaTiO_3$, Pt, and CaO under oxidizing and reducing conditions, respectively.

One could alternatively, though, simply add Pt to an already stoichiometric formulation of $CaTiO_3$. This scenario, is, in fact, closer to the materials discussed in this report. In this case, Pt could be added to the extent such that the nominal stoichiometry (assuming it is fully oxygenated) is $CaTiPt_{0.18}O_{3.36}$, *i.e.* Pt comprising 8% of cations. In this situation, the reduced catalyst would, according to the phase diagrams, comprise $CaTiO_3$, Pt, and $CaTi_5O_{11}$, with the oxidized catalyst comprising $CaTi_xPt_{1-x}O_3$ and $CaTi_5O_{11}$.

The perovskite could support more Pt catalyst at lower operating temperatures, as the Pt solubility in the $CaTi_xPt_{1-x}O_3$-$CaTi_5O_{11}$ two-phase coexistence is greatly increased, but that could prove detrimental to the catalyst system for a number of reasons. Higher operating

temperatures are a necessary result of placing the catalyst nearer to the engine in the exhaust stream in order to facilitate cold-start light-off. Kinetics are also commensurately slowed at lower temperatures, likely limiting the self-regeneration effect and therefore the practicality of the catalyst. Finally, it is unknown based on this and previous studies whether a higher fraction of Pt within the support will lead to more efficient catalysis, or how supports with varying amounts of Pt loading will survive extended cycling tests. Further studies will need to be completed to conclusively determine the useful viability of this catalyst and other similar self-regenerative catalysts.

5.4 Conclusions

The phase evolution of the Ca-Ti-Pt-O system has been studied by advanced atomic-resolution transmission electron microscopy and density functional theory calculations in order to gauge its usefulness as an automotive three-way catalyst. First-principles simulations were used to calculate the formation energies of phases in this quaternary system. From those energies, pseudo-ternary isothermal phase diagrams, informed by microscopy results were constructed at various temperatures and oxygen partial pressures in order to explain the phases appearing in the experimental thin films, including anatase and bronze TiO_2 and Pt metal and oxides. Most significantly, it has been found that the reversible dissolution and reformation of Pt in this system, especially the capacity of the system to store Pt, is dependent upon the nominal composition of the catalyst/support and the operating temperature of the catalyst.

5.5 References

1 Y. Nishihata, J. Mizuki, T. Akao, H. Tanaka, M. Uenishi, M. Kimura, T. Okamoto, N. Hamada, "Self-Regeneration of a Pd-Perovskite Catalyst for Automotive Emissions Control", *Nature* **418** 164-167 (2002).

2 H. Tanaka, M. Taniguchi, M. Uenishi, N. Kajita, I. Tan, Y. Nishihata, J. Mizuki, K. Narita, M. Kimura, K. Kaneko, "Self-Regenerating Rh- and Pt-Based Perovskite Catalysts for Automotive-Emissions Control", *Angew. Chem. Int. Ed.* **45** 5998-6002 (2006).

3 M.B. Katz, S.Y. Zhang, Y.W. Duan, H.J. Wang, M.H. Fang, K. Zhang, B.H. Li, G.W. Graham, X.Q. Pan, "Reversible Precipitation/Dissolution of Precious-Metal Clusters in Perovskite-Based Catalyst Materials: Bulk Versus Surface Re-Dispersion", *J. Catal.* **293** 145-148 (2012).

4 G. Kresse, J. Hafner, "*Ab Initio* Molecular Dynamics for Open-Shell Transition Metals", *Phys. Rev. B* **48** 13115-13118 (1993).

5 J.P. Perdew, K. Burke, M. Ernzerhof, "Generalized Gradient Approximation Made Simple", *Phys. Rev. Lett.* **77** 3865-3868 (1996).

6 P.E. Blöchl, "Projector Augmented-Wave Method", *Phys. Rev. B* **50** 17953-17979 (1994).

7 S.P. Ong, L. Wang, B.W. Kang, G. Ceder, "Li-Fe-P-O_2 Phase Diagram from First Principles Calculations", *Chem. Mater.* **20** 1798-1807 (2008).

8 L. Wang, T. Maxisch, G. Ceder, "A First-Principles Approach to Studying the Thermal Stability of Oxide Cathode Materials", *Chem. Mater.* **19** [3] 543-552 (2007).

9 L. Wang, T. Maxisch, G. Ceder, "Oxidation Energies of Transition Metal Oxides Within the GGA+U Framework", *Phys. Rev. B* **73** [19] 195107-1-6 (2006).

10 Y.L. Lee, J. Kleis, J. Rossmeisl, D. Morgan, "*Ab Initio* Energetics of La*B*O_3(001) (*B*=Mn, Fe, Co, and Ni) for Solid Oxide Fuel Cell Cathodes", *Phys. Rev. B* **80** [22] 224101-1-20 (2009).

11 D.A. McQuarrie; *Statistical Mechanics*, University Science Books (2000).

12 A. Van de Walle, G. Ceder; Automating First-Principles Phase Diagram Calculations; *J. Phase Equilib.* **23** 348-359 (2002).

13 A. Van der Ven, J.C. Thomas, Q. Xu, J. Bhattacharya, "Linking the Electronic Structure of Solids to Their Thermodynamic and Kinetic Properties", *Math. Comput. Simul.* **80** 1393-1410 (2010).

14 J.M. Sanchez, F. Ducastelle, D. Gratias, "Generalized Cluster Description of Multicomponent Systems", *Physica A* **128** 334-350 (1984).

15 A. Van der Ven, H.C. Yu, G. Ceder, K. Thornton, "Vacancy Mediated Substitutional Diffusion in Binary Crystalline Solids", *Prog. Mater. Sci.* **55** 61-105 (2010).

16 G.L.W. Hart, V. Blum, M.J. Walorski, A. Zunger, "Evolutionary Approach for Determining First-Principles Hamiltonians", *Nature Mater.* **4** 391-394 (2005).

17 Q. Xu, A. Van der Ven, "First-Principles Investigation of Metal-Hydride Phase Stability: The Ti-H System", *Phys. Rev. B* **76** [6] 064207-1-12 (2007).

18 J. Bhattacharya, A. Van der Ven, "Phase Stability and Nondilute Li Diffusion in Spinel $Li_{1+x}Ti_2O_4$", *Phys. Rev. B* **81** [10] 104304-1-12 (2010).

19 S. Andersson, A.D. Wadsley, "$Na_xTi_4O_8$, an Alkali Metal Titanium Dioxide Bronze", *Acta Cryst.* **15** 201-206 (1962).

20 H. Nishizawa, Y. Aoki, "The Crystallization of Anatase and the Conversion to Bronze-Type TiO_2 Under Hydrothermal Conditions", *J. Sol. St. Chem.* **56** 158-165 (1985).

21 H. Savaloni, K. Khojier, M.S. Alaee, "Characteristics of Nanostructure and Electrical Properties of Ti Thin Films as a Function of Substrate Temperature and Film Thickness", *J. Mater. Sci.* **42** 2603-2611 (2007).

22 K.T. Jacob, S. Gupta, "Phase Diagram of the System Ca-Ti-O at 1200 K"; *Bull. Mater. Sci.* **32** 611-616 (2009).

23 K.T. Jacob, T.H. Okabe, T. Uda, Y. Waseda, "Determination of Thermodynamic Properties of Ca_4PtO_6 and $CaPtO_3$ Using Solid State Cells with Buffer Electrodes", Zeitschrift für Metallkunde **90** [7] 491-498 (1999).

24 O. Muller, R. Roy, "Formation and Stability of the Platinum and Rhodium Oxides at High Oxygen Pressures and the Structures Pt_3O_4, β-PtO_2 and RhO_2", *J. Less-Common Metals* **16** 129-146 (1968).

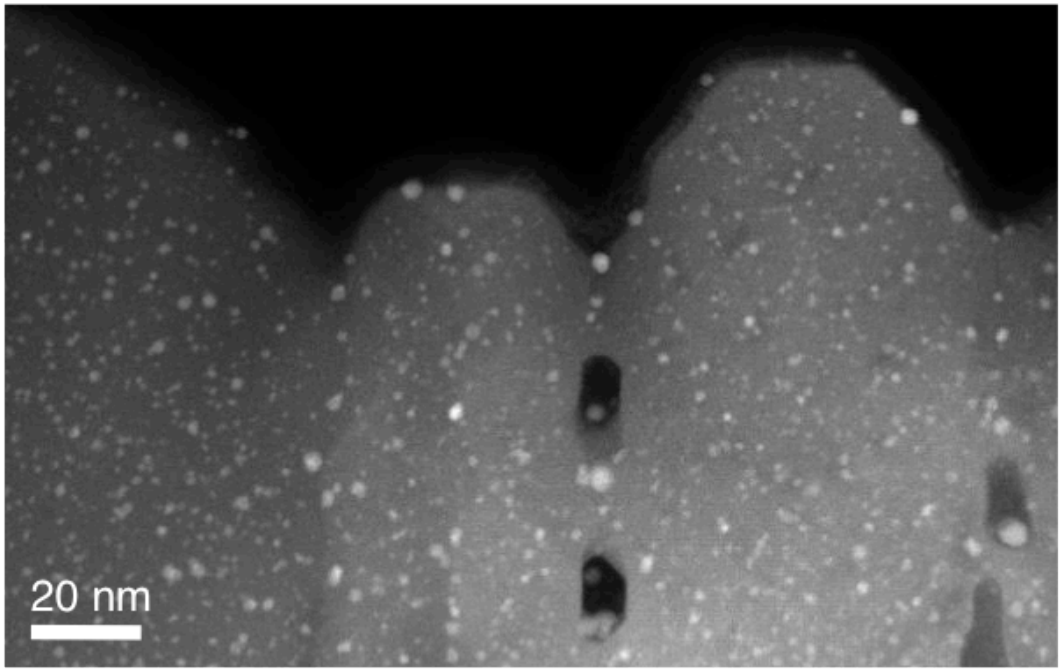

Figure 5.1. HAADF-STEM image of a typical region in the reduced Pt:$CaTiO_3$ thin film showing large-scale formation of Pt particles within the bulk of the oxide.

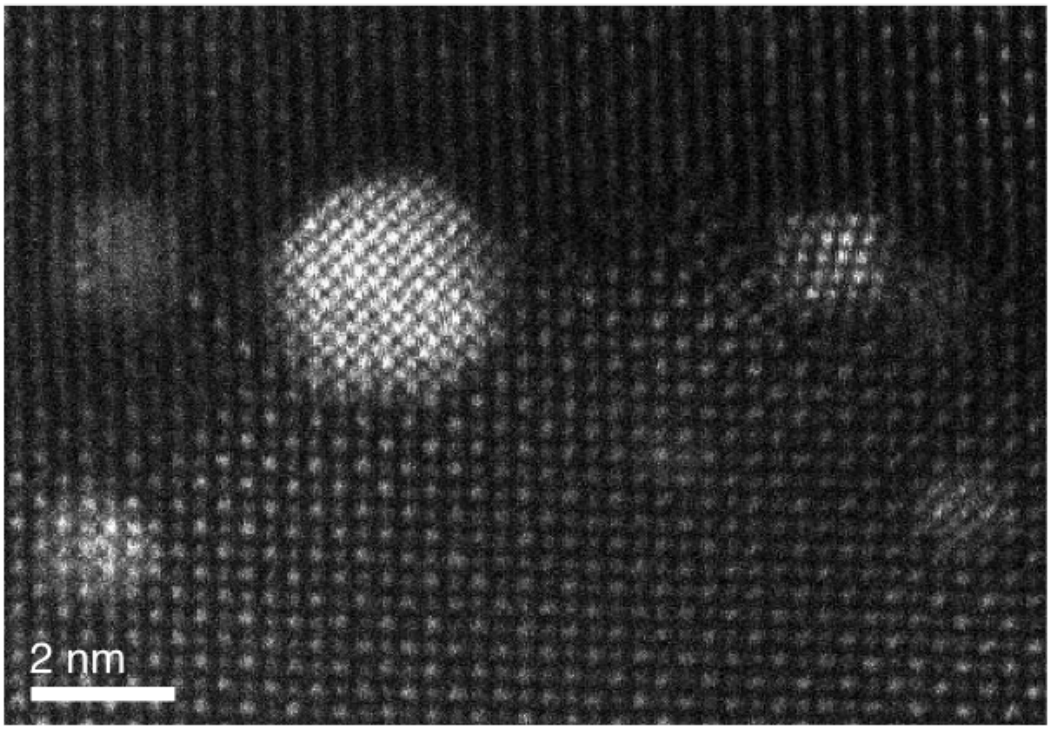

Figure 5.2. HAADF-STEM image of a typical assortment of Pt particles and clusters within the Pt:$CaTiO_3$ thin film subsequent to reduction treatment. Visible are fcc Pt particles of various epitaxial registrations and Pt clusters of a more vague structural nature.

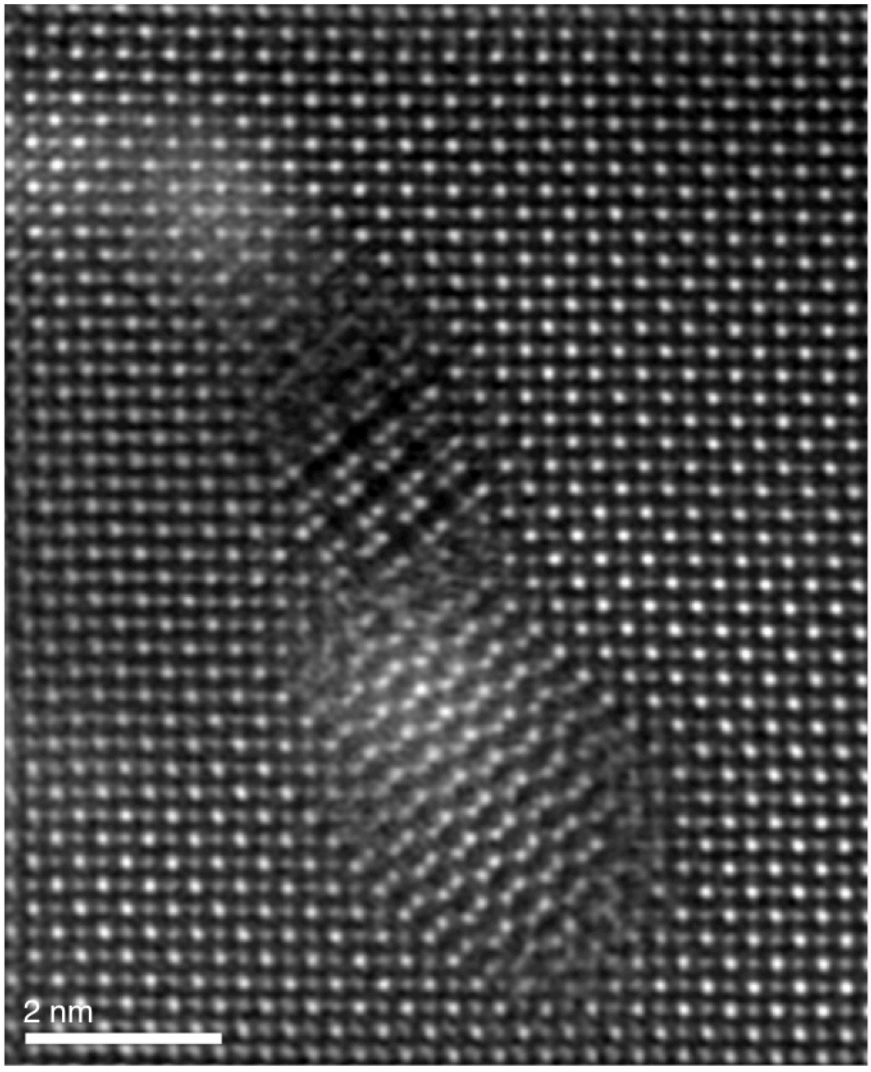

Figure 5.3. HAADF-STEM images of anatase and bronze TiO_2 inclusions within the Pt:$CaTiO_3$ film.

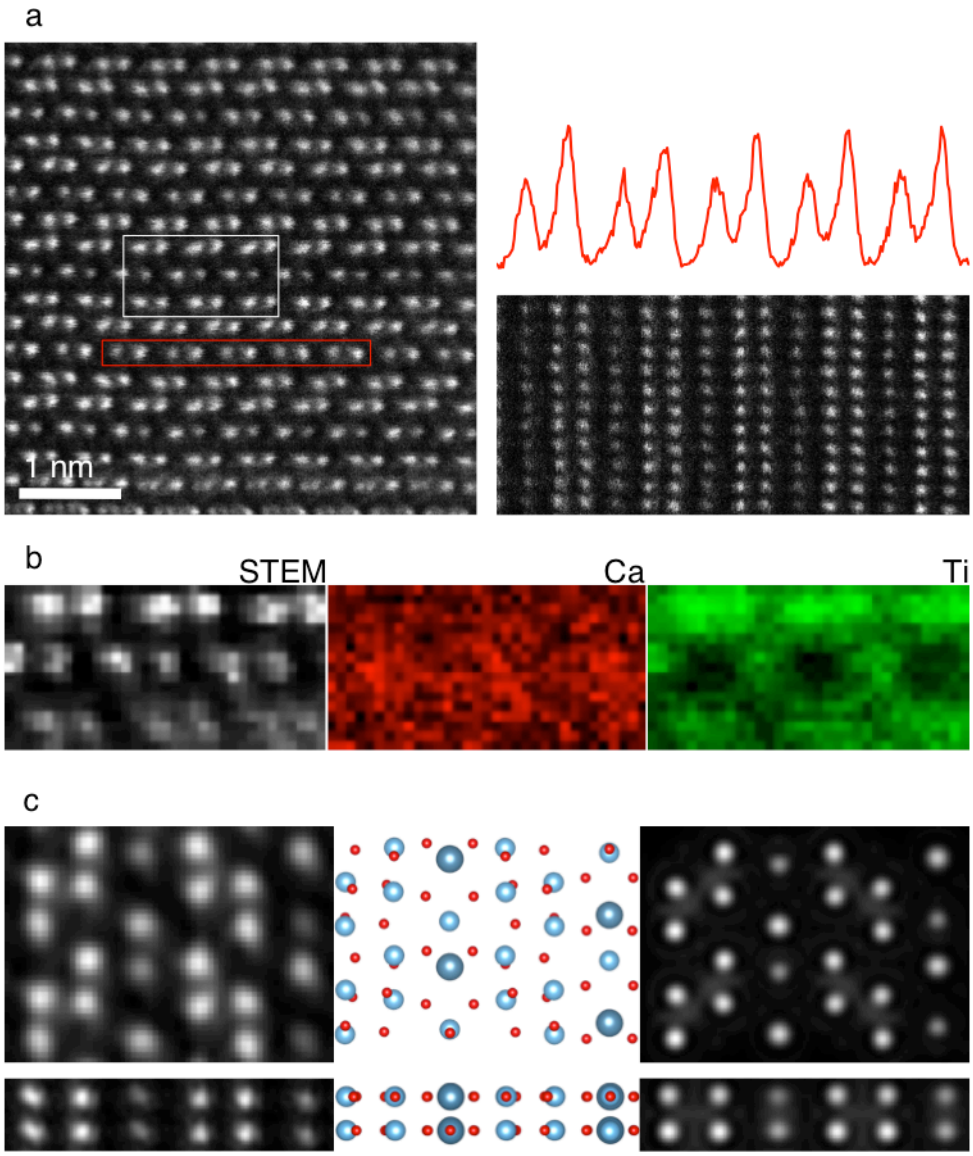

Figure 5.4. (a) HAADF-STEM images of the TiO_2 (B)-related structure along two of its primary crystal axes, and a HAADF intensity trace from the region in the red box showing the alternating intensities of the atomic columns in the intercalated layer. (b) Ca and Ti EELS maps from the white box in (a) showing the identity of the dimmer column as Ca. (c) Images of the phase in question (left), constructed crystal model of the proposed $CaTi_5O_{11}$ structure (center), and simulated HAADF-STEM image of that crystal structure (right).

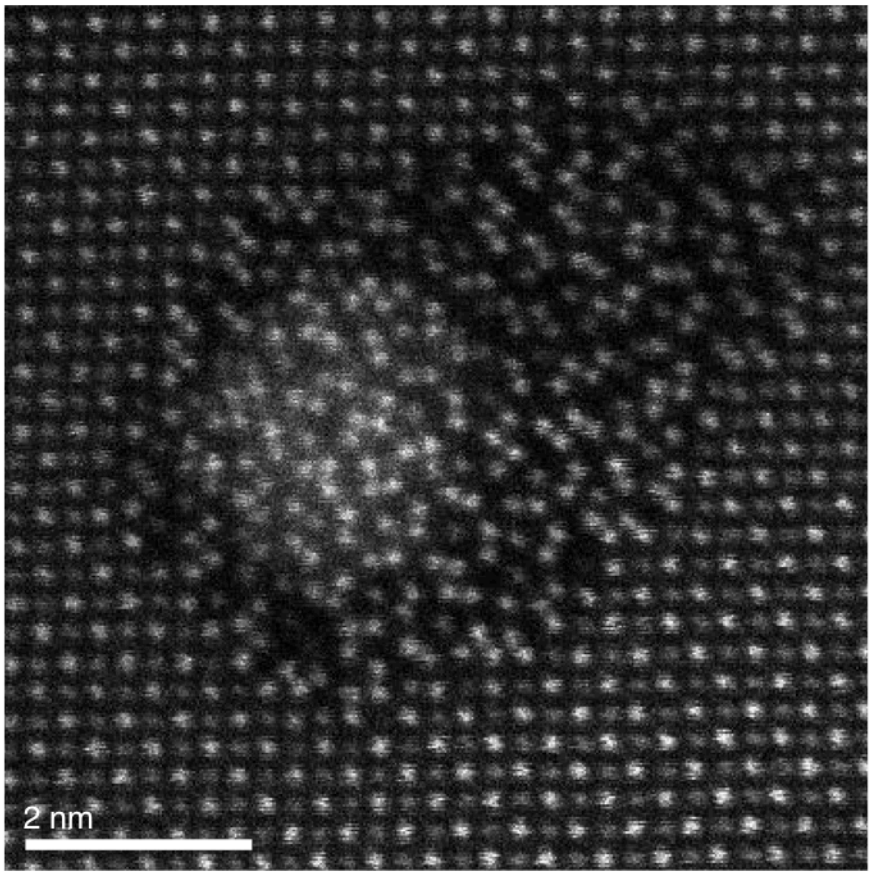

Figure 5.5. HAADF-STEM image of a pseudo-amorphous region of significantly degraded crystallinity.

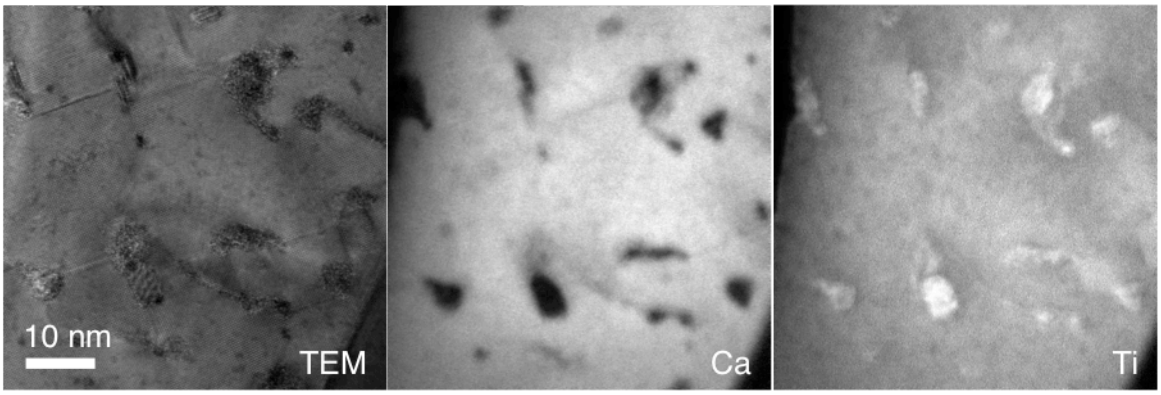

Figure 5.6. TEM image of a typical region in the reduced Pt:$CaTiO_3$ film along with EFTEM images isolating the Ca and Ti signals. No local regions of increased Ca content could be located.

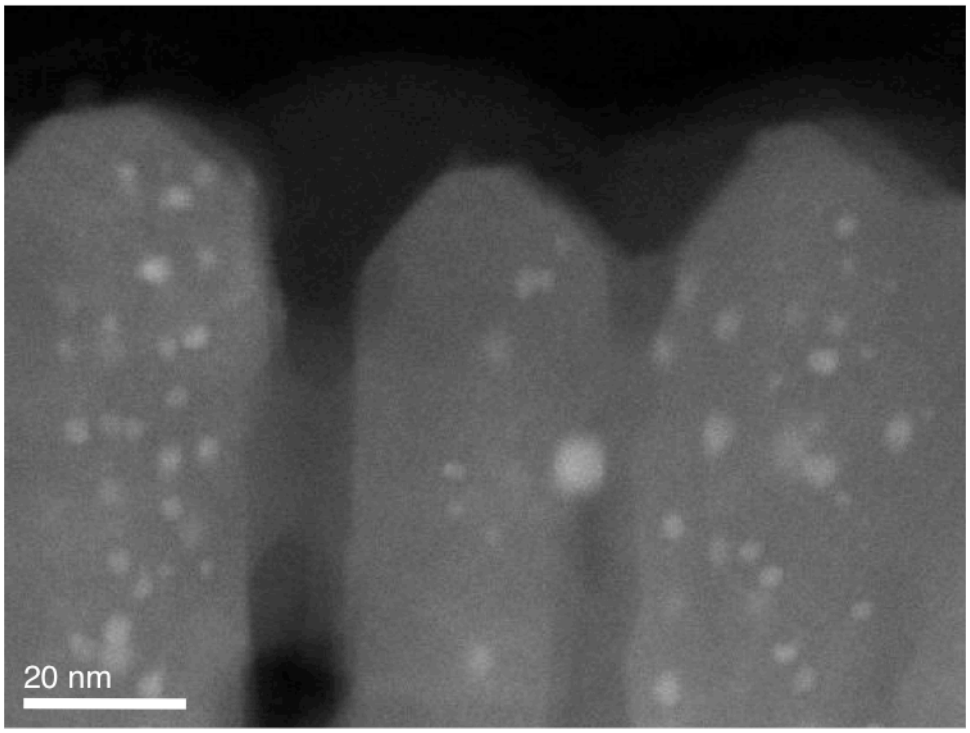

Figure 5.7. HAADF-STEM image of the re-oxidized Pt:$CaTiO_3$ film showing a much lower concentration of small internal Pt particles and clusters, presumably having dissolved back into the oxide matrix. Larger internal particles, however, remain.

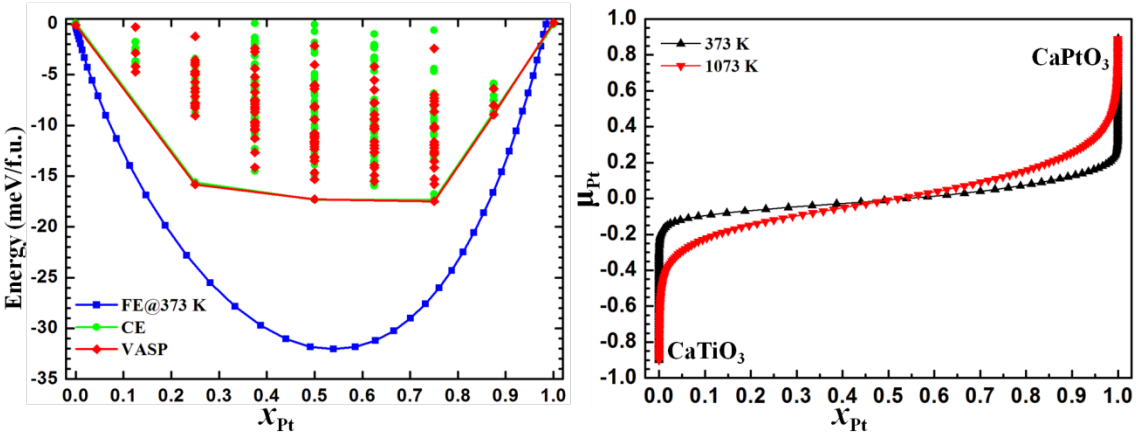

Figure 5.8. (Left) the comparison of the first-principles (VASP) calculated, cluster expansion (CE) predicted formation energies with the free energy (FE) at 373 K derived from Monte Carlo simulation of Pt doped $CaTiO_3$ ($CaTi_{1-x}Pt_xO_3$) system. (Right) the curves of Pt chemical potential as a function of Pt concentration in $CaTi_{1-x}Pt_xO_3$ system at 373 K and 1073 K, calculated by grand canonical Monte Carlo simulations.

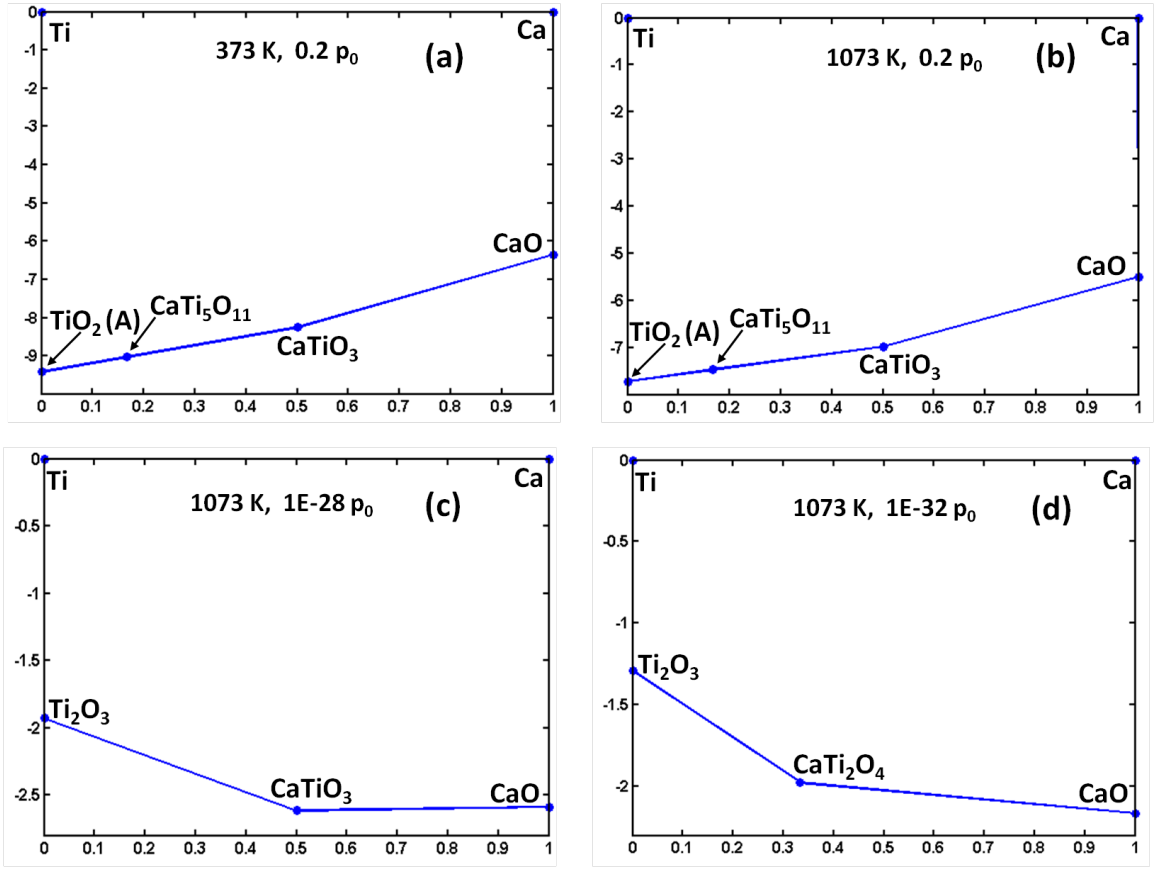

Figure 5.9. First-principles calculated CaO_x-TiO_y pseudo-binary phase diagrams under various temperatures and oxygen pressures. The oxygen partial pressure in (a) and (b) is fixed at 0.2 p_0, the temperature in (c) and (d) is fixed at 1073 K.

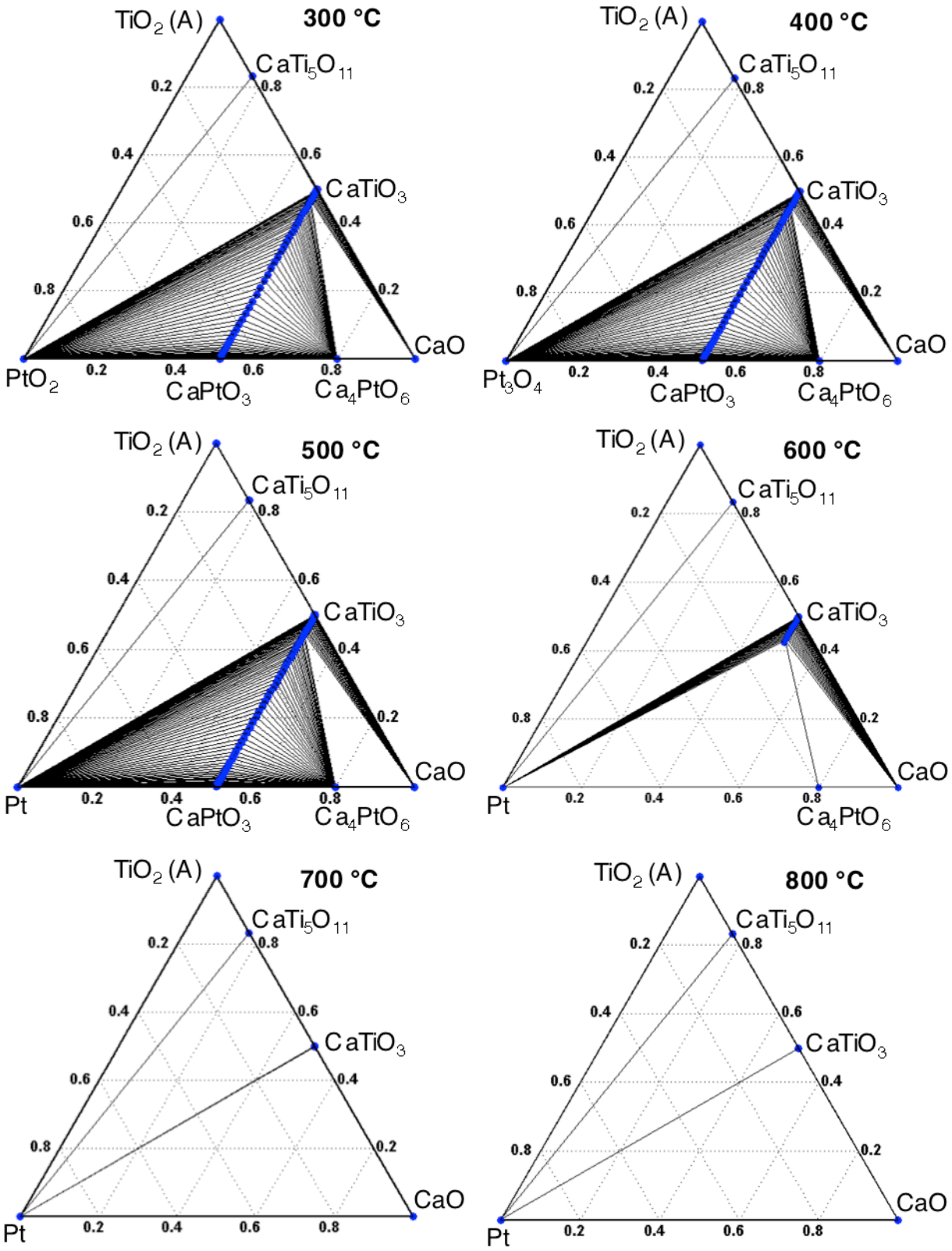

Figure 5.10. Calculated CaO_x-TiO_y-PtO_z pseudo-ternary phase diagrams at various temperatures under reducing conditions, with the oxygen pressure held to 1×10^{-8} atm.

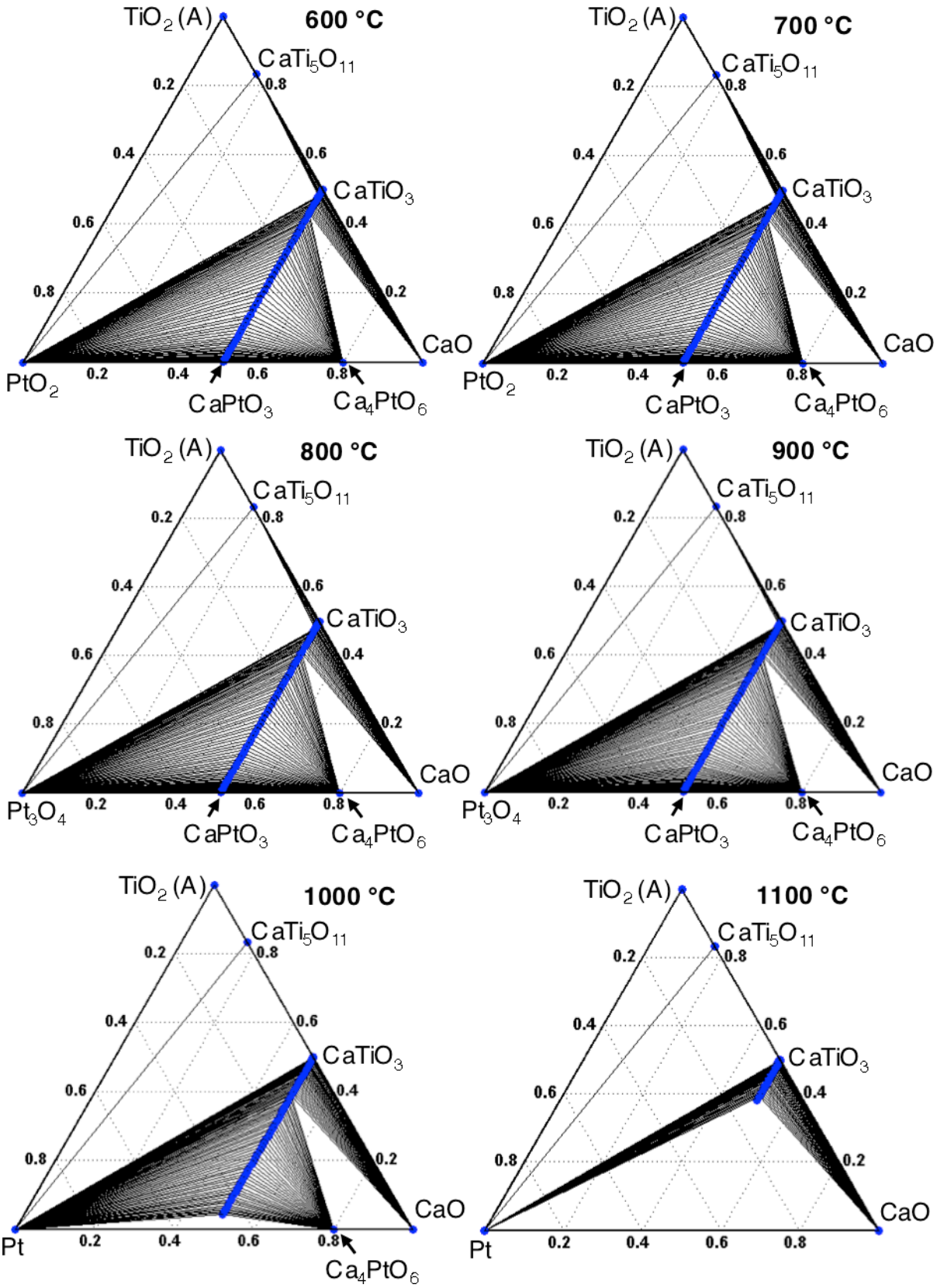

Figure 5.11. Calculated CaO_x-TiO_y-PtO_z pseudo-ternary phase diagrams at various temperatures under oxidizing conditions, with the oxygen pressure held to 0.2 atm.

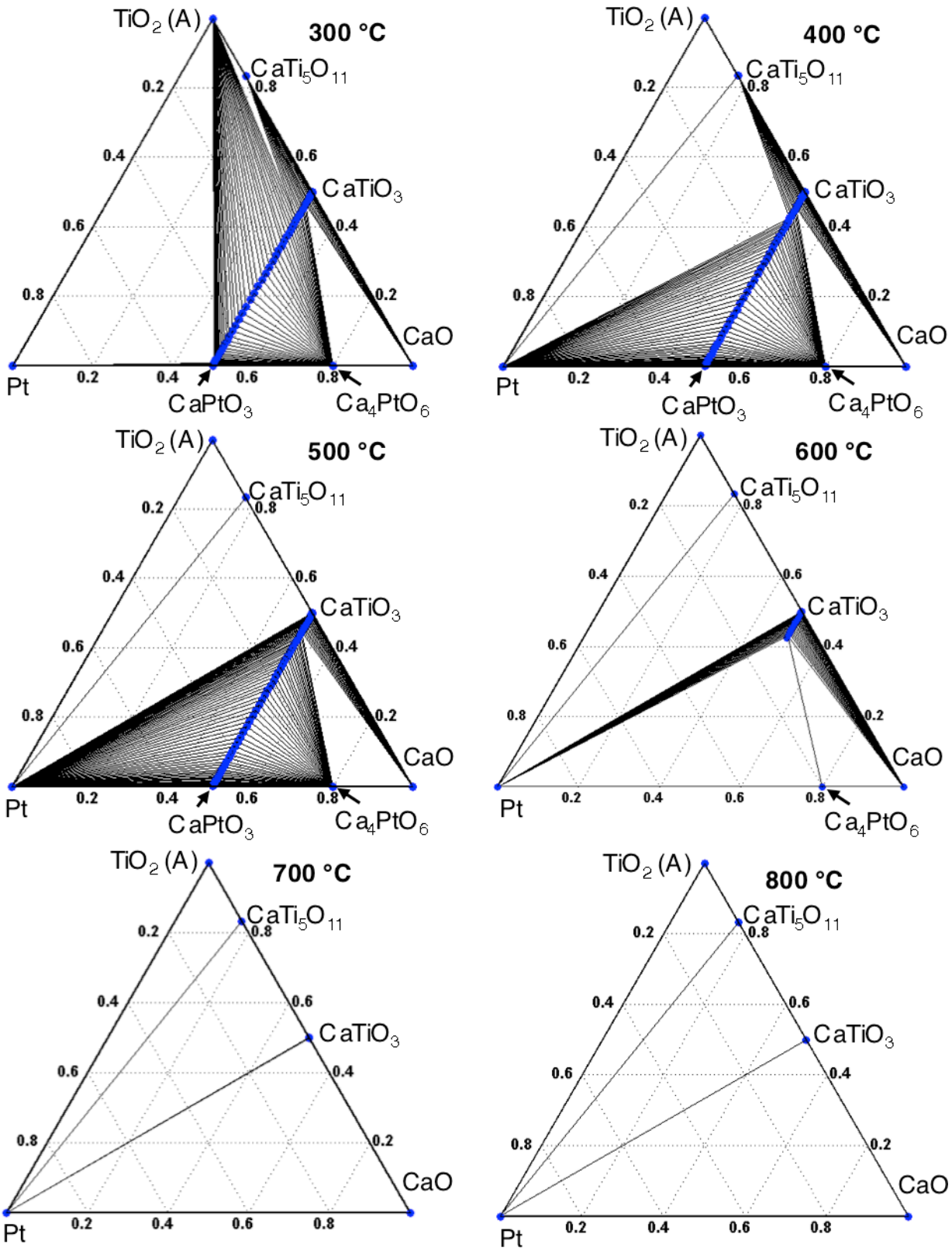

Figure 5.12. Calculated CaO_x-TiO_y-Pt pseudo-ternary phase diagrams, discounting the formation of oxides of Pt, at various temperatures under reducing conditions, with the oxygen pressure held to 1×10^{-8} atm.

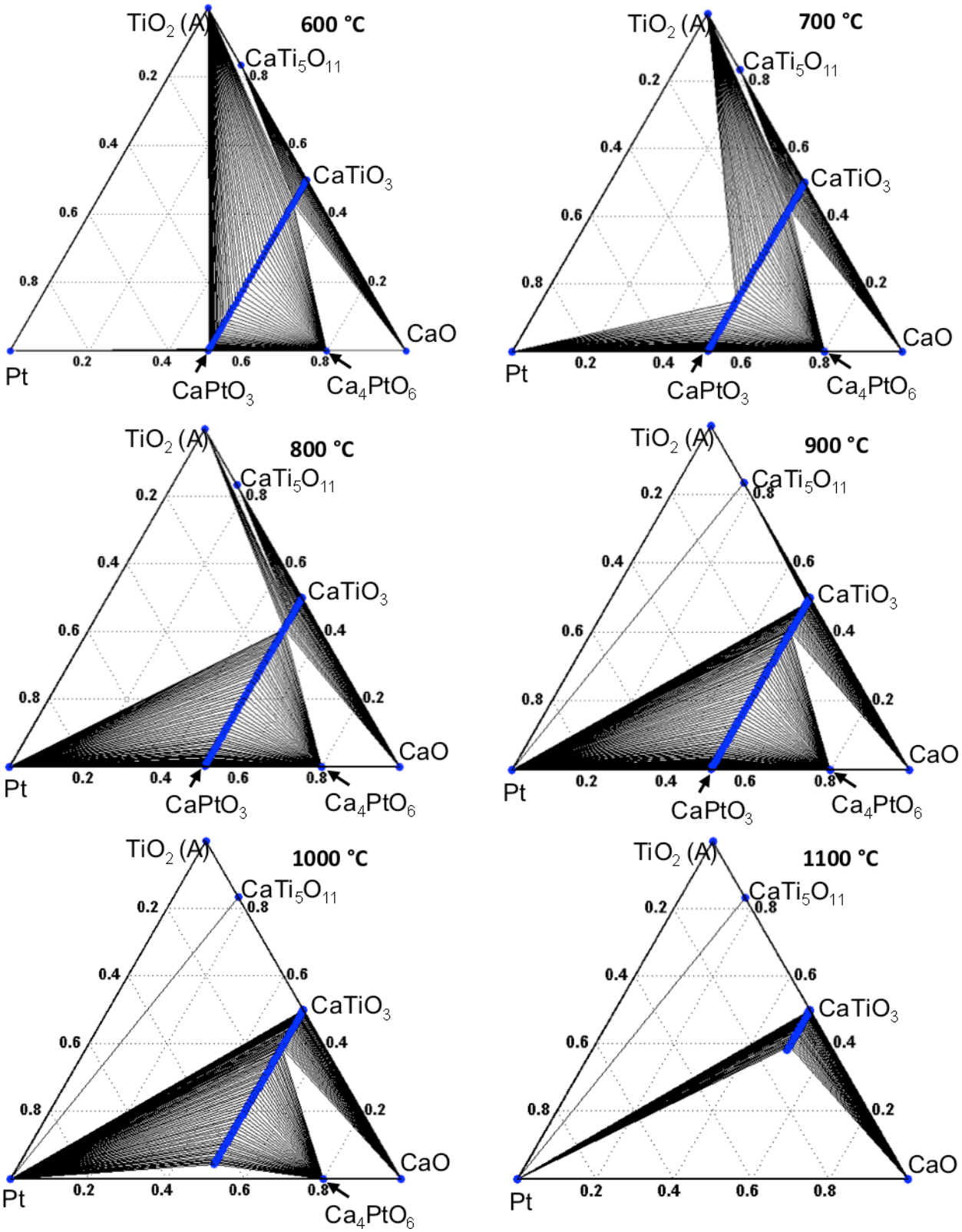

Figure 5.13. Calculated CaO_x-TiO_y-Pt pseudo-ternary phase diagrams, discounting the formation of oxides of Pt, at various temperatures under oxidizing conditions, with the oxygen pressure held to 0.2 atm.

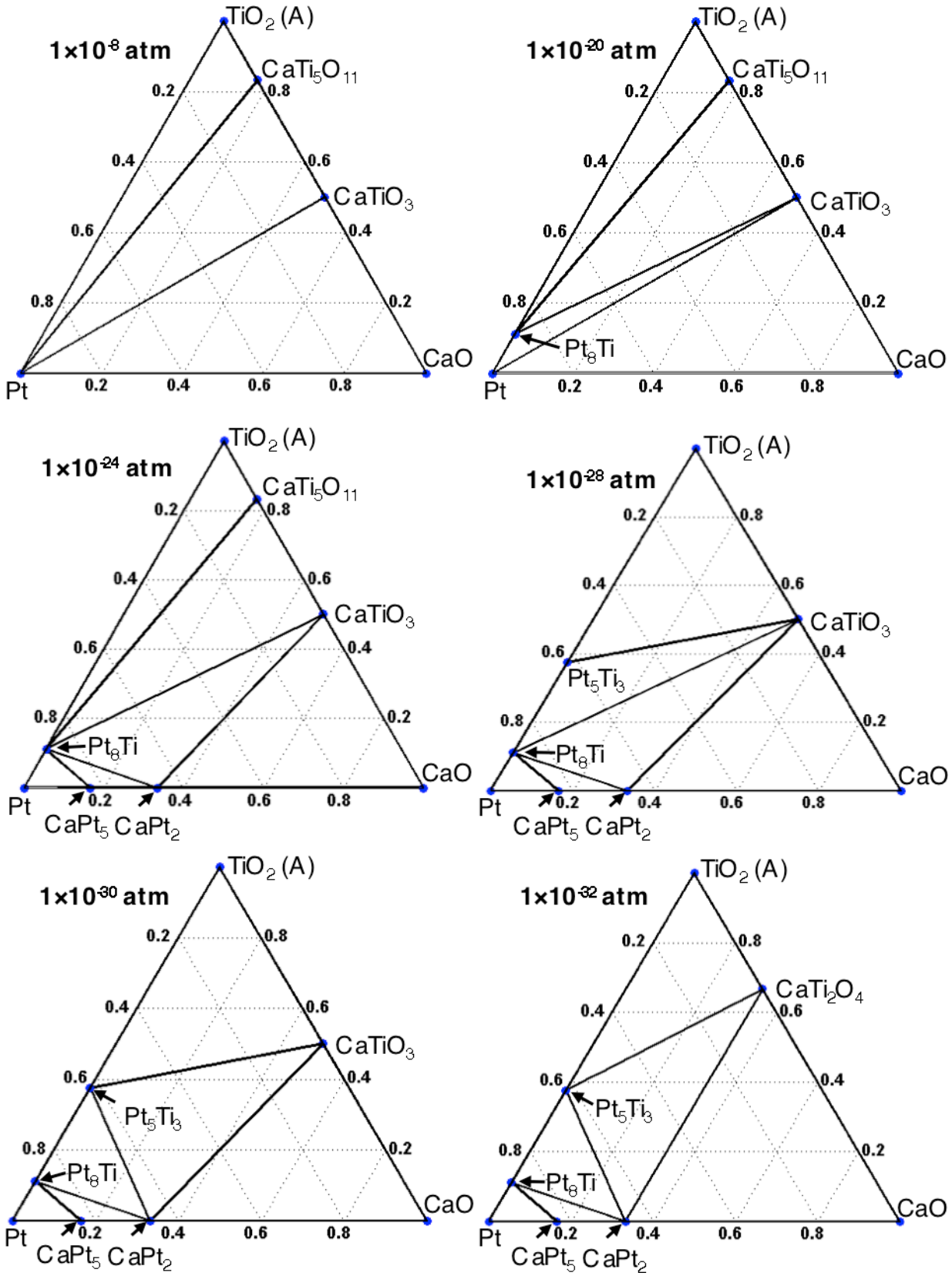

Figure 5.14. Calculated CaO_x-TiO_y-Pt pseudo-ternary phase diagrams calculated for various extremely reducing conditions for 800 °C.

Table 5.1. List of all phases considered in this study, along with their total energies. Those that actually appear in the phase diagrams are bolded and in red.

Phase	E_{tot} (eV)	Phase	E_{tot} (eV)
O_2	-9.077	**Pt_5Ti_3**	-60.938
Ca bulk	-1.909	$Ca_{0.9375}Pt_{0.0625}TiO_3$ (Pbnm)	-40.146
Ti bulk	-7.742	$Ca_{0.75}Pt_{0.25}TiO_3$ (Pbnm)	-39.349
Pt bulk	-6.049	$Ca_{0.9375}Pt_{0.0625}TiO_{2.9375}$ (Pbnm)	-39.625
CaO	-12.995	$CaTi_{0.9375}Pt_{0.0625}O_{2.9375}$ (Pbnm)	-39.317
TiO	-17.375	**$CaTi_{0.9375}Pt_{0.0625}O_3$ (Pbnm)**	-39.775
Ti_2O_3	-44.828	**$CaTi_{0.75}Pt_{0.25}O_3$ (Pbnm)**	-37.992
Ti_3O_5	-71.408	$CaTi_{0.75}Pt_{0.25}O_{2.75}$ (Pbnm)	-36.145
TiO_2 (A)	-26.632	**$CaTi_{0.875}Pt_{0.125}O_3$ (Pbnm)**	-39.180
TiO_2 (B')	-26.580	**$CaTi_{0.25}Pt_{0.75}O_3$ (Pbnm)**	-33.203
TiO_2 (R)	-26.542	**$CaTi_{0.5}Pt_{0.5}O_3$ (Pbnm)**	-35.598
TiO_2 (B)	-26.618	**$CaTi_{0.375}Pt_{0.625}O_3$ (Pbnm)**	-34.397
$CaTi_2O_4$	-58.155	**$CaTi_{0.125}Pt_{0.875}O_3$ (Pbnm)**	-31.996
$Ca_3Ti_2O_7$	-93.690	**$CaPtO_3$ (Pbnm)**	-30.794
$Ca_4Ti_3O_{10}$	-134.062	$CaTi_{1.875}Pt_{0.125}O_{3.875}$	-56.291
$CaTiO_3$ (Pm-3m)	-40.012	$Ca_{0.75}Pt_{0.25}Ti_2O_4$	-57.703
$CaTiO_3$ (Cmmm)	-40.012	$Ca_{0.75}Pt_{0.25}Ti_2O_{3.75}$	-56.813
$CaTiO_3$ (Pbnm)	-40.368	$Ti_{1.917}Pt_{0.083}O_3$	-44.240
$CaTi_5O_{11}$	-146.904	$Ti_{1.917}Pt_{0.083}O_{2.917}$	-43.630
$CaPt_5O_{11}$	-98.349	$Ti_{0.875}Pt_{0.125}O_2$ (B)	-25.353
$CaTi_4PtO_{11}$	-136.971	$Ti_{0.96875}Pt_{0.03125}O_2$ (B)	-26.302
$PtTi_5O_{11}$	-141.939	$Ti_{0.9375}Pt_{0.0625}O_2$ (B)	-25.988
$TiO_{1.5}$(R)	-21.653	$Ti_{0.9375}Pt_{0.0625}O_{1.9375}$ (B)	-25.561
$TiO_{1.9375}$ (R)	-25.946	$Ti_{0.9375}Pt_{0.0625}O_2$ (A)	-25.975
$TiO_{1.875}$ (B)	-25.062	$Ti_{0.9375}Pt_{0.0625}O_{1.9375}$ (A)	-25.554
$Ca_{0.9375}TiO_3$ (Pbnm)	-39.669	$Ti_{0.96875}Pt_{0.03125}O_2$ (A)	-26.294
$CaTi_{0.9375}O_3$ (Pbnm)	-38.958	$Pt_{0.03125}$+TiO_2 (B)	-26.707
$CaTiO_{2.9375}$ (Pbnm)-Ov_{II}	-39.7540	$Pt_{0.125}$+TiO_2 (B)	-26.990
$CaTiO_{2.9375}$ (Pbnm)-Ov_I	-39.734	$Pt_{0.25}$+TiO_2 (B)	-27.431
$CaTiO_{2.96875}$ (Pbnm)-Ov_{II}	-40.069	$Pt_{0.5}$+TiO_2 (B)	-28.270
$CaTiO_{2.96875}$ (Pbnm)-Ov_I	-40.067	$Ca_{0.25}$+TiO_2 (B)	-27.946
$Ca_{0.75}TiO_3$ (Pbnm)	-37.592	$Ca_{0.5}$+TiO_2 (B)	-28.630
$CaTi_{0.75}O_3$ (Pbnm)	-34.828	$Ca_{0.25}Pt_{0.25}$+TiO_2 (B)	-29.763
$Ca_{0.9375}TiO_{2.9375}$ (Pbnm)-Ov_{II}	-39.397	$Pt_{0.25}$+TiO_2 (A)	-27.152
$Ca_{0.9375}TiO_{2.9375}$ (Pbnm)-Ov_I	-39.385	$Pt_{0.5}$+TiO_2 (A)	-28.481
$CaTi_{0.9375}O_{2.875}$ (Pbnm)-$Ov_{I,II}$	-38.474	$Pt_{0.75}$+TiO_2 (A)	-29.278
$Ca_{0.9375}Ti_{1.0625}O_3$ (Pbnm)	-40.589	Pt_1+TiO_2 (A)	-30.289
$Ca_{1.0625}Ti_{0.9375}O_3$ (Pbnm)	-39.622	**PtO_2 (Pnnm)**	-17.373
PtTi	-15.340	PtO_2 (P-3m1)	-17.310
$PtTi_3$	-31.921	PtO_2 (Pn-3mS)	-14.843
Pt_8Ti	-59.946	PtO_2 (B)	-16.485
$CaPt_2$	-17.196	PtO_2 (R)	-17.264
$CaPt_5$	-35.378	**Pt_3O_4 (Pm-3n)**	-41.069
$Ca_3Ti_{1.75}Pt_{0.25}O_7$	-91.320	Pt_3O_4 (Im-3m)	-33.758
$Ca_4Ti_{2.75}Pt_{0.25}O_{10}$	-131.692	PtO (P42-mmc)	-11.524
$CaTi_{1.875}Pt_{0.125}O_4$	-57.220	PtO (Fm-3m)	-9.900

Chapter VI

In Situ Studies of Self-Regenerative Catalyst Evolution

6.1 Introduction and Background

With all of its advantages with regard to probing matter at an unprecedentedly small scale, the transmission electron microscope (TEM) can have some frustrating shortcomings. Because of the necessity for the specimen to be essentially electron-transparent, one is limited to studying extremely thin and/or extremely small specimens as well as extremely limited portions of larger samples. This can lead to a situation where the portion of the specimen studied is not necessarily representative of the sample as a whole. The other major shortcoming of the TEM is that specimens must be examined in ultra-high vacuum. For materials whose behavior is dependent on maintaining a controlled oxidizing or reducing environment, namely the self-regenerative catalyst discussed in this dissertation, this constraint can be quite limiting.

Recent technological developments in *in situ* equipment and techniques for use within the TEM column have therefore been met with much fanfare and anticipation. The major circumstance complicating efforts to place *in situ* equipment in the column is the gap in the objective lens pole pieces. In order to achieve very high resolutions, pole piece gaps are generally kept as small as possible – 2.1 mm in the case of the JEOL JEM-2100F used for the majority of work in this dissertation, for example. Heating stages are, in a sense, relatively easy to use and inexpensive to procure. They have the added benefit of being generally compact, as most are resistively heated.

Most heating stages have the downside that the entire tip is heated, resulting in a relatively large thermal mass and requiring extended ramping times.

Introducing gas atmospheres to the specimen within the column, however, is more difficult. The earliest TEMs to allow for such gas exposure were heavily modified instruments, referred to generally as environments TEMs (ETEMs).[1-4] In these instruments, the specimen was exposed to reaction gas via bleed lines into the specimen chamber. It was then heated, as necessary, using conventional heating stages. These instruments were outfitted with differential pumping systems in order to keep the gas from making its way up the column to the gun chamber. Variations on these designs make up a predominant portion of the market, and are still manufactured and sold by the major equipment manufacturers today. This type of design, however, presents two major problems. The first is that the electron beam must travel through several millimeters of gas, which scatters the electron beam and degrades both the signal and the ultimate resolution of the instrument. The second major shortcoming is that the differential pumping systems are of limited effectiveness, and pressures in the specimen chamber are thus limited to a few tens of Torr (~0.01-0.04 atm) of total gas pressure. This limits its effect of creating realistic operating conditions for most catalysts. Furthermore, ETEM instruments are generally quite expensive and come with necessary compromises with regard to other capabilities.

Given the experimental limitations of ETEM instruments, there has been a recent push for completely "on-holder" solutions to the *in situ* heating and gas exposure that would allow a modular holder device to be placed into the column of a conventional TEM. After a concept first described and demonstrated by Creemer *et al.* in 2009,[5] the equipment used in this report is designed and produced by Protochips Inc. (Raleigh, NC). The design, in essence, uses a

microfabricated, resistively heated, silicon-based chip with a Si_3N_4 electron-transparent support window for the powder specimen, based on Protochips' Aduro™ heating system.[6] The heater chip is placed against a window chip of similar construction, equipped with gold spacer pads, and the pair is clamped into place at the end of a TEM specimen rod. The spacers create a gap of about 5 μm between the two Si_3N_4 windows, allowing for gas to be held in the holder tip with the powder specimen, which was placed on the heater chip prior to clamping. The rod itself is fitted with the necessary feedthroughs to allow for electrical resistive heating and a gas inlet and outlet, to allow for flow, if desired, with total pressures up to ambient (1 atm). This device will collectively be referred to as the 'gas cell'.[7] A schematic and photographs of the gas cell are shown in Figure 6.1.

6.2 Experimental Methods

$CaTi_{0.95}Pt_{0.05}O_3$ and $BaCe_{0.95}Pt_{0.05}O_3$ (Pt:$CaTiO_3$ and Pt:$BaCeO_3$, respectively) powders were prepared via the citrate method,[8] and are meant to replicate the material synthesized by Tanaka *et al.*[9] Stoichiometric amounts of $Ca(NO_3)_2 \bullet 4H_2O$ and $Ti[O(CH_2)_3CH_3]_4$ for Pt:$CaTiO_3$ or $Ce(NO_3)_3 \bullet 6H_2O$ and $Ba(NO_3)_2$ for Pt:$BaCeO_3$ were mixed with $PtC_{10}H_{14}O_4$ (Alfa Aesar) and dissolved in de-ionized water with citric acid, with nitric acid was used to control the solution pH. The solution was dehydrated at 100 °C and held at 60 °C until it formed a gel, which was then calcined at 800 °C in flowing oxygen. The calcination treatment in oxygen essentially ensures that the materials as-prepared are in their oxidized state, with the catalyst metal maximally in solution within the perovskite. $CaTi_{0.95}Rh_{0.05}O_3$ (Rh:$CaTiO_3$) powders were obtained from Cabot Corporation.

All experiments discussed in this chapter were performed at the Advanced Microscopy Laboratory at Oak Ridge National Laboratory (ORNL) and, unless otherwise noted, used the 'gen 3' iteration of the prototype gas cell holder produced by Protochips Inc. Powders were suspended in either ethanol or hexane and sonicated to avoid agglomeration before being dropped onto the heater chip. The gas cell was then assembled and placed in the aberration-corrected JEOL JEM-2200FS scanning TEM (STEM) at ORNL. A diagram of the gas manifold system is shown in Figure 6.2, and an extended discussion of its details can be found in Reference 7. Throughout the experiments discussed in this section, the gas cell was maintained at an elevated temperature of 250 °C to avoid carbon contamination build-up and eliminate the need for extended beam showers. This slightly elevated temperature did not appear to have any effect on the sample. Because of the extremely small thermal mass of the heated region of the heater chips, there is essentially no ramp time, and the device reaches the desired temperature within milliseconds of the current being applied.

6.3 Results and Discussion

6.3.1 Redox Treatment of Self-Regenerative Catalyst Powders

The first experiments in this series were performed on the Aduro heater platform without reaction gas, as the gas cell holder was not yet available. Reductions were therefore performed in the vacuum of the column and oxidations were performed by pulling the specimen rod into the sample entry chamber and flooding it with lab air.

The results of the initial reduction are shown in Figure 6.3. The specimen was first heated to 600 °C for 5 min, followed by an additional 5 min at 800 °C, both in the column vacuum. The initial material, shown in Figure 6.3a, does have some extant Pt particles, plainly visible because

of the z-contrast nature of the high-angle annular dark-field (HAADF) STEM imaging mode used for all experiments discussed in this section. These are not the result of spontaneous reduction within the vacuum, but are remnants of the Pt used during synthesis that had not been fully incorporated into the perovskite matrix. Quite surprising was the rate at which Pt precipitated out of the perovskite matrix, even at the relatively low reduction temperature of 600 °C (Figure 6.3b). Because images were acquired before and after the reduction treatment, it is easy to see which Pt particles are directly the result of said reduction. The majority of Pt that formed during reduction, and, in fact, the entire population of them within the field of these images, are very small – approximately 1-2 nm. They are likewise presumably internal, having formed within the bulk of support oxide itself. The relatively low temperature of 600 °C and the short time spent at that temperature assure that the Pt atoms/ions were limited to extremely small diffusion lengths. Additional heating for 5 min at 800 °C, shown in Figure 6.3c, induces the precipitation of many more small Pt particles. Interesting to note is the relative monodispersity of this precipitated Pt. Given the short time in which Pt can diffuse, it is reasonable to assume that the Pt diffuses a short distance to meet other Pt atoms in its immediate vicinity to form a small cluster of a few tens of atoms or less and essentially freezes there. The perovskite precludes these internal particles from coarsening via any sort of migration and coalescence mechanism.

It was then attempted to drive the Pt from a reduced specimen back into solution within the perovskite by oxidizing it, this time in lab air. Because it is unknown if reduction in vacuum mimics the results of reducing in simulated engine exhaust, a portion of the Pt:$CaTiO_3$ was reduced under flowing 10% H_2 (bal. N_2) for 1 hr (the same conditions used in References 8 and 10) in prior to placing it on the holder. It was then heated in lab air and examined

intermittently. Figure 6.4 contains two frames, taken after 10 minutes and 100 minutes of oxidation (Figure 6.4a and 6.4b, respectively). (Images from before oxidation were not usable as all regions examined at that point were in areas where the underlying support film destroyed itself upon initial heating.) There is very little difference in the frequency of Pt particles between the two panels, indicating that the dissolution reaction is much more difficult, again corroborating the work on the thin films. Attempts to reduce the specimen and induce additional Pt to precipitate from the oxide were again impeded by the instability of the underlying support film, shown in Figure 6.4c.

Experiments were subsequently repeated in the gas cell when it became available. Because of tendencies for the heater membranes to rupture when heated, pressure was kept to 50 Torr total pressure, with reductions performed in 4% H_2 (bal. Ar) and oxidations in pure O_2. A diagram of the treatment is shown in Figure 6.5, along with images of a selected Pt:$CaTiO_3$ aggregate from each segment in the heat treatment. Since reduction is extremely rapid, the specimen was only reduced for 10 min before being subjected to oxidizing gas at various temperatures. These various temperatures were used to test whether 800 °C was high enough to prevent Pt from re-oxidizing, and causing any extant oxide to further decompose into metal. The extended re-oxidation regimen was only successful in driving some Pt back into the perovskite, as can be seen in Figure 6.6. An additional region is shown in Figures 6.7 and 6.8. Of special note is the fact that a ~5 μm gas path has little effect on either the resolution or apparent noise level in the images.

The experiments were then attempted again with a new, more reliable set of heater chips of a slightly altered design. These chips, coupled with improved procedures for clamping and sealing

the gas cell, allowed for the device to be more reliably operated at high gas pressures. Pt:$CaTiO_3$ was again loaded into the cell for redox treatments. It was imaged in its as-prepared state, as well as after reductions at 600 °C and 700 °C, each for 10 min in 300 Torr H_2 (bal. Ar) and after oxidation treatments at 700 °C for 30 min in 300 Torr O_2, 800 °C for 30 min in 300 Torr O_2, and 800 °C for 60 min in 600 Torr O_2. STEM images from two typical regions of this specimen are shown in Figures 6.9a,b. They show Pt particle precipitation upon reduction, but minimal, if any, Pt dissolution upon oxidation. Interesting to note is the surface Pt particle coarsening in Figure 6.9b. The material appeared to have some degree of inhomogeneity, as is evident in the lack of any Pt precipitation at all in the particle in Figure 6.9c. It is apparent that the Pt distribution was inhomogeneous to the degree that some entire aggregates exhibited no visible Pt precipitation. Since the Pt readily precipitates from this material, even under mild reducing conditions, it is a reasonable assumption that no Pt was present in the material shown in Figure 6.9c.

Also examined were two other proposed self-regenerative catalysts: Rh:$CaTiO_3$ and Pt:$BaCeO_3$. Rh:$CaTiO_3$ behaved largely similarly to Pt:$CaTiO_3$, as was the case with the thin films of the same materials in previous sections. Pt:$BaCeO_3$ showed generally the same behavior, as well. The Pt:$BaCeO_3$ specimen was reduced at 800 °C for 5 min in 300 Torr H_2 (bal. Ar), and subsequently oxidized at 800 °C for 60 min in 300 Torr O_2, interrupting the treatment after 10 min by bringing the temperature to 250 °C to examine the specimen before increasing it back to 800 °C to finish the oxidation. Images of a typical region are shown in Figure 6.10. The most evident aspect of the Pt:$BaCeO_3$ sample is that what appeared to be the primary particles in the as-prepared stage seem to have fractured and broken apart after the initial reduction, subsequently comprising many smaller apparently primary particles. The exact mechanism

behind this particular reaction is as yet undetermined, and merits some further study. It could be that the extrusion of Pt particles from the oxide occurred rapidly enough to cleave the primary particles apart. The behavior of those Pt particles was, in contrast, more conventional. The short reduction treatment predictably induced their precipitation from the oxide host. Oxidation treatment appeared to drive some of the Pt back from the particles into the perovskite, as is visible in Figure 6.10b, though most of the Pt remained in a metallic state.

6.3.2 Gas Cell Holder Practicalities and Complications

The various complications encountered throughout the use of the gas cell thus far merit a discussion. In order to minimize the gas flow path, the nominal gap between the heater chip and the window membrane is approximately 5 μm. This is effectively limits the size of the specimen that can be placed in the cell. Many powder aggregates, however, can be much larger than that. For this reason, the sample must be sonicated and care must be taken to make sure it is very well dispersed in suspension. This has the practical result that the powder suspension has a very low density, and it then becomes difficult to get an adequate amount of the specimen onto the electron-transparent portions of the heater chip, which must be checked and rechecked after each deposition, but before sealing into the gas cell. The electron-transparent regions are those in which the resistive ceramic is perforated, leaving only Si_3N_4 to span the resultant hole. Figure 6.11a shows a scanning electron microscope (SEM) image of a typical heater chip. It is for this same reason that specimens are limited to powders or lift-out lamellae from focused ion beam sample preparation. In the latter case, the lamella must be extremely carefully placed on the heater chip so as not to place undue stress on the window chip.

The major concern regarding the gas cells, however, is rupturing. When a rupture occurs, the gas from the manifold flows into the column and is usually high enough to cause a fail-safe sealing of the gun valve, in order to avoid damage to the gun filament. Several different events can lead to a heater chip rupture. The first is built-in defects from the initial manufacture. Debris from the fabrication process, as well as simple inhomogeneities in the Si_3N_4 membrane, can lead to a membrane rupture upon thermal cycling. The problems are exacerbated when heated, as the membrane expands and flexes due to thermal expansion and causes tears to propagate. Figure 6.11b shows one such rupture, in this case induced by debris during manufacturing. The hole is small, only about 1 μm in diameter, but is nonetheless sufficiently large to allow enough gas out of the holder to cause the gun valve to close, and bringing the experiment to an premature end.

Larger scale ruptures can also occur in some circumstances. The utmost care must be taken when changing the external pressure on the gas cell, for instance when removing from the column into the exchange chamber. The membranes on both the heater and window chips are designed to contain a positive relative pressure – that is, the pressure should be higher inside the cell than outside. If the pressure is lower than atmospheric when the holder is removed from the column, the Si_3N_4 membrane on the window chip will peel away from the Si frame. Another failure mode is the result of the very high effective ramp rate of the heater chip. In the usual operational mode, the gas cell can accommodate some expansion of the gas contained within. If the heater chip is turned on directly to a high current, and hence a high temperature, however, when the cell is loaded with gas, a compression wave propagates across the gas cell and blows out either the window or heater membrane (or both). An example of a heater chip after this type of

failure is shown in Figure 6.11c. It is therefore preferable to ramp up the heater chip over about a second, so as not to cause too much of a pressure increase.

Finally, understanding the precise temperature of the specimen on the holder in various pressure conditions is not currently straightforward. Since there is no on-board temperature sensing on the gas cell, and each heater chip is slightly different, each chip must be calibrated manually, by applying various currents and measuring the resulting temperature with an infrared camera. This must be done before the experiment begins. However, because the heater itself has such a negligible thermal mass, the gas pressure, and even gas blend, can have a large effect on the resulting temperature from a given applied current. One such calibration chart is shown in Figure 6.12 for vacuum and two higher pressure levels. These calibrations are still not precisely correct, though, as they were made with the chip alone placed in a vacuum chamber and attached to leads. The convection situation when the chip is on the holder is different in three ways: (1) the chip is exposed to atmosphere on only one side, not both; (2) the gas may be flowing and convecting away more heat than is accounted for in a static test; and (3) if the gas is static, it is an extremely small volume (~1.5 mm^3)[7], and may contain the heat at the sample, insulating more heat than is accounted for in a relatively larger vacuum test chamber. Rigorous studies must be performed in order to accurately estimate the on-cell temperature if no on-cell measurement device is available or practical.

6.4 Conclusions

It has been found that the materials studied *in situ* – Pt:$CaTiO_3$, Rh:$CaTiO_3$, and Pt:$BaCeO_3$ – behave qualitatively as expected based on earlier studies of corresponding thin films, though not to the same extent. The precious metal precipitated from a doped perovskite extremely rapidly,

in time periods of only a few minutes at 600-800 °C when reduced varyingly aggressively. The metal that did precipitate from the oxide generally maintained very small particle sizes, and most were essentially pinned from coarsening by virtue of being contained within the perovskite host itself. Upon re-oxidation, some metal re-dissolved into the perovskite host, but most remained in apparently metallic form in small particles. Some metal that either started on or happened to precipitate onto a perovskite free surface did coarsen into larger particles. Finally, great care must be taken when operating the gas cell system, both because any number of different events can cause the cell, and hence the experiment, to fail, and because the control of the cell itself is often imprecise. It is likely this imprecision in temperature control why unexpectedly large amounts of precious metal was not able to re-dissolve back into the perovskite given appropriate redox conditions.

6.5 References

1 E.D. Boyes, P.L. Gai, "Environmental High Resolution Electron Microscopy and Applications to Chemical Science", *Ultramicroscopy* **67** 219-232 (1997).

2 R. Sharma, K. Weiss, "Development of a TEM to Study *In Situ* Structural and Chemical Changes at an Atomic Level During Gas-Solid Interactions at Elevated Temperatures", *Microsc. Res. Tech.* **42** 270-280 (1998).

3 P.L. Gai, "Probing Selective Oxidation Catalysis Under Reaction Conditions by Atomic Scale Environmental High Resolution Electron Microscopy", *Current Opinion in Sol. St. Mater. Sci.* **4** 63-73 (1999).

4 P.L. Gai, "Developments in *in situ* Environmental Cell High-Resolution Electron Microscopy and Applications to Catalysis", *Top. Catal.* **21** [4] 161-173 (2002).

5 J.F. Creemer, S. Helveg, G.H. Hoveling, S. Ullmann, A.M. Molenbroek, P.M. Sarro, H.W. Zandbergen, "Atomic-Scale Electron Microscopy at Ambient Pressure", *Ultramicroscopy* **108** 993-998 (2008).

6 L.F. Allard, W.C. Bigelow, M. Jose-Yacaman, D.P. Nackashi, J. Damiano, S.E. Mick, "A New MEMS-Based System for Ultra-High-Resolution Imaging at Elevated Temperatures", *Microsc. Res. Tech.* **72** 208-215 (2009).

7 L.F. Allard, S.H. Overbury, W.C. Bigelow, M.B. Katz, D.P. Nackashi, J. Damiano, "Novel MEMS-Based Gas-Cell/Heating Specimen Holder Provides Advanced Imaging Capabilities for *In Situ* Reaction Studies", *Microsc. Microanal.* **18** 656-666 (2012).

8 M.B. Katz, S.Y. Zhang, Y.W. Duan, H.J. Wang, M.H. Fang, K. Zhang, B.H. Li, G.W. Graham, X.Q. Pan, "Reversible Precipitation/Dissolution of Precious-Metal Clusters in Perovskite-Based Catalyst Materials: Bulk Versus Surface Re-Dispersion", *J. Catal.* **293** 145-148 (2012).

9 H. Tanaka, M. Taniguchi, M. Uenishi, N. Kajita, I. Tan, Y. Nishihata, J. Mizuki, K. Narita, M. Kimura, K. Kaneko, "Self-Regenerating Rh- and Pt-Based Perovskite Catalysts for Automotive-Emissions Control", *Angew. Chem. Int. Ed.* **45** 5998-6002 (2006).

10 M.B. Katz, G.W. Graham, Y.W. Duan, H. Liu, C. Adamo, D.G. Schlom, X.Q. Pan, "Self-Regeneration of Pd-$LaFeO_3$ Catalysts: New Insight from Atomic-Resolution Electron Microscopy", *J. Amer. Chem. Soc.* **133** [45] 18090-18093 (2011).

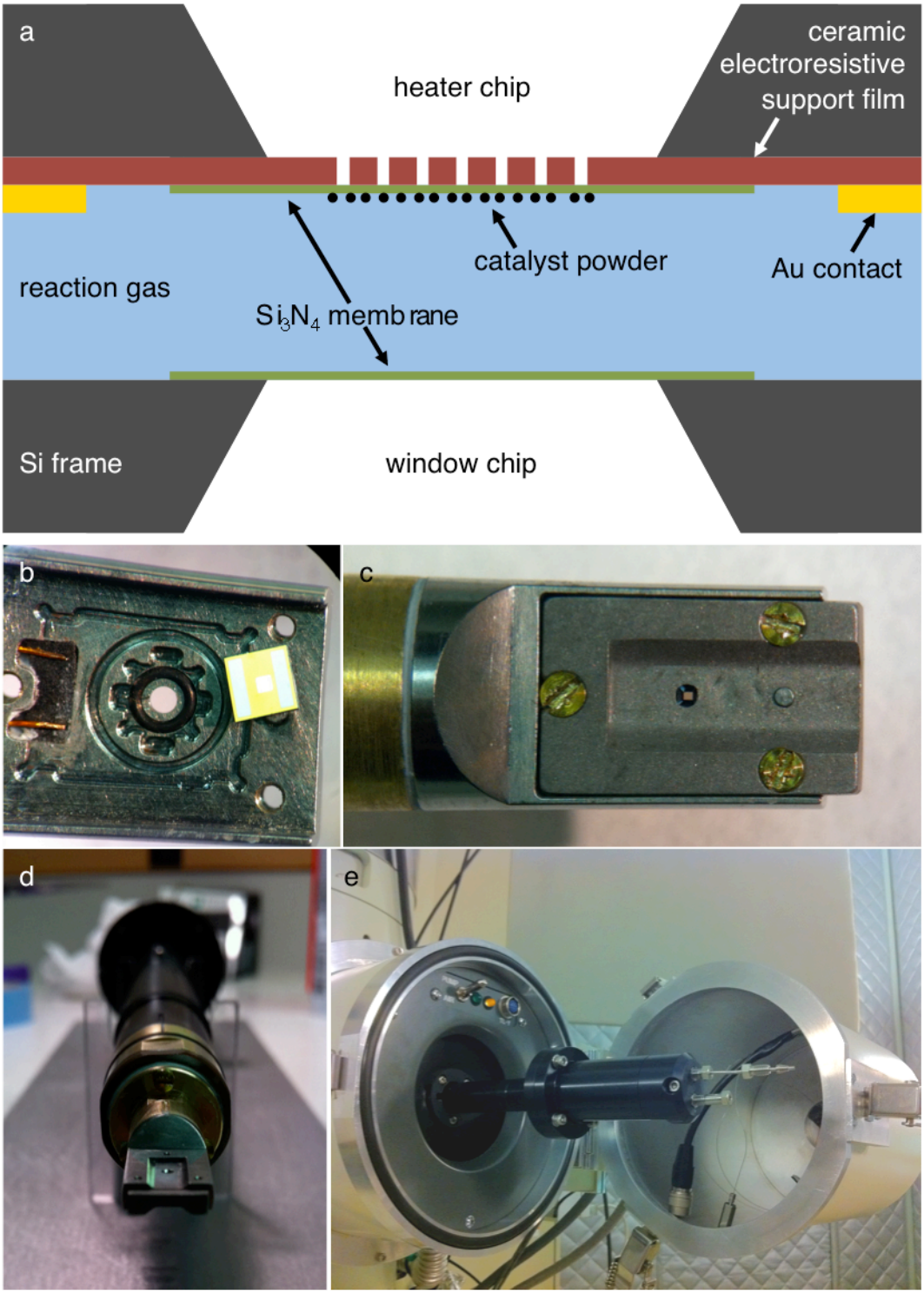

Figure 6.1. (a) A schematic of the relevant components of the gas cell and photographs of the larger holder device structure, specifically (b) the heater chip resting on the open holder tip, (c) the holder tip after sealing shut, (d) the holder from the end on, and (e) the holder in the pump position in the specimen transfer chamber, showing the gas feed nozzles coming out the back of the holder assembly. (Photographs courtesy L.F. Allard.)

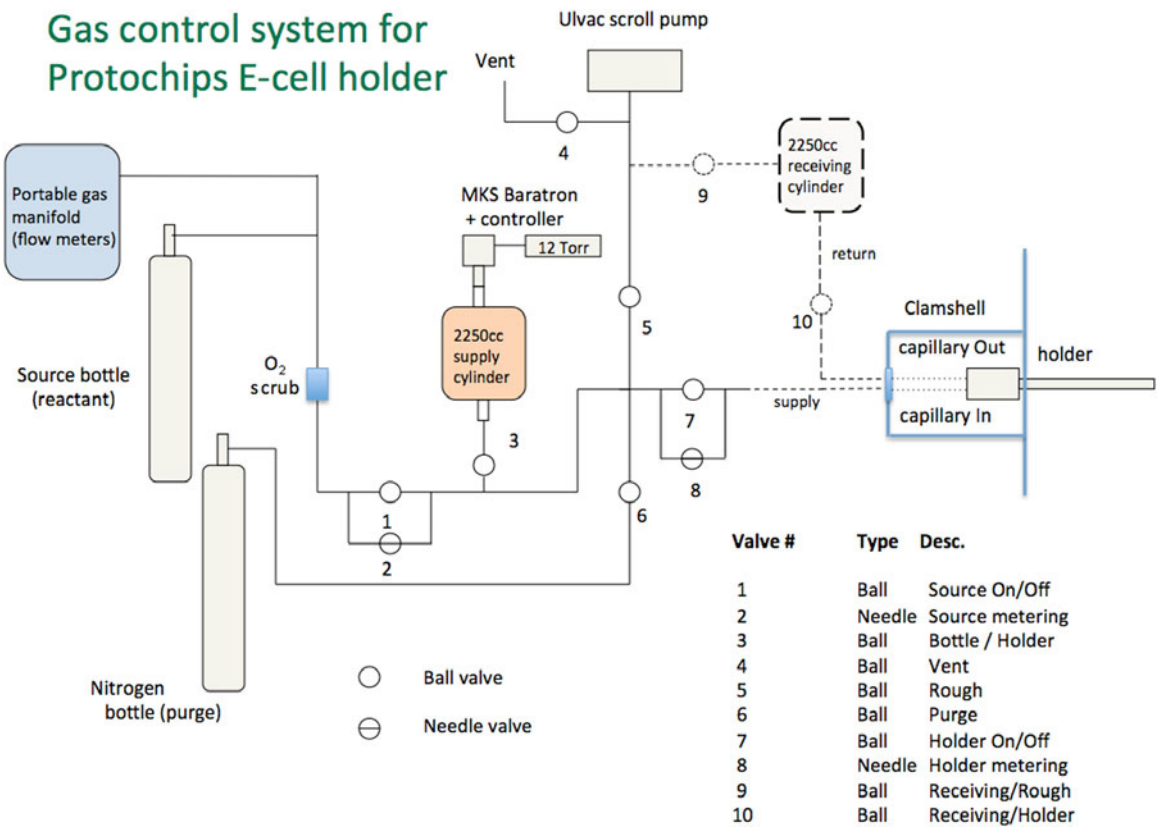

Figure 6.2. A schematic of the gas control system for the gas cell. (after Reference 7)

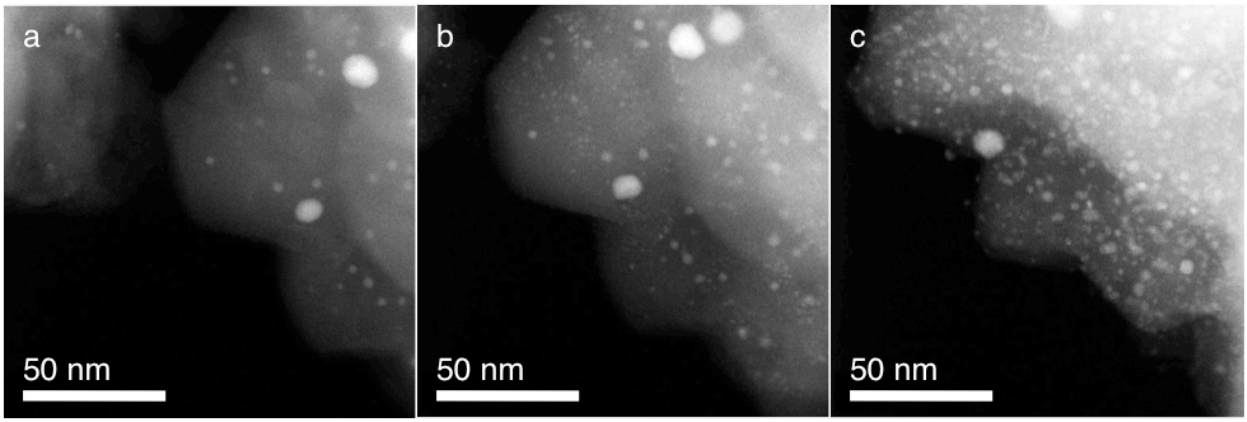

Figure 6.3. Sequential STEM images of the same region of a Pt:$CaTiO_3$ specimen (a) as prepared, (b) after 5 min of heating to 600 °C in vacuum, and (c) after an additional 5 min of heating at 800 °C in vacuum.

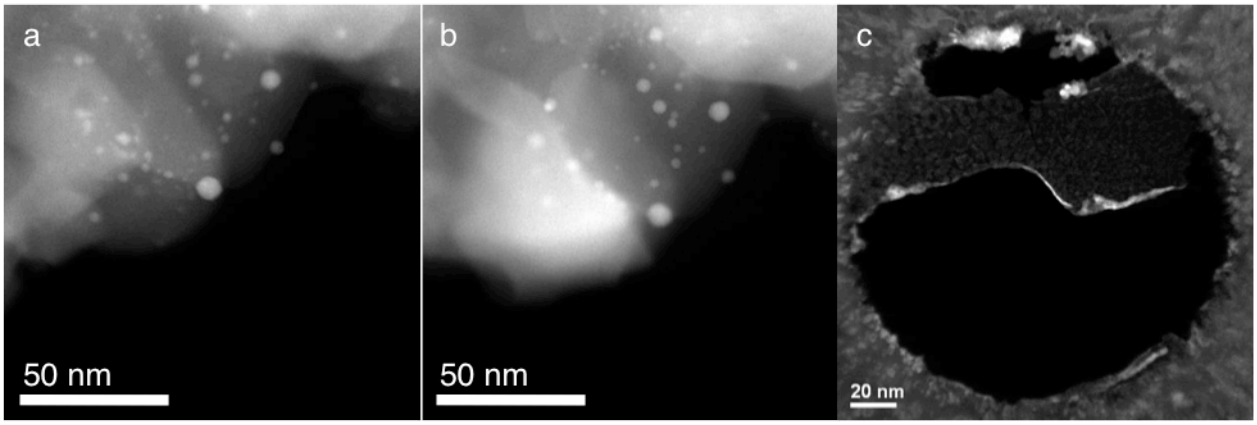

Figure 6.4. Sequential STEM images of a pre-reduced Pt:$CaTiO_3$ after (a) 10 min at 800 °C in lab air and (b) after 100 min at 800 °C in lab air. (c) After exposure to reducing conditions, the support membrane experienced a chemical reaction or phase change and curled up on itself.

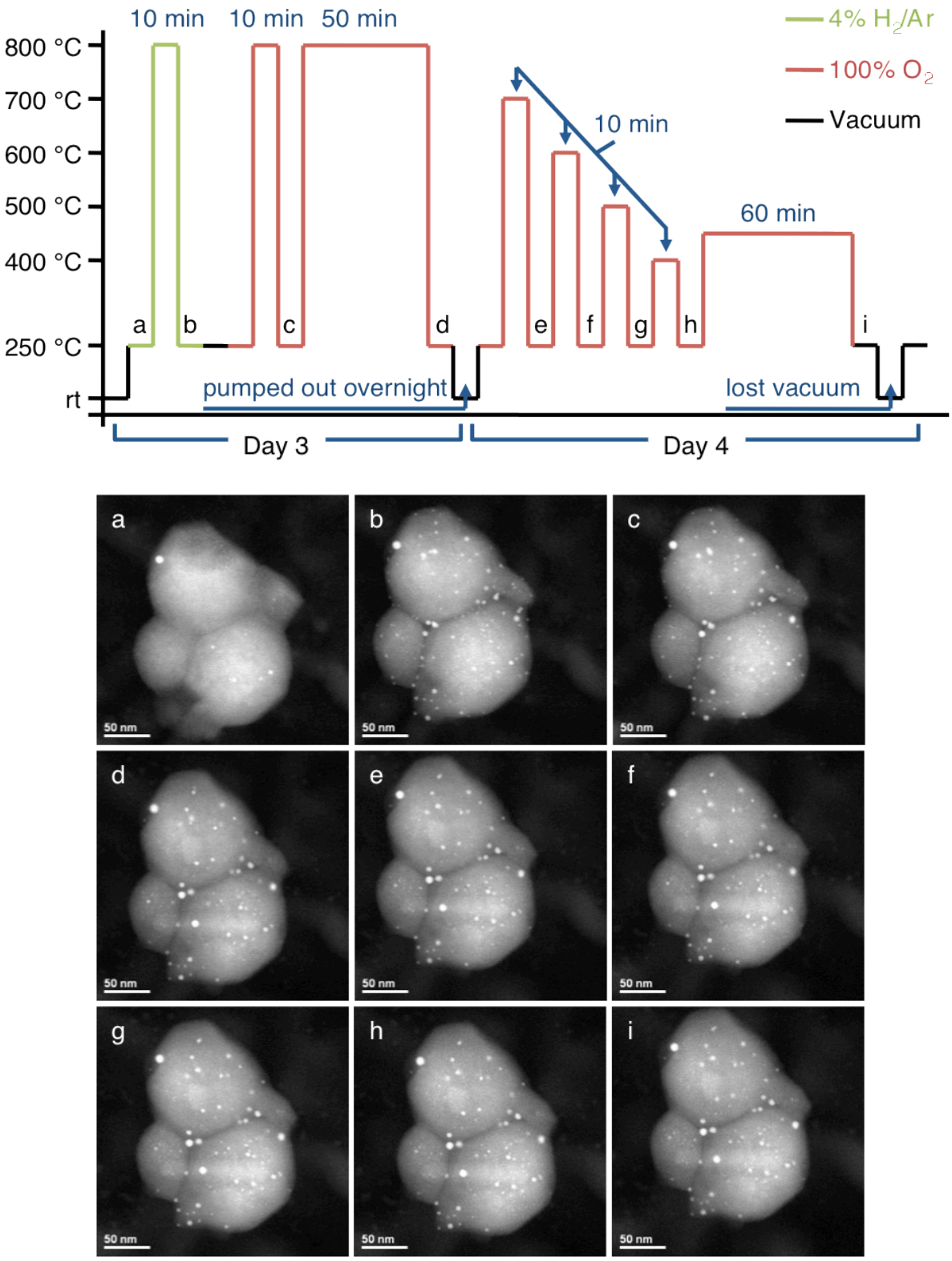

Figure 6.5. The experimental redox processing procedure, along with images corresponding to each of the points labeled on the schematic.

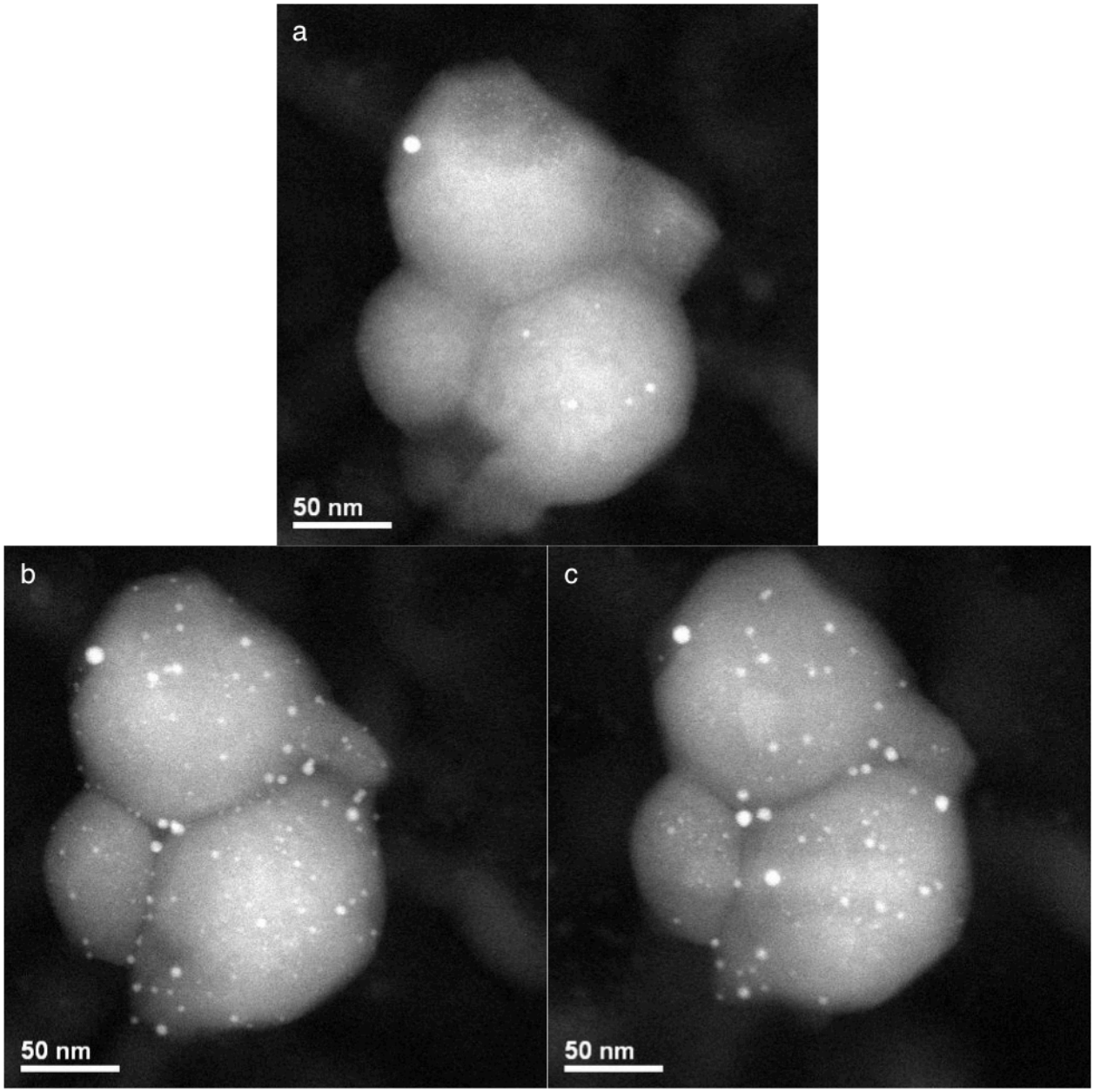

Figure 6.6. Three frames taken from the process outlined by the schematic in Figure 6.5: (a) the as-prepared view, (b) after reduction, and (c) after all oxidation procedures.

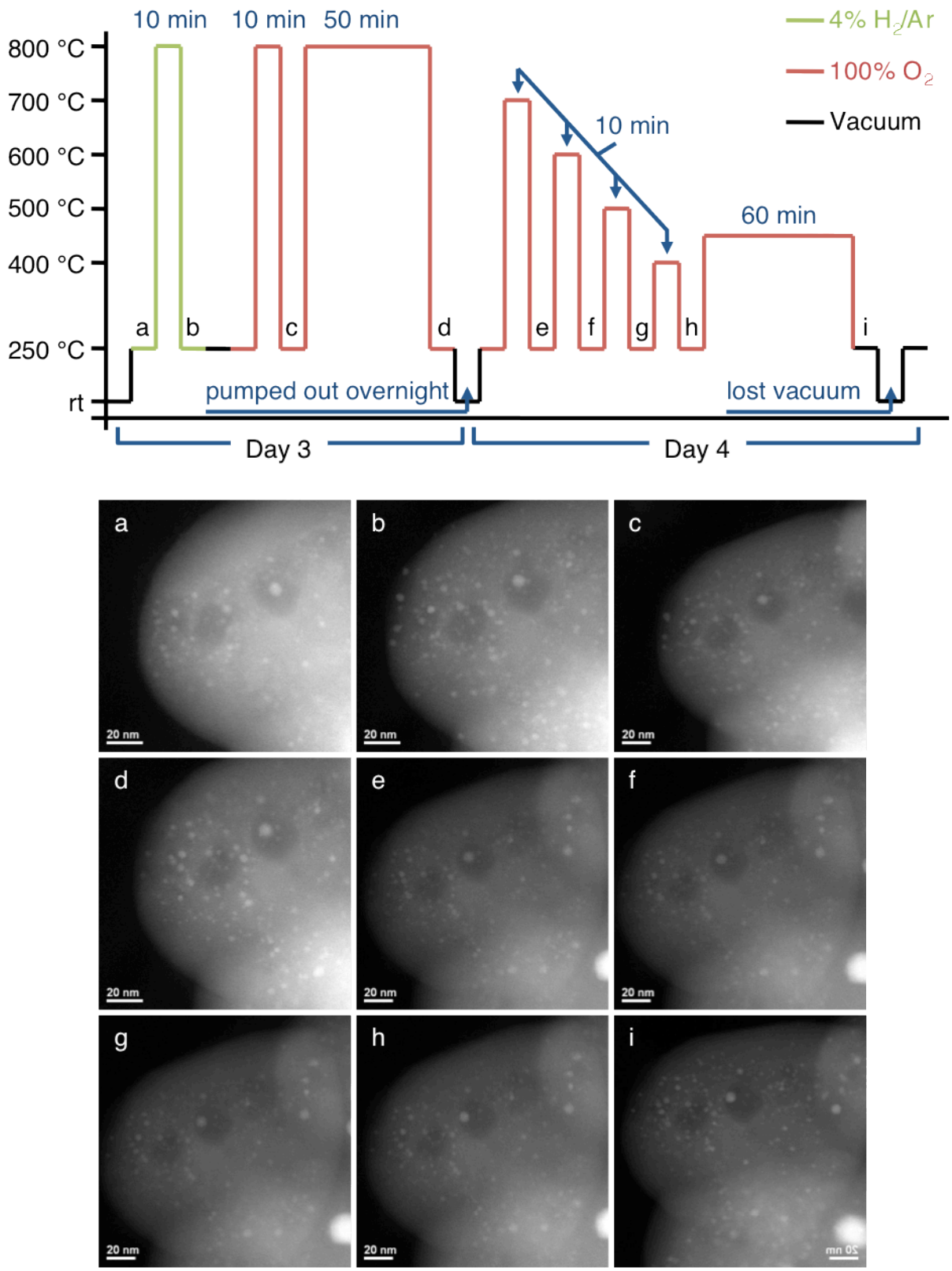

Figure 6.7. The experimental redox processing procedure, along with images corresponding to each of the points labeled on the schematic.

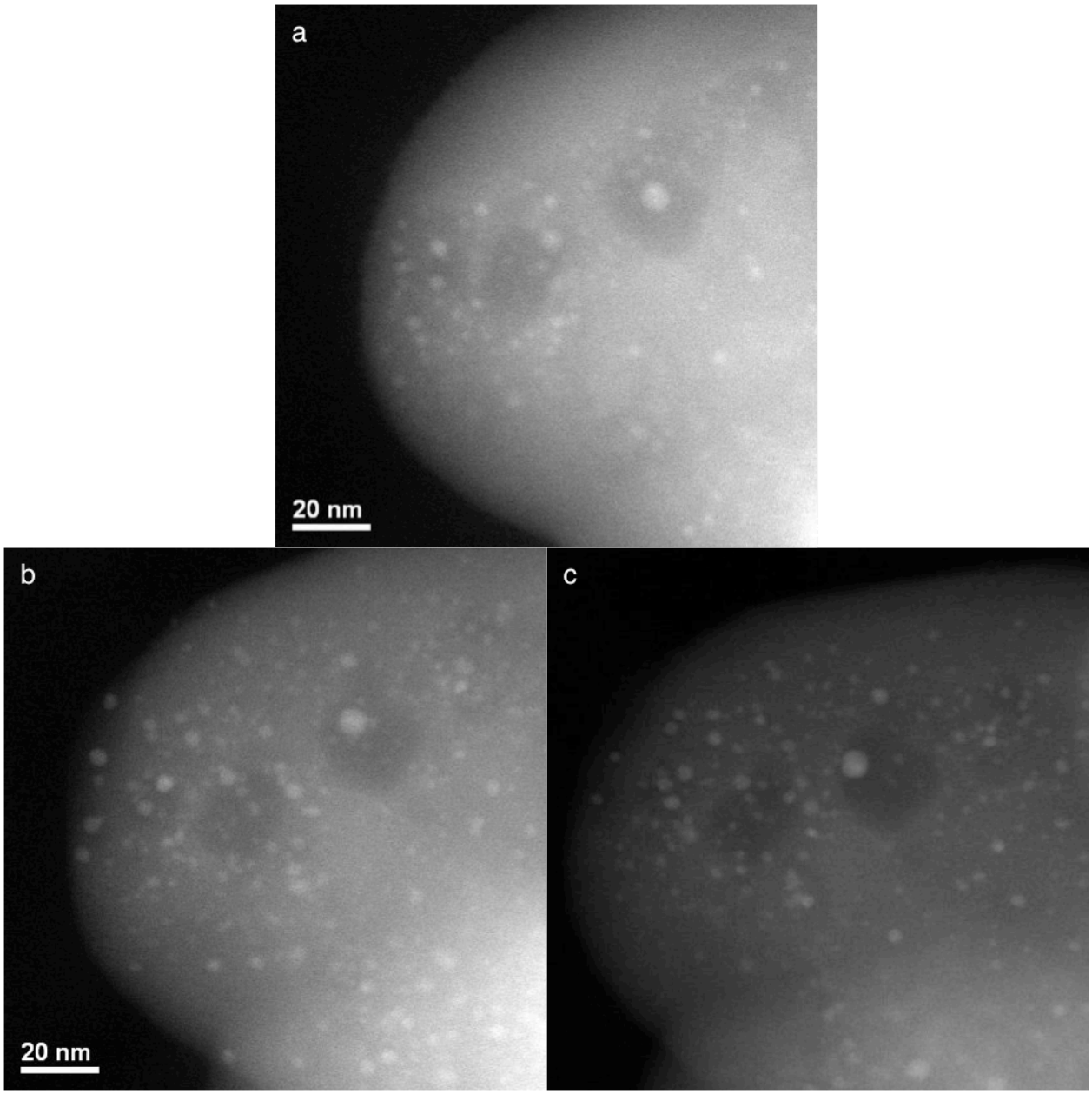

Figure 6.8. Three frames taken from the process outlined by the schematic in Figure 6.7: (a) the as-prepared view, (b) after reduction, and (c) after all oxidation procedures.

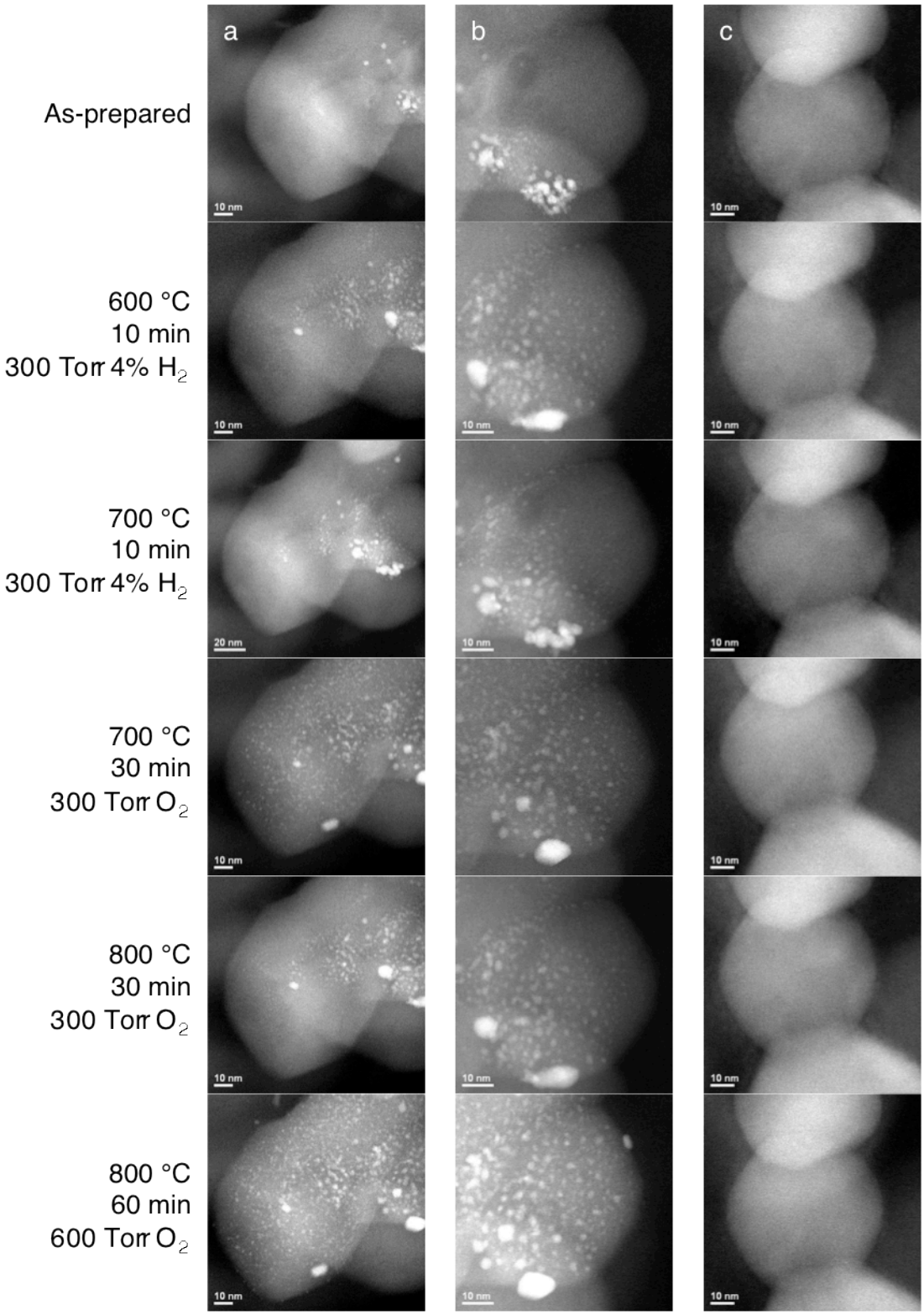

Figure 6.9. STEM images of three different regions from a Pt:$CaTiO_3$ specimen after each of the subsequent redox processing steps listed in the left column.

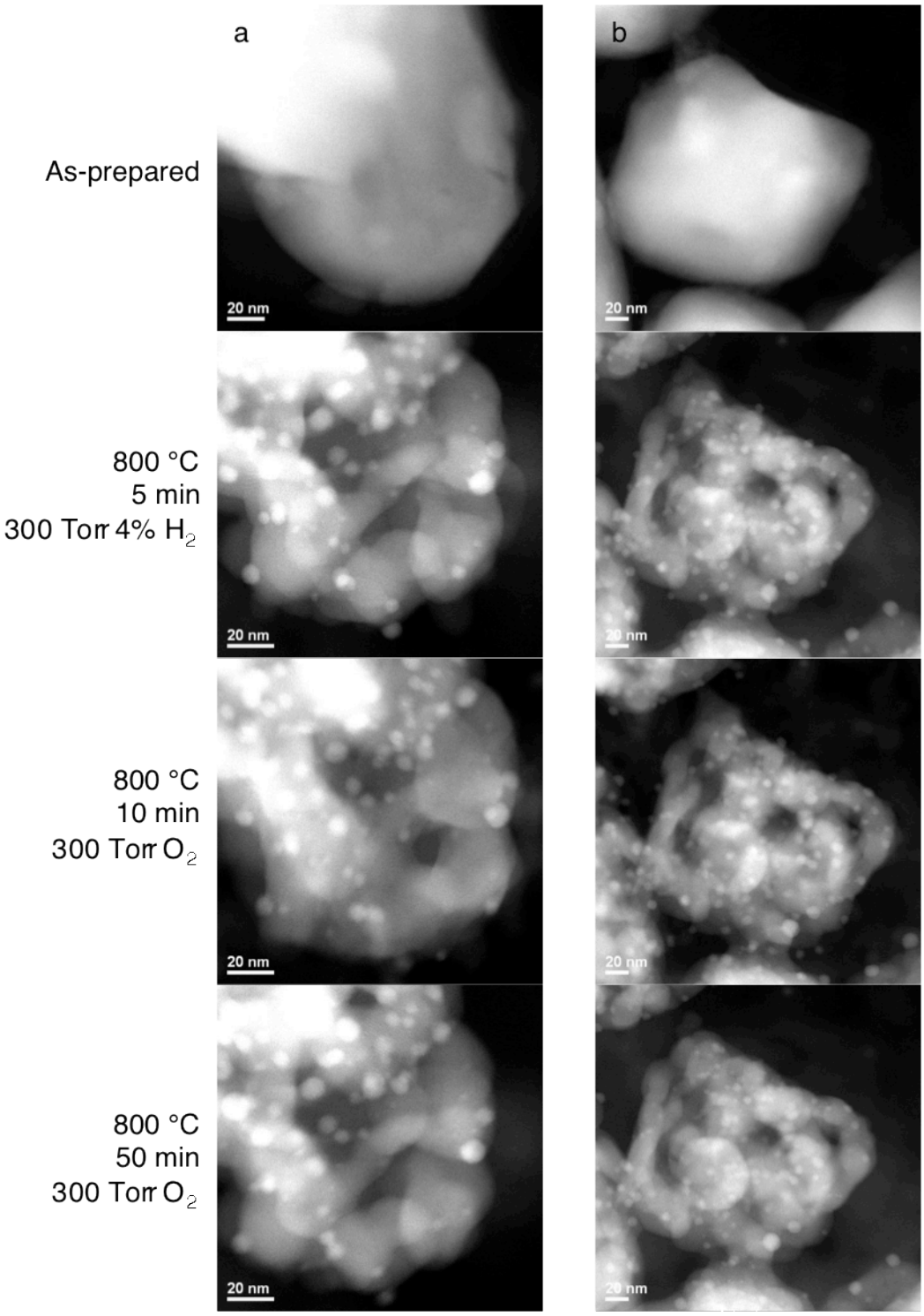

Figure 6.10. STEM images of two different regions from a Pt:$BaCeO_3$ specimen after each of the subsequent redox processing steps listed in the left column.

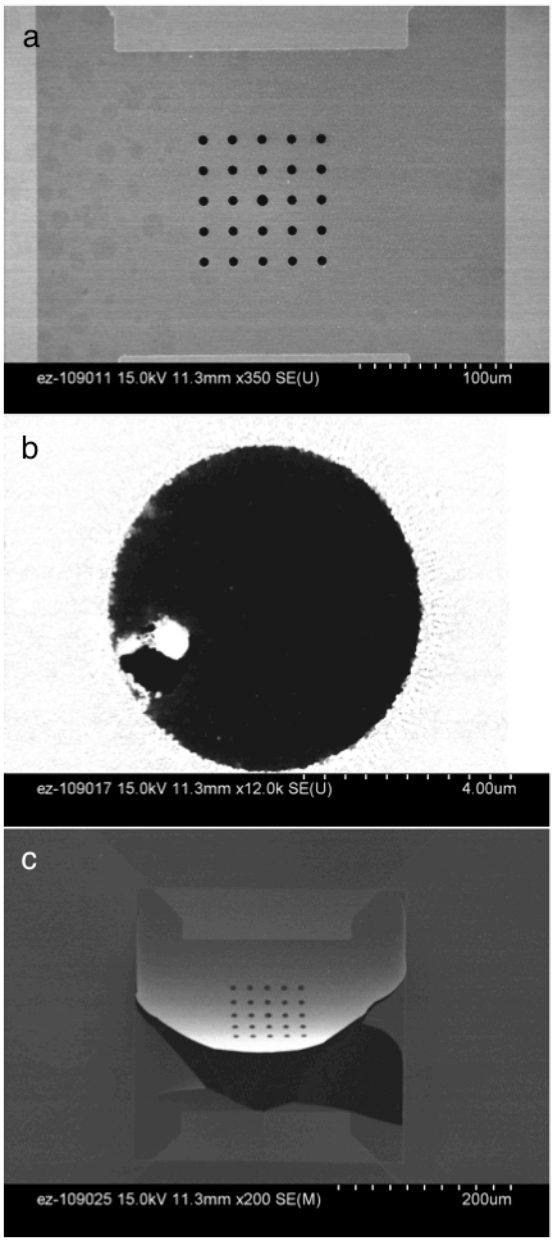

Figure 6.11. Scanning electron microscope images of (a) a pristine gas cell heater chip, (b) a defective hole on a heater chip with a rupture caused by debris present during manufacture, and (c) a heater chip membrane after being blown out by overpressure.

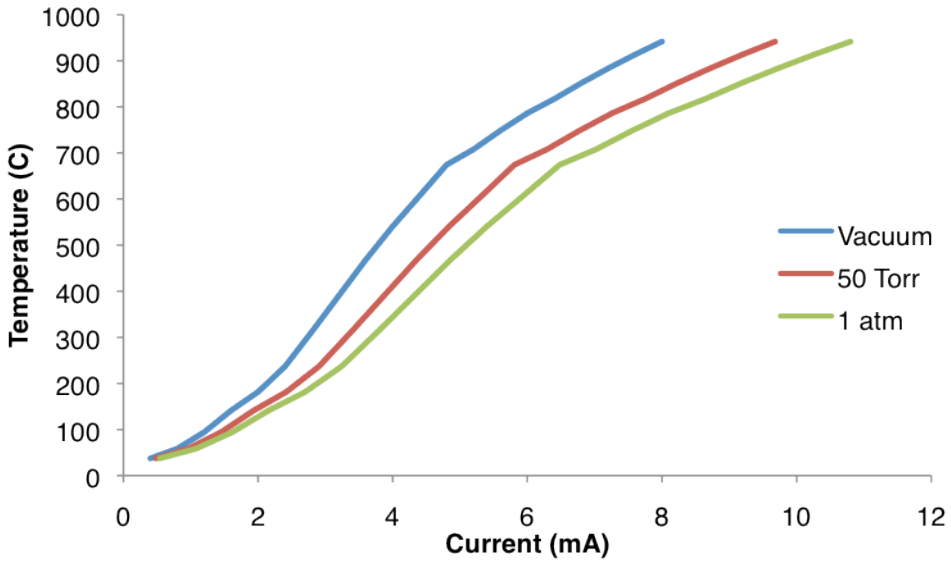

Figure 6.12. Current-temperature calibration curve for a heater chip under different gas pressures.

Chapter VII

Summary and Future Work

7.1 Summary

Presented here is a detailed study and analysis of the various so-called 'intelligent catalysts' proposed by Daihatsu Motor Company, which have been heretofore examined only by bulk x-ray absorption techniques – x-ray absorption near-edge structure and extended x-ray absorption fine-structure spectroscopies. Advanced analytical transmission electron microscopy, paired with state of the art *in situ* techniques, and complemented with extensive density functional theory phase calculations, were used to show the operational mechanisms at play in this class of catalysts.

This work has shown the Pd:$LaFeO_3$ system not to behave in the expected 'self-regenerative' way accepted in prior literature. Pd neither exits the $LaFeO_3$ support easily upon reduction, nor dissolves readily upon oxidation, given simulated aggressive aging conditions, though x-ray energy-dispersive spectroscopy mapping indicates it does, to a limited extent, displace Fe in local regions of the oxide. The most interesting and perhaps most useful aspect of the Pd:$LaFeO_3$ system is what can be termed 'self-stabilization', that is the Pd particles on the $LaFeO_3$ surface, upon oxidation, and maintaining through redox cycling, sink partially into the support, displacing the oxide material itself. These particles create approximately hemispherical divots within the support, which provide for increased mechanical stability against migration and

coarsening of Pd particles, serving to theoretically maintain a high dispersion over the same catalyst on a non-interacting substrate. Density functional theory calculations hint that this process may be the result of the combination of the switching of the stable terminating surface of $LaFeO_3$ between LaO^+ and FeO_2^- under various redox conditions and highly non-congruent interaction energies of Pd with each surface, respectively.

The other major thrust of this work pertains to the Pt:$CaTiO_3$ (and, to a lesser extent, the Rh:$CaTiO_3$) system, also proposed by Daihatsu as an 'intelligent catalyst'. It has been shown conclusively, through extensive transmission electron microscopy analysis, that though the catalyst metal does indeed dissolve into and precipitate out of the perovskite support upon oxidizing and reducing conditions, respectively, the metal does not, as was suggested by Daihatsu, transport itself to the surface of the support, either atomically or by correlated mass transport as a whole particle. A preponderance of other phenomena, including the formation of secondary TiO_2 phases and amorphous inclusions, also appear in the support, variously under oxidizing and reducing conditions. Pseudo-ternary CaO_x-TiO_y-PtO_x phase diagrams were calculated for several temperatures and oxygen pressures that can explain both the formation of these secondary phases as well as the origin of the 'intelligent catalyst' or 'self-regenerative catalyst' phenomenon itself. The phenomenon originates from the alternating stability and instability of Pt existing within the primary perovskite as a solid solution. Under oxidizing conditions, Pt is stable as a dopant within $CaTiO_3$, TiO_2 (a), and $CaTi_5O_{11}$, which exist in equilibrium, but becomes unstable under reducing conditions, causing it to precipitate out of its various host oxides and metalize.

Advanced *in situ* transmission electron microscopy equipment and techniques were utilized to attempt to observe transient phenomena in the various self-regenerative catalyst systems, including Pt:$CaTiO_3$, Rh:$CaTiO_3$, and Pt:$BaCeO_3$. These experiments took advantage of the unique capabilities of the *in situ* sample stage to both apply high temperatures – up to 1200 °C, in principle – and gas pressures up to a full atmosphere. This set of experiments made apparent the extremely rapid precipitation of the various metal species out of the perovskite, which happens in only seconds or minutes under even mild reduction conditions. The converse reaction, attempting to drive the re-dissolution of the catalyst back into the perovskite lattice, is much more difficult, though. Even extremely oxidizing environments, with a pure oxygen gas at nearly a full atmosphere of pressure, was only partially effective in driving some of the catalyst back into the perovskite. It is difficult, at this point in the development of the equipment, to ascribe the entire lack of oxidation reaction to the material itself, though, as there are still aspects of the gas cell in the holder that may give rise to peculiar sample artifacts. Overall, the results of the *in situ* work largely corroborate the results from the previous thin film work.

Finally, new insights (Appendix A) into the interactions of $CaTiO_3$ and $LaFeO_3$ are presented. Using epitaxial thin films as a basis for a diffusion couple, the large-scale diffusion of La from $LaFeO_3$ into $CaTiO_3$ is observed, with no detectable counterdiffusion of Ca or Ti. La was shown, through scanning transmission electron microscopy and electron energy-loss spectroscopy, to occupy the a-site in $CaTiO_3$, effectively substituting for Ca. The diffusion length was found to be a few nanometers in the $CaTiO_3$ bulk and many tens of nanometers along extended defects within the film. Additionally, two as yet unreported cation-ordered structures, postulated to be $La_{0.5}Ca_{0.5}TiO_3$ and $La_{0.75}Ca_{0.75}TiO_3$ were discovered. Charge balance is compensated for by partial reduction of local Ti ions from Ti^{4+} to Ti^{3+}.

7.2 Future Work

Major work can continue from this dissertation along three major thrusts. The first is a continuance of the general investigations into the various self-regenerative catalyst systems. This report presents extensively data on only two systems, Pd:$LaFeO_3$ and Pt:$CaTiO_3$. It is hypothesized that this sort of self-regenerative effect can take place in a wide variety of perovskites and metals, depending of course on the specific thermodynamics and crystal chemistries at work in those cases. The ability of a metal to dissolve into the perovskite and precipitate back out is expected to depend strongly on its ability to switch between its oxide and metal forms. Gold is not generally stable as an oxide, and is not expected to function in this way. Neither is titanium easily reduced to a metallic form. Investigating the bounds of these stabilities and their relationships to their perovskite hosts will no doubt prove to be quite scientifically interesting.

Exploring a more practical application, the morphological tailoring of the self-regenerative catalyst may prove to be the key in utilizing it in a real production catalyst. Since it seems not to be a straightforward venture to get the metal precipitating out of the perovskite upon reduction to the surface, where it will be catalytically useful, the surface may be brought to the metal. One could imagine a thin, conformal coating of Pt:$CaTiO_3$ around a stable, high-surface-area support in which the perovskite is about 2 or so nanometers thick. This would increase the likelihood that any metal particle that forms would be at least partially exposed to a free surface and, in turn to the gas to be catalyzed. Thus far, only very preliminary investigations have been performed into whether this can be easily accomplished and, in turn, how effective it might be. Scanning transmission electron microscope images of such a film is shown in Figure 7.1. This film, at 15 nm, is slightly thicker than is surmised would be ideal, but growing very thin crystalline films by

pulsed laser deposition has proven difficult thus far. In any case, a more applicable laboratory would likely be atomic layer deposition, which does not rely on ballistic deposition and can conformally coat complex surfaces, such as a high surface area support. For large-scale production, though, synthesis of this layered material would likely require the use of various solution processes.

Finally, continuing the *in situ* work may prove to be quite fruitful. Currently, work is limited by technical problems, as the system used in the work presented here is a prototype, still in the developmental stages. Once these technical problems are mitigated and a stable, easy to use system is available, the dynamics of the various self-regenerative systems can be studied in much greater depth.

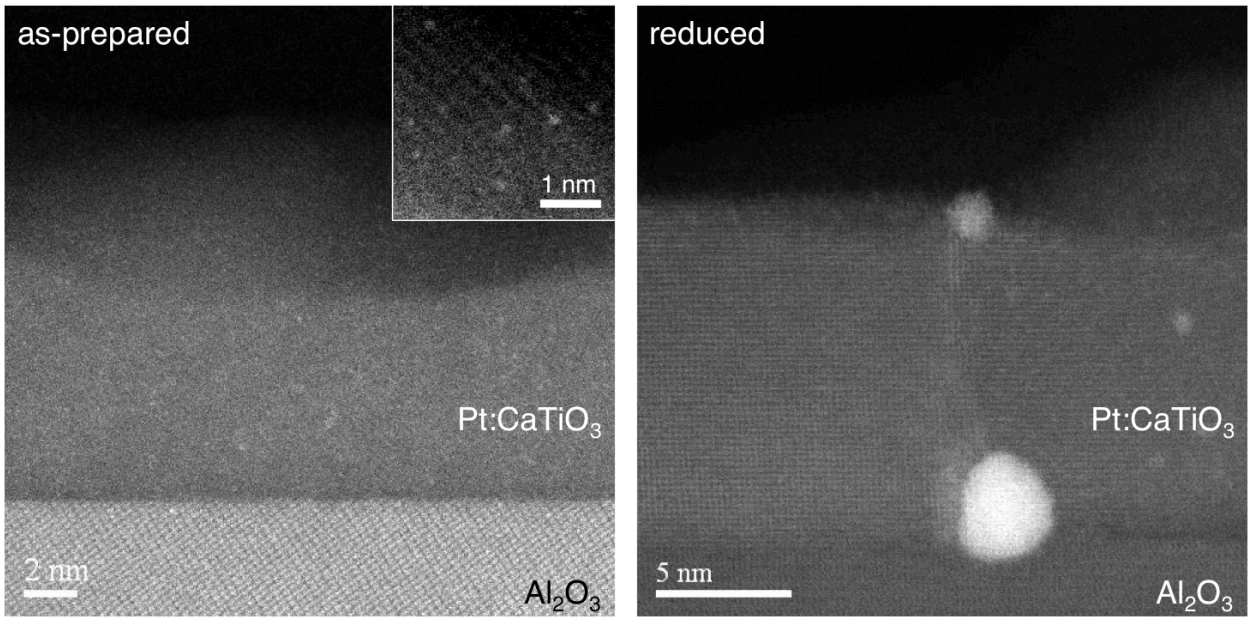

Figure 7.1. Ultra-thin films of Pt:$CaTiO_3$ as deposited (left) and after reduction (right). Inset: High-resolution image of atomically-dispersed Pt in the as-prepared film.

Appendix A

Lanthanum Diffusion Across the $LaFeO_3/CaTiO_3$ Interface

A.1 Introduction and Background

During the course of the oxidation experiments outlined in Chapter 3, anomalous diffusion behavior occurring along the interface between the $LaFeO_3$ film and the $CaTiO_3$ diffusion barrier layer were discovered. Specifically, in scanning transmission electron microscopy (STEM) imaging, it appeared as if a heavy species was diffusing into the $CaTiO_3$ layer, presumably either La or Fe from the overlying perovskite layer. An investigation was hence undertaken into this phenomenon using microscopy and spectroscopy.

In the literature, solid solutions of $CaTiO_3$ and $LaFeO_3$ ($La_xCa_{1-x}TiO_{3-\delta}$ or $La_{2(1-x)/3}Ca_xTiO_{3-\delta}$, depending upon the Ti formal oxidation state) is one system under general consideration for, among other applications, solid oxide fuel cell anodes. While these solid solutions have been studied, primarily by x-ray diffraction, diffusion couples of the two constituent materials and their interface have yet to be examined in detail.[1-3] In this work, direct imaging and chemical mapping of La diffusion from $LaFeO_3$ into $CaTiO_3$ as well is provided as evidence of two different ordered La-doped $CaTiO_3$ compounds.

A.2 Experimental Methods

$LaFeO_3/CaTiO_3$ perovskite bilayer thin films were grown on $SrTiO_3$ (001) substrates by pulsed laser deposition. The $CaTiO_3$ and $LaFeO_3$ films were grown for 40 minutes and 20 minutes, respectively, in 40 mTorr oxygen with the substrate held at 750 °C. The deposition utilized a KrF excimer laser (248 nm) operated at 200 mJ pulses at 10 Hz. The films were then annealed under flowing 20% O_2 (bal. N_2) at 800 °C for 1 hour.

Following heat treatments, thin films were sectioned into cross-sectional TEM specimens. These specimens were mechanically polished on diamond-embedded lapping films, followed by final thinning by argon ion milling (Gatan PIPS model 691) to electron transparency. TEM specimens were examined using JEOL JEM-2100F STEMs equipped with spherical aberration correctors and spectrometers for X-ray energy-dispersive spectroscopy (XEDS; JEOL and EDAX) and electron energy-loss spectroscopy (EELS; Gatan).

A.3 Results and Discussion

Examination of the thin film cross sections, a typical image of which is shown in Figure A.1, revealed large-scale diffusion of La out of the $LaFeO_3$ layer into the $CaTiO_3$ layer. This is readily apparent due to the Z-contrast nature of HAADF imaging, given that La, at Z = 57, is much larger than the other species present (O, Ca, Ti, and Fe have atomic numbers of 8, 20, 22, and 26, respectively). This diffused La appears to occupy exclusively the perovskite a-site of the host $CaTiO_3$, formerly occupied by Ca – no instances of La on a b-site could be identified in the specimens studied. The identity of the heavy species was confirmed to be La by atomic-resolution EELS mapping,[4] shown in Figure A.2. It is worth noting that no evidence of counter-diffusion by Ca into the $LaFeO_3$ layer could be found. Several regions of the $LaFeO_3$, about

5-10% by volume, had also transformed into La_2O_3, indicating a superstoichiometric amount of La in the film. This was indeed shown to be the case by XWDS, which gave a La:Fe ratio of 1.18.

In the majority of regions of the $LaFeO_3/CaTiO_3$ interface, La uniformly diffused into the $CaTiO_3$ about 2 to 3 nm. In some local regions, however, the La diffused far deeper into the $CaTiO_3$, seemingly following fast diffusion channels running through the $CaTiO_3$ normal to the plane of the film, shown in Figure A.3. These channels are generally 1-2 nm wide and appear to permeate completely to the $CaTiO_3/SrTiO_3$ interface, though La diffusing through their entire length is only seen on a few. These channels are likely the boundaries between orthorhombic rotation domains in the $CaTiO_3$, as the crystals on either side of the channels generally have slightly different orientation (HAADF-STEM imaging is very sensitive to the crystal orientation). There is no apparent difference between the films given reduction treatments at different temperatures. The extent of La diffusion therefore seems entirely dependant upon the 800 °C oxidation step, possibly due to slow kinetics at the lower temperatures during reduction.

Diffusion of La was also enhanced along the boundaries between $CaTiO_3$ and internal domains of anatase TiO_2 that had formed during deposition, again likely due to super-stoichiometric concentrations of Ti, as shown in Figure A.4. The anatase TiO_2 has an epitaxial orientation relationship with the $CaTiO_3$ matrix of $[100](100)_{anatase}||[100](100)_{perovskite}$, but the epitaxy exists only along the a-b plane of the anatase, a = b = 3.784 Å, which is only a 2.6% mismatch with the pseudocubic lattice parameter of $CaTiO_3$ (~3.825 Å). The c-axis of anatase, however, is 9.515 Å, a very large mismatch with $CaTiO_3$. These boundaries, which are of higher energy than the bulk, are known to be pathways for rapid diffusion. Along both types of boundaries, as with the

shorter interface diffusion, La occupied exclusively the a-site, substituting again for Ca, as shown in Figure A.5.

This contrast in behavior between the diffusion of La through the $CaTiO_3$ crystal and along the internal boundaries in the $CaTiO_3$ film ($CaTiO_3/TiO_{2,anatase}$ and $CaTiO_{3,[100]}/CaTiO_{3,[010]}$) is to be expected. Cation diffusion and self-diffusion in perovskites, as with most crystalline solids, is known to be much more facile along grain boundaries than through the bulk, with diffusion lengths increased by about two orders of magnitude at 800 °C. Though no such values in published literature could be found regarding the diffusivity of La in $CaTiO_3$, the diffusivity of La in other perovskites, and that of other cations in $CaTiO_3$, suggest a diffusion length of about 1-3 nm and 300-500 nm for heavy cations in perovskites through bulk crystals and along grain boundaries, respectively, in qualitative agreement with this work.

Close examination of the diffusion zone using atomic-resolution HAADF-STEM reveals apparent La/Ca a-site ordering, reminiscent of double or compound perovskites, as shown in Figure A.6a. The majority of the ordered regions show sequential bright-dark contrast between successive a-site layers, suggesting alternating LaO and CaO layers (interspersed, of course, with TiO_2 layers). HAADF intensity mapping, however, shows that the intensity of the atomic columns in the fainter layers is too high (compared to nearby CaO columns within $CaTiO_3$) to simply be CaO, suggesting some LaO substitution in that layer as well, as shown in Figure A.6b. The layering sequence can thus be determined to be LaO-$La_xCa_{1-x}O$, with x likely close to 0.5, giving an overall composition of $La_{0.75}Ca_{0.25}TiO_3$. A model of this ordering scheme is shown in Figure A.6e Other small ordered regions exhibit an even more sophisticated ordering pattern. These regions comprise a two-by-two repeating pattern, shown in Figure A.6c,d, with one bright

column and a diagonally opposite faint column, with the two remaining columns of an approximately equal intermediate contrast. Because the brightest columns appear to be of comparable contrast to the LaO columns in $LaFeO_3$ and the faintest columns comparable to the CaO columns in $CaTiO_3$, the three columns can be deduced to be LaO, $La_{0.5}Ca_{0.5}O$, and CaO. One possible a-site ordering for this structure is shown in Figure A.6f.

Though some evidence of ordering in heavily La-doped $CaTiO_3$ system has been published previously, this type of ordering is distinct from that discussed above. This previously published ordering is oxygen vacancy ordering on the a-site sheets, with the La and Ca cations randomly arranged. Those reports, however, refer to a solid solution of $CaTiO_3$ and $La_{2/3}TiO_3$ ($La_{2(1-x)/3}Ca_xTiO_3$), which would be a-site deficient for any amount of La doping because of the lack of accounting for any charge compensation by a local reduction of an adjacent b-site Ti^{4+} to Ti^{3+} to compensate for the addition of the La^{3+} cation in place of the Ca^{2+}. A non-a-site-deficient $LaTiO_3$, with a Ti^{3+} cation, is well known to exist in general, however. Since the EELS edge structures of the $L_{2,3}$ edge of Ti^{4+} and Ti^{3+} are mutually distinct, direct observation of the presence of Ti^{3+} by spectroscopy is possible.[5] Indeed, an EEL spectrum from the diffusion zone is shown in Figure A.7. It is not possibly, however, to discount the possibility of any a-site vacancies, and it is therefore unknown in the thin films in this work whether the oxygen vacancy charge compensation mechanism is at work to any extent and, subsequently, what the total oxygen occupancy around the La-ordered and substituted regions are.

A.4 Conclusions

Single crystal thin films heterostructures of $LaFeO_3$ on $CaTiO_3$ on $SrTiO_3$ substrates were fabricated by pulsed laser deposition and subjected to an hour each of oxidation at 800 °C and

reduction at lower temperatures. After heat treatment, La diffused into the $CaTiO_3$ approximately 2-3 nm in the bulk and through the totality of internal boundaries within the $CaTiO_3$, substituting for the Ca cations on the perovskite a-site, with no Ca counter-diffusion into the $LaFeO_3$ detected. In certain areas of the diffusion zone with high La concentrations, the La formed two types of substitutional ordering which have not been reported previously.

A.5 References

1. V. Vashook, L. Vasylechko, M. Knapp, H. Ullmann, U. Guth, "Lanthanum Doped Calcium Titanates: Synthesis, Crystal Structure, Thermal Expansion and Transport Properties", *J. Alloys Comp.* **354** 13-23 (2003).
2. V. Vashook, L. Vasylechko, N. Trofimenko, M. Kuznecov, P. Otchik, J. Zosel, U. Guth, "A-Site Deficient Perovskite-Type Compounds in the Ternary $CaTiO_3$-$LaCrO_3$-$La_{2/3}TiO_3$ System", *J. Alloys Comp.* **419** 271-280 (2006).
3. L. Vasylechko, V. Vashook, U. Guth, "$CaTiO_3$-$LaCrO_3$-$CaCrO_3$ and $CaTiO_3$-$LaCrO_3$-$La_{2/3}TiO_3$ Quasi-Ternary Systems", *Fuel Cell Technologies: State and Perspectives*, Springer 373-380 (2005).
4. D.A. Muller, L. Fitting Kourkoutis, M. Murfitt, J.H. Song, H.Y. Hwang, J. Silcox, N. Dellby, O.L. Krivanek, "Atomic-Scale Chemical Imaging of Composition and Bonding by Aberration-Corrected Microscopy", *Science* **319** 1073-1076 (2008).
5. Z.L. Zhang, W. Sigle, W. Kurtz, M. Rühle, "Electronic and Atomic Structure of a Dissociated Dislocation in $SrTiO_3$", *Phys. Rev. B* **66** 214112-1-7 (2002).

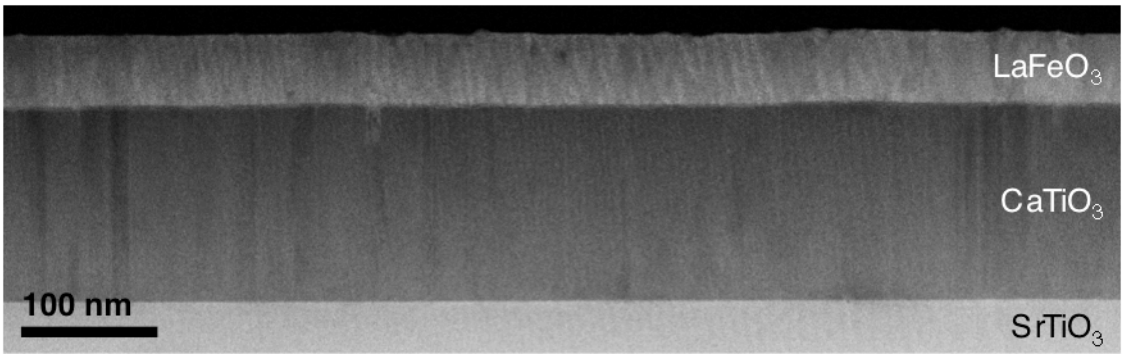

Figure A.1. HAADF-STEM image of the overall structure of the thin film stack.

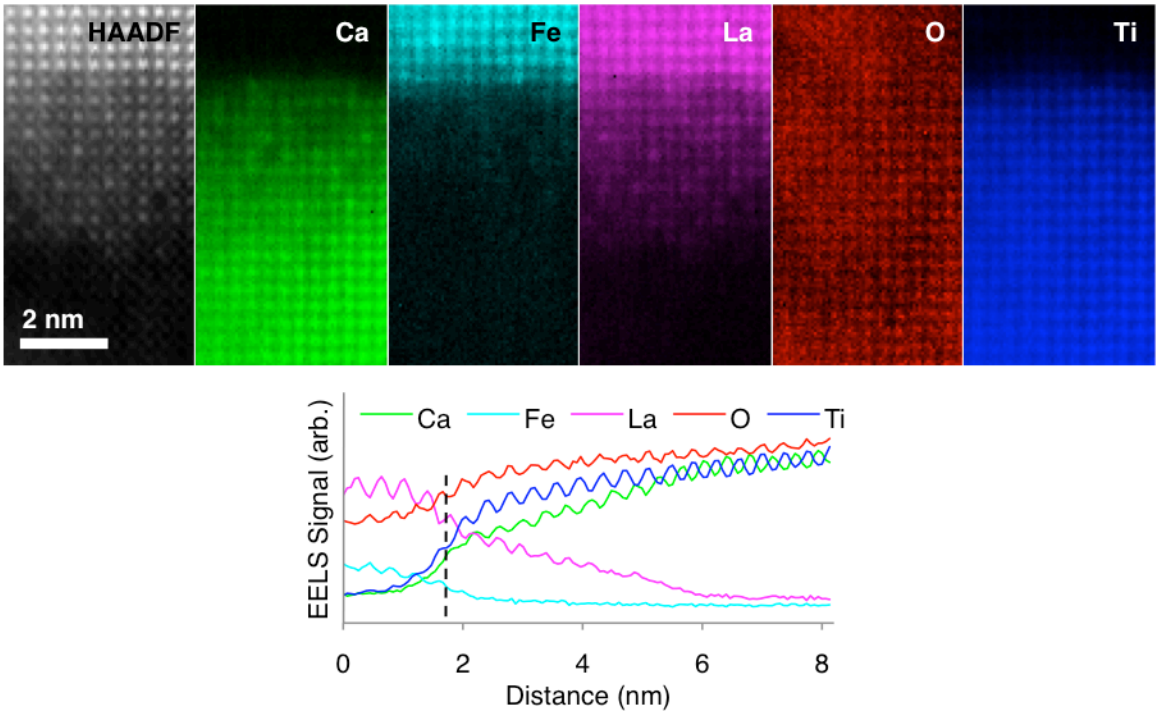

Figure A.2. EELS edge intensity maps for each atomic species present at the $CaTiO_3/LaFeO_3$ interface, along with the associated HAADF image. Significant La diffusion across the interface is plainly visible in the HAADF image and La maps, as well as in the signal profiles below. (Dashed line on plot indicates the structural interface.)

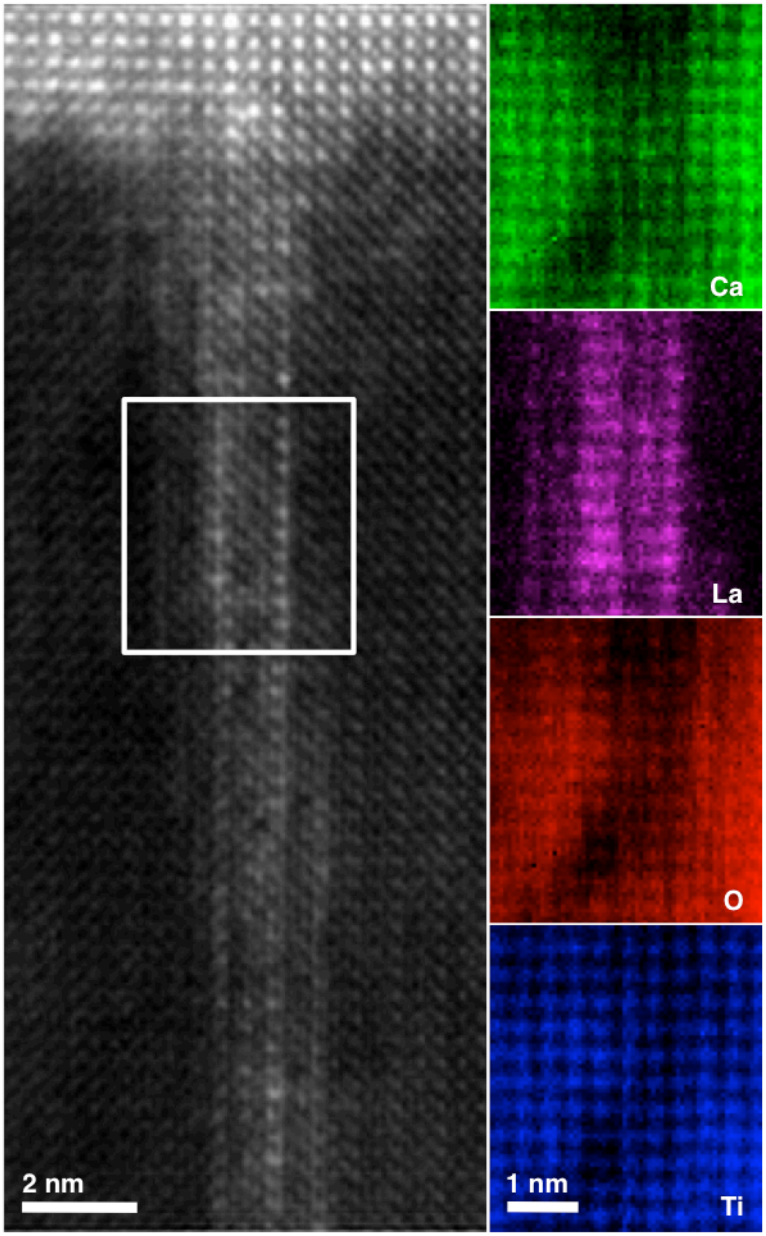

Figure A.3. A HAADF-STEM image of a vertical fast diffusion path in the $CaTiO_3$ film populated with anomalously high La content, along with EELS elemental maps of the region indicated.

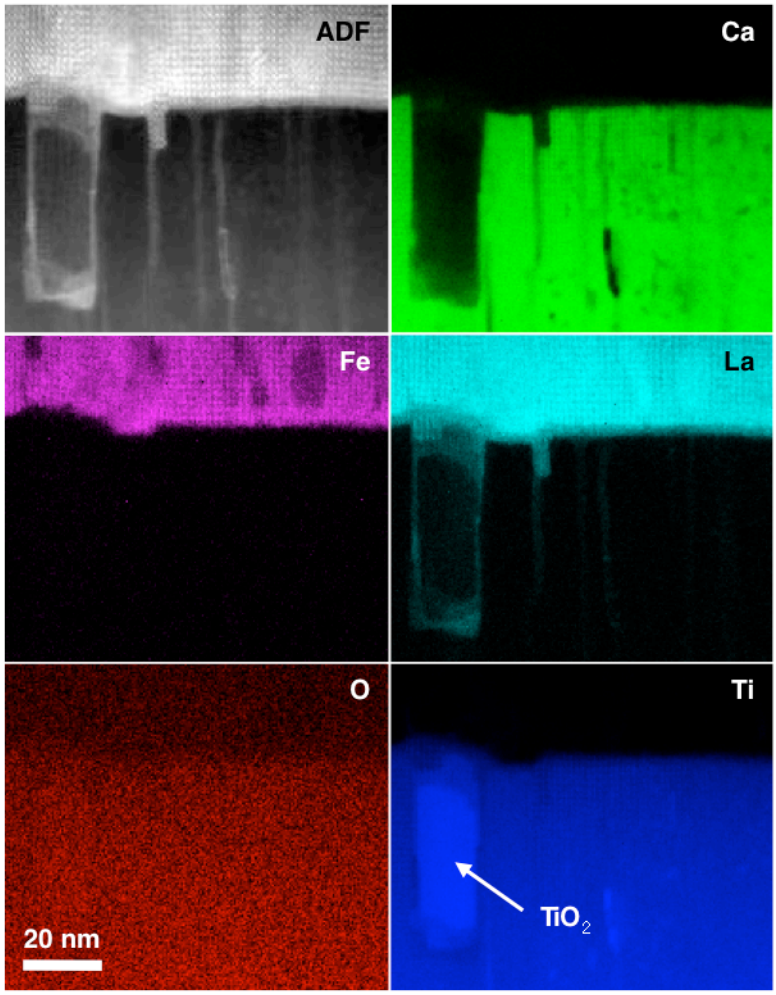

Figure A.4. An ADF-STEM image of a typical region in the $CaTiO_3$ layer showing significant La diffusion along columnar defects as well as around an anatase TiO_2 defect phase region within the thin film.

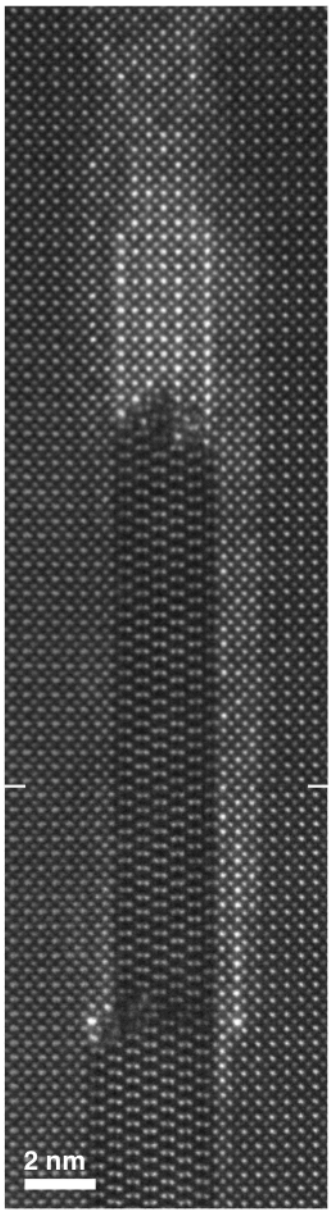

Figure A.5. Atomic-resolution HAADF-STEM image showing preferential La diffusion to and around a columnar anatase TiO_2 region. The $LaFeO_3$ film is above the region pictured. (The white notches indicate the edges of the boundary between two images that were stitched together to form this figure.)

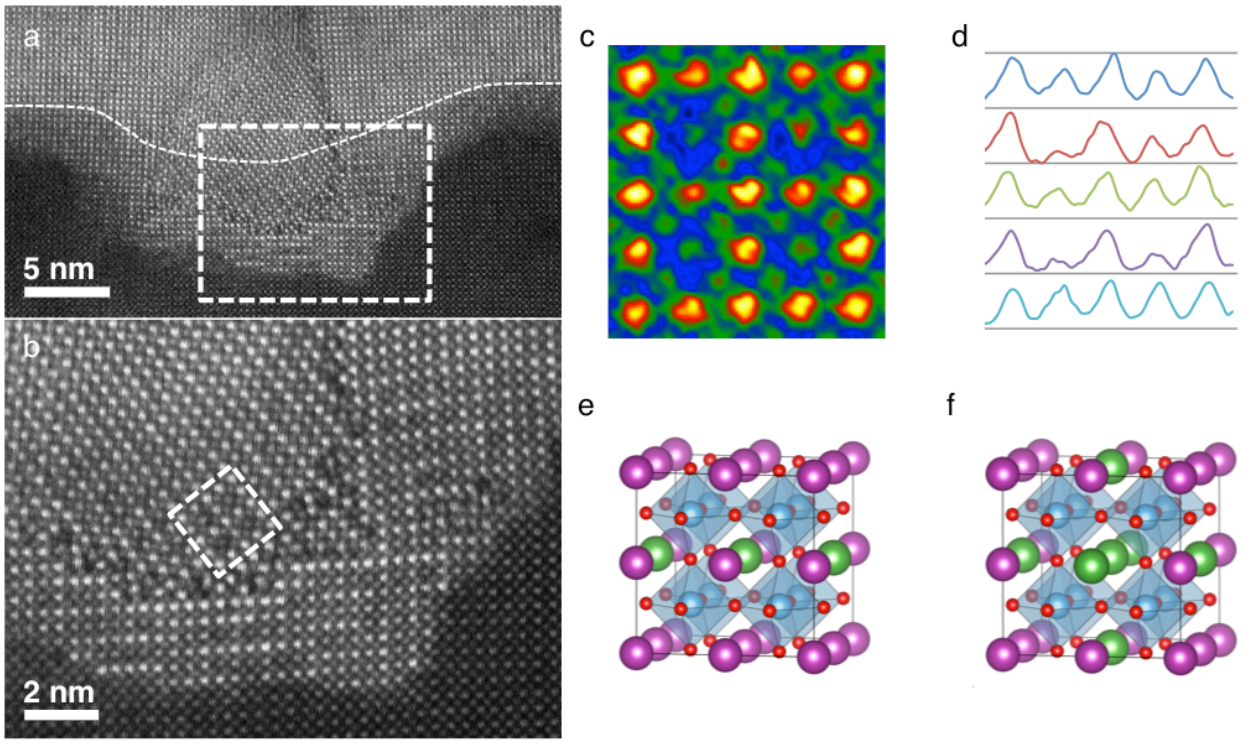

Figure A.6. (a) HAADF-STEM image of a defective region at the $LaFeO_3/CaTiO_3$ interface, with the original interface indicated by the lighter dashed line. (b) A higher resolution images of the region indicated in (a) exhibiting a-site ordering. (c) Enlargement of the region indicated in (b), showing complex ordering. The column intensity profiles are shown in (d). (e, f) Schemes showing possible a-site ordering that would generate the one-dimensional and two-dimensional superlattices seen in the images.

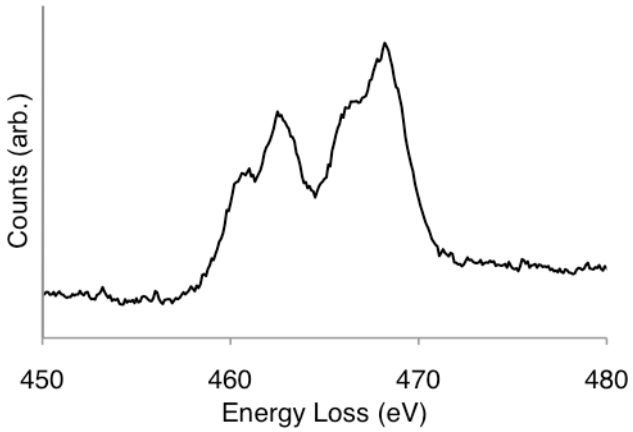

Figure A.7. Ti $L_{2,3}$ EELS edge from the La diffusion zone region in $CaTiO_3$, showing mixed Ti^{4+} and Ti^{3+} character.